Title
Hot Electron Generation and Laser–Plasma Instabilities in Shock Ignition Conditions

Author
Zhang, Shu

Publication Date
2020

UNIVERSITY OF CALIFORNIA SAN DIEGO

Hot Electron Generation and Laser–Plasma Instabilities in Shock Ignition Conditions

A dissertation submitted in partial satisfaction of the
requirements for the degree
Doctor of Philosophy

in

Engineering Sciences (Engineering Physics)

by

Shu Zhang

Committee in charge:

Farhat N. Beg, Chair
Prabhakar Bandaru
Christopher Holland
Sergei Krasheninnikov
Kevin B. Quest
Mingsheng Wei

2020

The dissertation of Shu Zhang is approved, and it is acceptable in quality and form for publication on microfilm and electronically:

Chair

University of California San Diego

2020

DEDICATION

For my father, in memoriam.

TABLE OF CONTENTS

LIST OF FIGURES

LIST OF TABLES

ACKNOWLEDGEMENTS

First of all, I want to thank my advisors, Prof. Farhat Beg and Dr. Mingsheng Wei, for all their guidance in these six years. Their broad knowledge and extensive expertise in this field are the most valuable resources for me. I also want to thank Christine Krauland for her indispensable help with the experiments.

I would also like to thank the group members at UCSD: Rui Hua, Jonathan Peebles, Christopher McGuffey, Maylis Dozieres, Mathieu Bailly-Grandvaux, Adam Higginson, Daiki Kawahito, Krish Bhutwala, Joe Strehlow and SJ Spencer. We had a lot of fruitful discussions, and they spent a lot of their free time helping me improve my presentations and writing.

I also want to thank Bill for teaching me fencing, Jeff and San Diego Mountain Biking Association for hosting group mountain biking events, SD Orienteering Club for setting up orienteering courses, and Fang Rongxin, Ye Jingqiang, Nie Jiuyuan, Yu Huan and Yan Qizhang for running, gyming, and surfing with me in these years. They are my mental support.

I feel so lucky to meet my love, Ren Chi, who is willing to discuss with me about all my crazy ideas and random thoughts in these years.

Finally, I want to thank my parents for their love and support in my whole life. My father was like my third advisor. He was always encouraging me to push this research one step further. Every year when I came back home, the first day was always like an annual review. I hope he could be satisfied with the result.

Chapter 4 is currently being prepared for the publication: “Pump-depletion Dynamics and Saturation of Stimulated Brillouin Scattering in Shock Ignition Condition”, S. Zhang, J. Li, C. M. Krauland, H. Reynolds, S. Muller, F. N. Beg, W. Theobald, C. Ren, C. Stoeckl, D. Haberberger, T. Filkins, D. Turnbull, R. Betti, E. M. Campbell, J. Trela, D. Batani, R. Scott, M. S. Wei. The dissertation’s author is the primary investigator and author of this paper.

Chapter 5 is a reprint of the publication: “Experimental Study of Hot electron Generation in Shock Ignition Relevant High-intensity Regime with Large Scale Hot Plasmas”, S. Zhang, C. M. Krauland, J. Peebles, J. Li, F. N. Beg, N. Alexander, W. Theobald, R. Betti, D. Haberberger, E. M. Campbell, R. Yan, E. Borwick, C. Ren, and M. S. Wei, *Physics of Plasma* 27, 023111 (2020). The dissertation’s author is the primary investigator and author of this paper.

Chapter 6 is currently being prepared for submission and publication: “Generation of Collimated Moderate Temperature Electron Beam and Laser–Plasma Interaction for Megajoule Shock Ignition”, S. Zhang, C. M. Krauland, J. Li, J. Peebles, F. N. Beg, S. Muller, N. Alexander, C. Ren, W. Theobald, R. Betti, D. Haberberger, E. M. Campbell, R. Yan, E. Borwick, J. Trela, D. Batani, P. Nicolai, and M. S. Wei. The dissertation’s author is the primary investigator and author of this paper.

I acknowledge the OMEGA EP and OMEGA 60 laser facility staff at the Laboratory for Laser Energetics. This work was performed under the auspices of U.S. DOE NNSA under the NLUF program with award number DE-NA0002730, DE-NA0003600, DOE Office of Science under the HEDLP program with award number DE-SC0014666 and DOE Office of Science under DE-SC0012316. The FLASH code used in this work was in part developed by the DOE NNSA-ASC OASCR Flash Center at the University of Chicago. The support of the DOE does not constitute an endorsement by the DOE of the views expressed in this article.

VITA

2014	Bachelor of Science, School of Physics, Peking University, Beijing, China
2020	Doctor of Philosophy, in Engineering Sciences (Engineering Physics), Department of Mechanical & Aerospace Engineering, University of California San Diego, United States

PUBLICATIONS

S. Zhang, C. M. Krauland, J. Peebles, J. Li, F. N. Beg, N. Alexander, W. Theobald, R. Betti, D. Haberberger, E. M. Campbell, R. Yan, E. Borwick, C. Ren, and M. S. Wei, “Experimental Study of Hot electron Generation in Shock Ignition Relevant High-intensity Regime with Large Scale Hot Plasmas” *Physics of Plasmas* 27, 023111 (2020)

S. Zhang, J. Li, C. M. Krauland, H. Reynolds, S. Muller, F. N. Beg, W. Theobald, C. Ren, C. Stoeckl, D. Haberberger, T. Filkins, D. Turnbull, R. Betti, E. M. Campbell, J. Trela, D. Batani, R. Scott, M. S. Wei, “Pump-depletion Dynamics and Saturation of Stimulated Brillouin Scattering in Shock Ignition Conditions” *submitted to Physical Review Letter* (under revision)

S. Zhang, C. M. Krauland, J. Li, J. Peebles, F. N. Beg, S. Muller, N. Alexander, C. Ren, W. Theobald, R. Betti, D. Haberberger, E. M. Campbell, R. Yan, E. Borwick, J. Trela, D. Batani, P. Nicolai, and M. S. Wei, “Generation of Collimated Moderate Temperature Electron Beam and Laser Plasma Interaction for Megajoule Shock Ignition” (in preparation)

J. Li, S. Zhang, C. M. Krauland, H. Wen, F. N. Beg, C. Ren, and M. S. Wei, “Pump Depletion and Hot-electron Generation in Long-density-scale-length Plasma with Shock-ignition High Intensity Laser”, *Physical Review E* 101, 033206 (2020)

M. Bailly-Grandvaux, J. Kim, C. Krauland, S. Zhang, M. M. Dozieres, M. S. Wei, W. Theobald, P. E. Grabowski, J. J. Santos, P. Nicolai, Transport of kJ-laser-driven relativistic electron beams in cold and shock-heated vitreous carbon and diamond, *New Journal of Physics* 22, 033031 (2020)

M. Dozières, S. Hansen, P. Forestier-Colleoni, C. McGuffey, D. Kawahito, M. Bailly-Grandvaux, K. Bhutwala1, C. M. Krauland, M. S. Wei, P. Gourdain, J. R. Davies, K. Matsuo, S. Fujioka, E. M. Campbell, J. L. Peebles, J. J. Santos, D. Batani, S. Zhang, and F. N. Beg, Characterization of an imploding cylindrical plasma for electron transport studies using x-ray emission spectroscopy, *Physics of Plasmas* 27, 023302, (2020)

C. K. Li, V. T. Tikhonchuk, Q. Moreno, A. F. A. Bott, S. Feister, H. Sio, E. D'Humières, P. Tzeferacos, G. Gregori, D. Q. Lamb, X. Ribeyre, Ph. Korneev, S. Atzeni, R. Betti, A. Birkel, E.M. Campbell, R. P. Drake, F. Fiuza, R. K. Follett, J. A. Frenje, S. X. Hu, C. M. Huntington, M. Koenig, H. S. Park, B. A. Remington, A. Rigby, J. S. Ross, D. D. Ryutov, Y. Sakawa, T. C. Sangster, F. H. Seguin, H. Takabe, S. C. Wilks, S. Zhang, and R. D. Petrasso, "Collisionless Shocks Driven by Supersonic Plasma Flows with Self-generated Magnetic Fields", *Physical Review Letter* 123, 055002 (2019)

J. Strehlow, P. Forestier-Colleoni, C. McGuffey, M. Bailly-Grandvaux, T. S. Daykin, E. McCary, J. Peebles, G. Revet, S. Zhang, T. Ditmire, M. Donovan, G. Dyer, J. Fuchs, E. W. Gaul, D. P. Higginson, G. E. Kemp, M. Martinez, H. S. McLean, M. Spinks, H. Sawada, and F. N. Beg, The Response Function of Fujifilm BAS-TR Imaging Plates to Laser-accelerated Titanium Ions, *Review of Scientific Instruments* 90, 083302 (2019)

H. Habara, T. Iwawaki, T. Gong, M. S. Wei, S. T. Ivancic, W. Theobald, C. M. Krauland, S. Zhang, G. Fiksel, and K. A. Tanaka, "A Ten-inch Manipulator (TIM) Based Fast-electron Spectrometer with Multiple Viewing Angles (OU-ESM)", *Review of Scientific Instruments* 90, 063501 (2019)

J. Peebles, A. V. Arefiev, S. Zhang, C. McGuffey, M. Spinks, J. Gordon, E. W. Gaul, G. Dyer, M. Martinez, M. E. Donovan, T. Ditmire, J. Park, H. Chen, H. S. McLean, M. S. Wei, S. I. Krasheninnikov, and F. N. Beg, "High-angle Deflection of the Energetic Electrons by a Voluminous Magnetic Structure in Near-normal Intense Laser-plasma Interactions", *Physical Review E* 98, 053202 (2018)

L. Ceurvorst, A. Savin, N. Ratan, M. F. Kasim, J. Sadler, P. A. Norreys, H. Habara, K. A. Tanaka, S. Zhang, M. S. Wei, S. Ivancic, D. H. Froula, and W. Theobald, "Channel Optimization of High-intensity Laser Beams in Millimeter-scale Plasmas", *Physical Review E* 97, 043208 (2018)

ABSTRACT OF THE DISSERTATION

Hot Electron Generation and Laser–Plasma Instabilities in Shock Ignition Conditions

by

Shu Zhang

Doctor of Philosophy in Engineering Sciences (Engineering Physics)

University of California San Diego, 2020

Farhat N. Beg, Chair

Shock ignition is an alternative inertial confinement fusion scheme, which uses a strong convergent shock generated by a ~10^{16} W/cm^2 spike laser pulse to ignite a pre-compressed fusion capsule. Understanding nonlinear laser–plasma instabilities (LPIs) and the physics of hot electron generation is critical for SI. LPIs can not only deplete the laser pump through scattering with the resonant electron plasma or ion-acoustic waves (IAW), but also generate hot electrons to assist the shock generation. We have conducted a series of experiments on the OMEGA EP and OMEGA-60 laser facilities demonstrating that stimulated Brillouin scattering (SBS) can deplete ~100% of the beam energy during the first ~0.5 ns of the 10^{16} W/cm^2 ultraviolet (UV) laser in an SI-relevant plasma ($L_n \sim 260 - 330$ μm). The pump-depletion started from the ~0.02 critical density (n_c) region and progressed to the 0.1–0.2n_c region, which was evidenced from the shape of the laser-generated blast wave and the time-resolved stimulated Raman backscattering spectra. This dynamic pump-depletion is consistent with an IAW-breaking SBS saturation model. Strong SBS was also observed in our large-scale Particle-in-Cell (PIC) modeling. The observed dynamic pump-depletion resolved a long-standing inconsistency of SBS reflectivity between PIC simulations and previous experiments. Although this pump-depletion would inhibit the collisional laser absorption, it may benefit the electron shock ignition scheme, which uses hot electrons with temperatures <100 keV to generate the ignition shock. Inferred from the bremsstrahlung x-ray spectra, the LPIs converted 2–6% of the laser energy into hot electrons with moderate temperatures ($T_{\text{hot}} \sim 45 - 90$ keV). In addition, Cu K-shell fluorescence images show these hot electrons are collimated. Analytical models suggest that these hot electrons are suitable to generate the required 300 Mbar ignition shock in a megajoule laser facility.

Chapter 1

Introduction

1.1 Energy evolution

All human activities are transformations of energy [1]. Since 9500 BC, humans have been transforming solar energy into chemical energy through cultivation [2]. Then, the industrial revolution provided ways to use fossil fuels, which powered the exponential growth of the economy over the 200 years. Besides the economy, the energy of fossil fuels has also been used to support the growing human population through the production of nitrogen fertilizers. However, the overuse of fossil fuels has negatively affected the environment; in particular, it has led to air and ocean pollution, and global warming. With the rapid growth in energy demand, these effects have worsened. Human development will be limited if fossil fuels are not replaced by sources of clean and renewable energy.

Global warming is the inevitable result of the CO_2 emission from burning fossil fuels. The atmospheric CO_2 level passed the historical maximum in 1950 and has continued to grow [3, 4, 5]. Meanwhile, the average temperature has increased by 0.9 °C since the late 19th century. The resulting climate change is affecting agriculture by diminishing crop growth and animal husbandry [6]. To prevent further global warming, we need a carbon-free energy source to replace fossil fuels.

One carbon-free energy is nuclear fusion energy. The most promising fusion power plant is designed to fuse hydrogen isotopes—deuterium and tritium—to generate energy. Similar to other clean energies, such as wind, solar, tidal, and geothermal energy, fusion energy is sustainable because deuterium is abundant in the ocean, and tritium can be converted from lithium. In contrast to those clean energies, fusion power plants will operate on demand and be independent on geographic conditions. The 2019 Texas heatwave drove the electricity demand high but reduced wind power production, raising the electricity price by a factor of 360 [7]. Moreover, California's photovoltaic panels cannot produce energy during the cloudy months, which requires the conventional thermal plant to remain on standby. The geographic requirement of the tidal and geothermal energy limits their usage, although they are more stable than the wind and solar power plants. However, net fusion energy production requires a stable, high-temperature, and high-density fuel condition, which has not yet been realized on Earth except for in thermonuclear bombs. The problem of how to harness nuclear fusion has been openly studied since it declassified in 1958 [8].

1.2 Nuclear fusion

Nuclear fusion is a nuclear reaction in which light atomic nuclei collide to form one or more different nuclei. A fusion reaction releases the difference in binding energy between the nuclei before and after the reaction. The binding energy per nucleon (proton or neutron) varies with the nucleus's atomic number, and is highest for ^{56}Fe, as shown in Fig. 1.1. The atomic-number dependence suggests that the fusion of nuclei lighter than Fe can produce energy; the fission of the nucleus heavier than Fe can also produce energy. The release of the fusion energy ΔE results in a mass change Δm of the fuel,

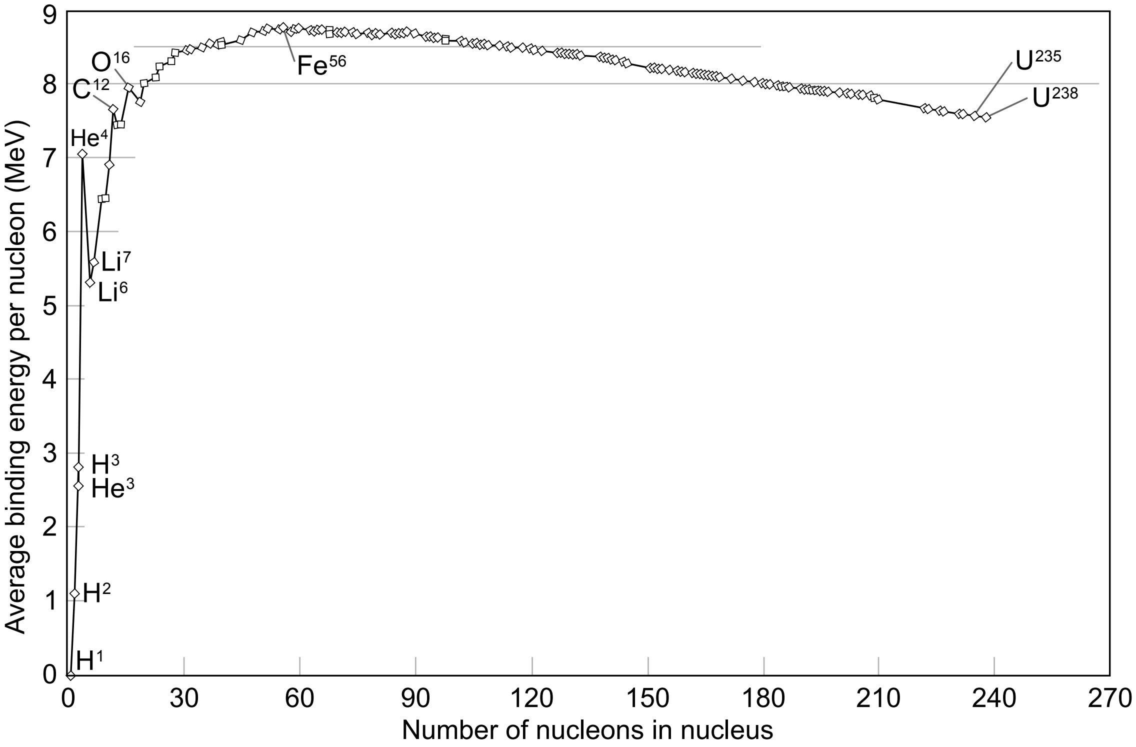

Figure 1.1: Binding energy per nucleon versus atomic number. Original data are available in Ref. [9].

which supports Einstein's famous mass-energy equivalence: $E = mc^2$.

Fusion is the energy source for stars. Stars like the Sun are made of dense and hot hydrogen. The protons can fuse to produce alpha particles and release 26.73 MeV of energy through proton–proton chain reactions as [10]

$$4\mathrm{p} \rightarrow {}^4\mathrm{He}^{2+} + 2\mathrm{e}^+ + 2\nu_\mathrm{e}. \tag{1.1}$$

However, this chain reaction is a slow process, because its first step,

$$\mathrm{p} + \mathrm{p} \rightarrow \mathrm{D} + \mathrm{e}^+ + \nu_\mathrm{e}, \tag{1.2}$$

is rare. A proton's average lifetime in the Sun is about 10^9 years. Owing to this long timescale, although a proton–proton chain reaction is neutron-free, it can provide energy

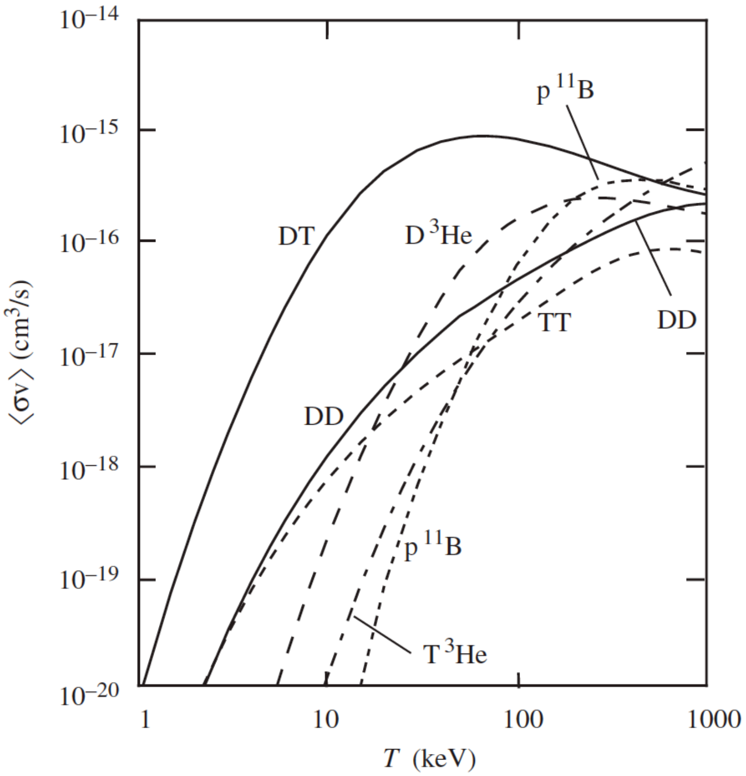

Figure 1.2: Reaction rate versus ion temperature for common fusion reactions, assuming a Maxwell velocity distribution [11].

only for stars.

Deuterium–tritium (DT) fusion attracts the most attention because of its high reaction rate and ample fuel supply. The reaction rate is the higher than that of all other fusion reactions in the temperature range below 400 keV [11], as shown in Fig. 1.2. The deuterium in a glass of ocean water can produce the same energy as a gallon of oil. A DT-fusion reaction produces a 3.5 MeV alpha particle and a 14.1 MeV neutron. Although the generated neutrons may irradiate the reactor and produce radioactive waste, they could also breed tritium and reduce the fuel price. With ample fuel supply, DT-fusion energy could support humanity for much longer than all fossil fuels.

For a pulsed DT-fusion reactor where the radiations and the particles can escape, Lawson found that this system needs to keep a DT plasma at a high temperature (T) and a high ion density (n) for a relatively long duration (τ) to generate more energy than is lost [12]. This criterion can be expressed as

$$\frac{\tau P_{\mathrm{R}}}{\tau P_{\mathrm{B}} + 3(n_{\mathrm{D}} + n_{\mathrm{T}})T} > 2, \tag{1.3}$$

in which the reaction energy power per unit volume P_{R} is

$$P_{\mathrm{R}} = n_{\mathrm{D}} n_{\mathrm{T}} \overline{v\sigma(T)} E, \tag{1.4}$$

where $E = 3.5$ MeV is the released alpha particle energy in DT-fusion, the bremsstrahlung radiated power P_{B} is [13]

$$P_{\mathrm{B}} = 1.69 \times 10^{-32} n_{\mathrm{i}}^2 T^{1/2}\ \mathrm{W/cm^3}, \tag{1.5}$$

where T is in eV, $3(n_{\mathrm{D}} + n_{\mathrm{T}})T$ is the internal energy of the DT plasma, assuming $T_{\mathrm{e}} = T_{\mathrm{i}}$, $\overline{v\sigma(T)}$ is the Maxwell-averaged reaction rate, as shown in Fig. 1.2. Because both P_{B} and P_{R} are proportional to n^2, the criterion reduces to $n\tau > 1.5 \times 10^{14}$ s/cm^3 when $T = 26$ keV or $nT\tau > 3 \times 10^{15}$ keV$\cdot$s/cm^3 when $T = 14$ keV.

To meet the Lawson criterion, several fusion schemes have been proposed. The three primary schemes are i) inertial confinement fusion (ICF), in which an imploded fuel capsule is confined by its inertia, ii) magnetic confinement fusion (MCF), in which magnetic fields confine a hot DT plasma, and iii) magneto-inertial fusion (MIF), in which a pulsed Lorentz force implodes a fuel cylinder and confines the cylinder by its inertia. This dissertation concerns an alternative ICF scheme: shock ignition [14].

1.3 Inertial confinement fusion and its challenges

Inertial confinement fusion (ICF) uses high-power lasers to implode a fusion fuel capsule to achieve the required high density and high temperature. These lasers heat and ablate the surface of a millimeter-sized DT capsule. This capsule consists of a DT ice shell that is filled with DT vapor and covered with a CH ablator, as shown in Fig. 1.3. By the rocket effect, the remaining shell is pushed inward. During this implosion, the DT vapor in the center of the capsule is heated to ~10 keV, starts the fusion reaction and produces 3.5 MeV alpha particles. These energetic particles heat the compressed DT fuel around the hot spot and create a burn wave that propagates outward. This burn wave can heat and burn the dense fuel around the hot spot to produce more fusion energy.

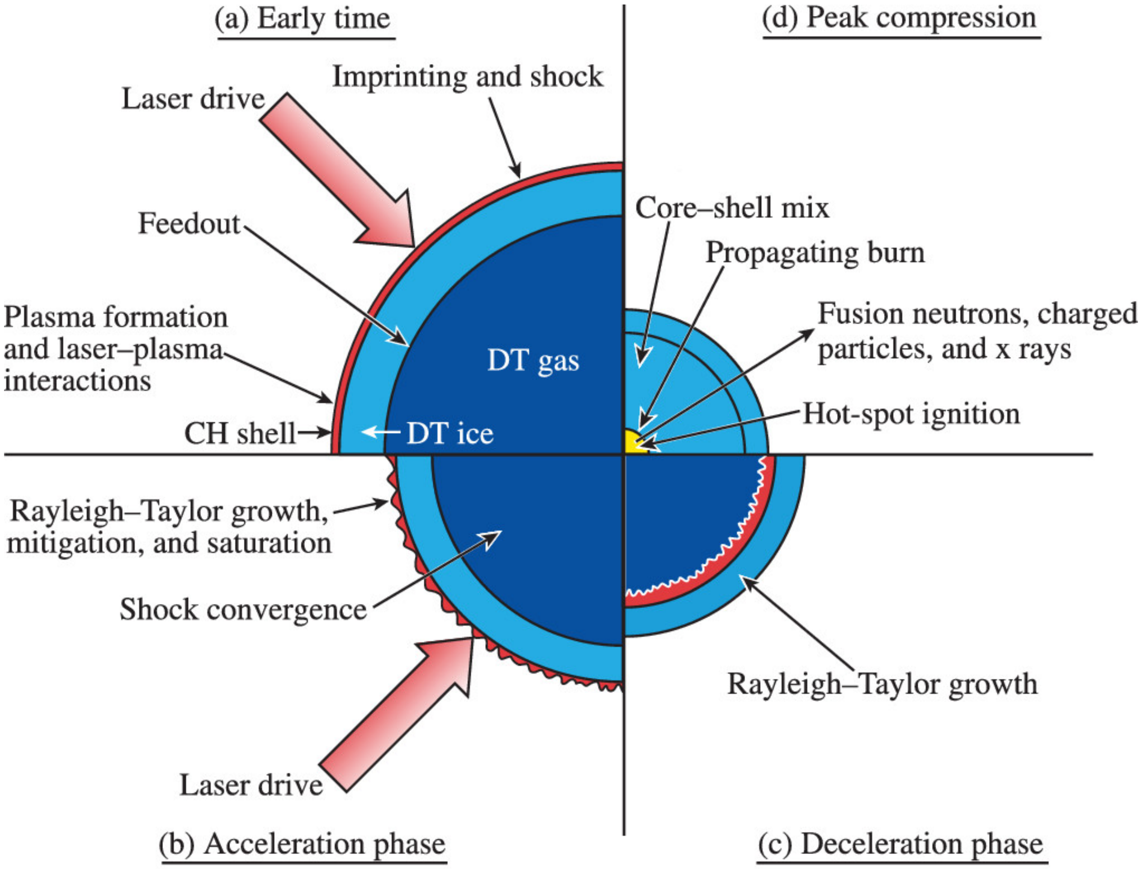

Figure 1.3: Four stages of direct drive inertial confinement fusion and the typical implosion target [15].

Reference [16] describes a simplified model to estimate the confinement time for ICF. The model calculates the disassembly time for a sphere of a dense DT plasma that is homogeneous. In this sphere, a rarefaction wave will move inward with the sound velocity

$$c_{\mathrm{s}} = \sqrt{\gamma T/m_{\mathrm{ion}}}. \tag{1.6}$$

Therefore, for the material at radius r' from the center of the sphere, the local confinement time is

$$\tau_c(r') = \frac{R - r'}{c_{\mathrm{s}}}. \tag{1.7}$$

The mass-averaged confinement time for this sphere is

$$\tau_{\mathrm{c}} = \int_0^R \frac{4\pi r'^2 \rho}{\frac{4}{3}\pi\rho R^3} \frac{R - r'}{c_{\mathrm{s}}} \mathrm{d}r' = \frac{R}{4c_{\mathrm{s}}}. \tag{1.8}$$

During the disassembly, only a fraction of the fuel will be burned. The burn fraction is commonly approximated as

$$\Phi = \frac{\rho R}{7 + \rho R}, \tag{1.9}$$

where ρR is in g/cm^2. A burn fraction of 1/3 would need $\rho R \gtrsim 3$ g/cm^2. Such a high ρR requires $\rho = 80$ g/cm^3 for a 1 mg spherical target, which implies a 300-fold compression of the cryogenic DT fuel.

However, uniformly heating the fuel to the fusion temperature requires large amount of energy, as discussed in Sec. 1.2. To minimize the energy needed to start the fusion, researchers have designed a scheme, known as central hot-spot ignition, which implodes a fuel capsule, as shown in Fig. 1.3. The implosion heat and fuse only the DT vapor while keeping the surrounding fuel cold and dense. This surrounding fuel acts both as a tamper to confine the hot spot and as a fuel reservoir. The burn wave from the hot spot will propagate outward and ignite the cold fuel.

Central hot-spot ignition has its challenges. Two major ones are the laser–plasma instability (LPI) and the Rayleigh–Taylor instability (RTI). LPIs are the instabilities of the laser light propagating in a plasma. The electromagnetic wave can stimulate plasma waves or ion-acoustic waves and secondary electromagnetic waves. The generation of secondary electromagnetic waves depletes the laser energy; the produced plasma waves can induce superthermal electrons preheating the fuel. The preheating may inhibit the fuel compression. RTI happens when a light fluid pushes against a denser material. Perturbations along the fluid interface grow and cause mixing. During the implosion, RTI can occur in two phases: i) during the ablation, and ii) in the stagnation. When the lasers irradiate the capsule surface, the heated low-density plasma accelerates into the dense shell. Similarly, when the hot spot decelerates the dense fuel, RTI could break the shell, causing leakage of the hot spot.

Both instabilities need to be mitigated in central hot-spot ignition. With limited laser energy, this design requires a high-speed implosion. The minimum energy required for ignition depends on the in-flight adiabat of the fuel (α_{if}), the implosion velocity (v_{imp}), and the pressure out of the shell at the time of the peak implosion velocity P [17]:

$$E_{\text{ign}}(\text{kJ}) = 50.8\alpha_{\text{if}}^{1.88\pm0.05}\left(\frac{v_{\text{imp}}}{3\times10^{7}\ \text{cm/s}}\right)^{-5.89\pm0.12}\times\left(\frac{P}{100\ \text{Mbar}}\right)^{-0.77\pm0.03}. \tag{1.10}$$

The high implosion velocity would thin the shell during the implosion and induce the growth of RTI [11]. This velocity also requires a high laser intensity on the order of 10^{15} W/cm^2, which can stimulate LPIs [18].

To mitigate RTI, instead of using lasers to irradiate the fuel capsule directly, researchers proposed to use a gold hohlraum to convert the lasers to x-rays since the ablation driven by electron conduction is generally less stable than the ablation driven by x-rays. [19] This scheme is known as indirect-drive ICF; the scheme that uses lasers to irradiate the capsule is known as direct-drive ICF. However, even with the hohlraum, the 15–100 nm thin tent holding the target still seeds the hydrodynamic perturbation causing fuel mixing and the leakage of the hot spot. [20]

Since 1999, to bypass the impact of RTI and LPIs, researchers have proposed several alternative schemes, such as fast ignition [21] and shock ignition [14, 22]. Both schemes separate the compression and ignition phases. Because the ignition is no longer the consequence of the compression, the compression can be achieved using a lower-speed, stable implosion. Then, in fast ignition, a fast-electron beam generated by a PW laser is injected into the compressed capsule to ignite it. In shock ignition, a direct-drive scheme, a converging shock launched by a sub-nanosecond laser pulse with an intensity of 10^{16} W/cm^2 forms a non-isobaric hot spot to ignite a pre-compressed capsule. Shock ignition is the topic of this dissertation.

1.4 Shock ignition

Shock ignition (SI) is an alternative inertial confinement fusion (ICF) scheme [14, 22]. In the SI scheme, the separation of the compression and ignition phases may provide a more stable implosion and a higher energy gain than the conventional central hot-spot ICF [23]. The implosion stability is improved through lowering the implosion velocity which can inhibit the Rayleigh–Taylor instability. A high energy gain is predicted in simulations because the formation of the non-isobaric hot spot may improve the energy conversion from the drive laser to the hot spot by limiting the pressure of the surrounding compressed fuel [14]. The required laser energy is lowered by a factor $(p_{\mathrm{hs}}/p_{\mathrm{iso}})^{2.5}$ [22], in which p_{hs} is the pressure of the non-isobaric hot spot, and p_{iso} is the isobaric pressure. Owing to these advantages, SI has been proposed for megajoule (MJ) and sub-MJ laser facilities such as National Ignition Facility (NIF) [24, 25], Laser Megajoule (LMJ) [26] and

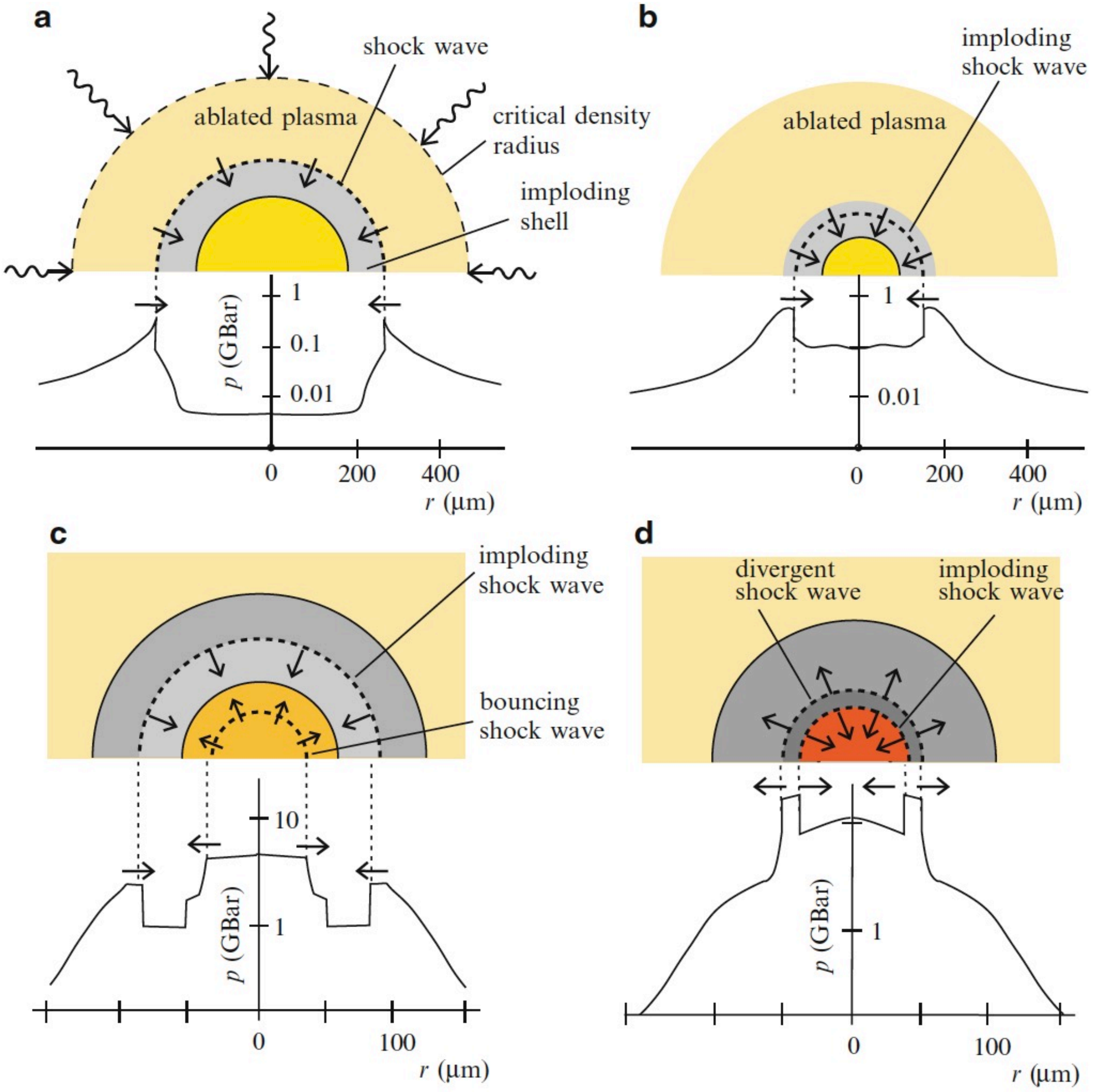

Figure 1.4: The sequences of shock ignition. (a) the shell implodes with a velocity lower than that of the conventional central hot-spot ICF. (b) the implosion shock convergence, compressing the capsule. (c) A spike pulse generates a second shock while the implosion shock bounces from the center. (d) the shock collision amplifies the ignition implosion shock [29].

High Power Laser Energy Research facility (HiPER) [27, 28].

The sequences of shock ignition is shown in Fig 1.4. Similar to the central hot-spot ignition scheme, a nanoseconds laser pulse irradiates and implodes the capsule. The implosion shock bounces at the center of the capsule and forms a return shock the propagates outward. After the implosion, a high-intensity (~10^{16} W/cm^2) sub-nanosecond spike laser launches a high pressure shock to collide with the return shock and form an amplified inward shock. When this inward shock converges at the center, it increases the pressure and temperature of the hot spot to ignite the capsule while keeping the surrounding fuel at a lower pressure than the hot spot. This hot spot is known as a non-isobaric hot spot. To generate the amplified inward shock, the shock produced by the spike laser needs to have a comparable pressure to the return shock before the shock collision, which requires an initial pressure of ~300 Mbar at the ablation front, where the flow velocity is 0 [30]. This pressure, known as the ablation pressure p_a, scales with the laser intensity I_L based on the model of inverse-bremsstrahlung absorption, as discussed in Sec. 2.2 and Sec. 2.5.1:

$$p_\mathrm{a} = 40(I_\mathrm{L}/\lambda)^{2/3}\ \mathrm{Mbar}, \tag{1.11}$$

where I_L is in units of 10^{15} W/cm^2, and λ is the laser wavelength in µm [31]. This scaling law suggests that 7×10^{15} W/cm^2 lasers could generate the 300 Mbar ablation pressure shock.

The concept of SI has been validated in the experiments on the 30-kJ 60-beam OMEGA laser facility in the Laboratory of Laser Energetics [32]. Limited by the laser energy (~30 kJ), these experiments scaled down the laser power by one order of magnitude while keeping the pulse shape similar to the MJ design. The pulse shapes with and without the spike were then compared. The implosions that had the SI pulse shape produced more neutrons than those that had the conventional pulse shape. Moreover, the pulse with the spike also improved the area density, yield of clean and hydrodynamic stability of the implosion capsule.

1.5 Physics issues of shock ignition

The initial shock ignition experiment validated the scheme's high-gain and stability benefit from the pulse shape design. However, this experiment reduced the spike intensity to ~7×10^{14} W/cm^2, which is one order of magnitude lower than the intensity required to generate the ~300 Mbar shock for full-scale shock ignition [32]. For a ~10^{16} W/cm^2 laser in full-scale shock ignition, the laser–plasma instabilities (LPIs) may be much stronger than those for a ~10^{15} W/cm^2 laser [33, 34, 35]. Such stronger LPIs would complicate the energy conversion from the laser to the shock [36]. For example, stimulated Brillouin scattering (SBS) [37] and stimulated Raman scattering (SRS) [38] can deplete the laser pump; SRS and two-plasmon decay (TPD) [39] can convert the laser energy into superthermal electrons. Whether a ~10^{16} W/cm^2 laser can generate the 300 Mbar shock remains uncertain. As a result, the feasibility of full-scale shock ignition still requires an experimental study.

Experiments have been performed to characterize the shock generated by 10^{15}–10^{16} W/cm^2 lasers. For example, experiments conducted at the Ligne d'Intégration Laser (LIL) facility generated a 90 Mbar shock on a planar target and a 120 Mbar shock on a spherical-front target using ~10^{15} W/cm^2 10 kJ lasers [40]. In addition, OMEGA lasers that have intensities of up to 1.4×10^{15} W/cm^2 produced a 75 Mbar shock in the presence of a large-scale plasma [41]. However, the 10^{16} W/cm^2 3ω laser on Prague Asterix Laser System (PALS) also generated a 90 Mbar shock [42]. Another set of PALS experiments found that the ablation pressure increased to 180 Mbar when a ~5×10^{16} W/cm^2 1ω laser directly interacted with the target [43]. These experiments also showed that the preformed plasma can decrease the laser energy absorption [44]. The experiments on OMEGA-60 that had a reduced target size generated a 300 Mbar shock using 6×10^{15} W/cm^2 UV lasers [45, 46]. Analysis of these experiments suggest that 30% of the shock pressure is contributed by hot electrons generated by LPIs.

For the conventional central hot-spot ICF scheme, the LPI-induced hot electrons would preheat the fuel because they can penetrate the ablator and deposit their energy in the fuel. By contrast, shock ignition may benefit from hot electrons. In this scheme, the hot electrons can be stopped by the capsule surface because the capsule is partially compressed before the spike pulse [14, 22]. Simulations predict that hot electrons of temperature $T_{\mathrm{hot}} < 100$ keV could improve full-scale shock ignition by increasing the gain and expanding the parameter space for robust ignition designs [22, 25]. The LPI-accelerated hot electrons may also generate the 300 Mbar shock if the intensity of the electron beam can reach 10^{15} W/cm^2 [47, 48, 49]. Generating the ignition shock solely by hot electrons is proposed in Ref. [50] and is known as the electron shock ignition. Therefore, it is necessary to characterize the temperature and total energy of these hot electrons to determine their role in shock ignition.

The LPIs and the hot-electron generation depend on the laser's intensity and wavelength, and the plasma's temperature and length scale [18]. When the laser intensity is about 10^{15} W/cm^2, the efficiency of the energy conversion from the laser to the hot electrons has been found to increase with the spike-pulse intensity in particle-in-cell (PIC) simulations [35, 51, 52] and experiments [41, 53, 54, 55] conducted at the OMEGA and NIF laser facilities. The OMEGA planar experiments [41] and the NIF spherical experiments [53] found that TPD induced by overlapping beams of intensity 0.6×10^{15} W/cm^2–1.4×10^{15} W/cm^2 generated hot electrons of temperature 20–70 keV, and an energy conversion efficiency of up to 1.8%. The $\sim 10^{15}$ W/cm^2 NIF planar experiment with larger plasma length scale (500–700 μm) showed that SRS contributes the majority of the hot electron generation with $T_{\mathrm{hot}} \sim 50$ keV and up to ~3% energy conversion efficiency [54, 55]. When the laser intensity was increased to $2-6 \times 10^{15}$ W/cm^2 in OMEGA experiments, $60-80$ keV hot electrons were detected, and the energy conversion efficiency was also increased to $2-9\%$ [45, 46]. When higher intensities $\sim 10^{16}$ W/cm^2 non-overlapped lasers were used, the conversion efficiency and the hot electron temperature drop to 0.1–5% and 20–50 keV, respectively [56, 57, 58, 59]. However, those experiments were conducted in smaller plasmas with scale-lengths (L_n) from 10s of μm [57, 58, 59] to ~170 μm [56]. Because the plasmas density scale-length and temperature can influence the competition in LPIs, such as that between SRS and TPD [54, 60], characterization experiments for ~10^{16} W/cm^2 lasers in large-scale ($L_n > 300$ μm) and high-temperature (>keV) plasmas are warranted.

The pump depletion induced by the LPIs can inhibit the laser–shock energy coupling. PIC simulations involving ~10^{16} W/cm^2 intensities and large plasmas have shown >50% SBS reflectivity [33, 34, 35], which is not seen in small-scale simulations [60, 61, 62] or in experiments [40, 46, 56, 63, 64, 65, 66, 67]. Some experiments have observed a burst of SBS at the beginning of the laser spike [40, 46, 63, 64]. However, those experiments were limited by either small plasma length-scales ($L_n < 170$ μm) or low laser intensities (~ 10^{14}–10^{15} W/cm^2). The large-scale plasma created by the magejoule laser (L_n ~ 300–500 μm and electron temperature $T_\mathrm{e} > 3$ keV) can affect the role of each LPI mode [54]. It is also challenging to extend the PIC simulations to full time and spatial scales with the current computational capability. Therefore, experiments are needed to characterize the LPI-induced pump depletion of 10^{16} W/cm^2 lasers in large-scale plasmas.

1.6 Outline of dissertation

A series of experiments were performed at the OMEGA Extended Performance (OMEGA EP) [68] and the 60-beam (OMEGA-60) laser facilities at the Laboratory of Laser Energetics to solve the issues described in Sec. 1.5.

Chapter 2 discusses the physics theories related to shock ignition. It first summarizes the linear theory of laser–plasma instabilities and then describes the role of the suprathermal electrons in shock ignition.

Chapter 3 details the experimental setup the simulation tools, including the target designs, the OMEGA laser facility, the diagnostics, the radiation-hydrodynamic code FLASH, and the Monte Carlo code GEANT4.

Chapter 4 discusses the strong pump-depletion found in the experiments with a high-intensity UV laser beam interacting with a preformed large-scale plasma. Analysis of the observed laser-generated blast wave suggests that this pump-depletion starts at 0.01–0.02 critical density and progresses to 0.1–0.2 critical density. The time-resolved stimulated Raman backscattering spectra also confirmed the dynamic pump-depletion.

Chapter 5 describes the plasma characterization and the hot electron measurement results. The plasma was preformed by two UV laser beams, then a high-intensity IR or UV laser was injected to interact. The plasma density profiles were characterized by comparing the experimental angular filter refractometer (AFR) images to the simulated AFR images. The hot electron temperature and total energy were inferred by fitting the synthetic bremsstrahlung x-ray spectra to the measured spectra.

Chapter 6 shows the divergence angle measurement for the hot electrons. Collimated hot electron beams were found in these experiments. This chapter also discusses the required laser parameters to generate a high-pressure strong shock that can ignite the capsule.

Chapter 7 summarizes this dissertation.

1.7 Role of the author

The experiments described in Chapter 4, Chapter 5, and Chapter 6 were performed at OMEGA EP and OMEGA-60 laser facilities during five experiment days over four years from 2015 to 2018. The first two experiment days in 2015 and 2016 were designed by

Christine Krauland and Mingsheng Wei. The author planned and executed the three experiment days in 2017 and 2018. To optimize the plasma conditions for these experiments, the author used the FLASH radiation-hydrodynamic code to simulate the laser-generated plasma profiles. The author also analyzed Cu Kα images to quantify the hot electron divergence. For the hard x-ray spectrum analysis, the author simulated the target response functions by using the GEANT4 Monte Carlo simulation package. The author has also calculated the synthetic hard x-ray spectra and fitted the synthetic spectra to the measured spectra to infer the hot electron temperatures and energies. In addition, the author reconstructed the plasma density perturbations from the shadowgraphy images. The author has also calculated the synthetic AFR images based on the FLASH-simulated density profiles. The synthetic AFR images were compared with the experimental AFR images by the author to benchmark the FLASH code and reveal the pump-depletion dynamics. To explain the pump-depletion dynamics, the author developed the SBS saturation model induced by the ion-acoustic wave breaking, which agrees with the observations.

The OMEGA EP and OMEGA-60 operation teams performed the experiments. General Atomics manufactured the targets and provided the target meteorology. The FLASH Center at the University of Chicago develops the FLASH open-source code. Dan Haberberger originally wrote the Matlab scripts used to generate the synthetic AFR images. The author adjusted the scripts to create the image from a density profile simulated by FLASH. The target response functions of the 3-layer (25 μm CH/20 μm Cu/50 μm Al) disk target and the detector response functions of the bremsstrahlung MeV x-ray spectrometer (BMXS) [69] were simulated by Jonathan Peebles using ITS 3.0 Monte Carlo code [70]. Jun Li performed the Osiris PIC simulations. The optical depth (OD) correction tables and the time and wavelength calibration for the EP sub-aperture backscattering spectrometer were from Tim Filkins. Micheal Rosenberg wrote the scripts to correct the OD and the dispersion. The author added a feature to correct the deformation of the streak camera images.

Chapter 2

Physics of Laser–Plasma Instabilities and Role of Hot Electrons in Shock Ignition

As discussed in Ch. 1.4 and Ch. 1.5, shock ignition needs a 10^{16} W/cm^2 laser to generate a ~300 Mbar shock to ignite a pre-compressed capsule made of fusion fuel. The physics mechanisms in laser propagation, absorption, and shock generation are complicated. This chapter first introduces the fundamental physics regrading laser propagation in plasma. Then, since laser–plasma instabilities are important for shock ignition, the theories of laser–plasma instabilities are discussed. Two of these instabilities, two-plasmon decay and stimulated Raman scattering, can generate hot electrons. These hot electrons may benefit shock ignition since they may generate the shock at certain temperatures. Two mechanisms for ignition shock generation are discussed: ablation by thermal conduction and ablation by hot electrons. In this chapter, equations are in Gaussian units by default. Temperatures usually have the dimension of energy; if they follow the Boltzmann constant k_B, they are in the unit of Kelvin.

2.1 Electromagnetic wave propagation in plasmas

Plasma is a quasineutral gas made of negatively and positively charged particles. This state can be achieved by heating any material to a high temperature ($\gtrsim 1$ eV, $1\text{ eV} = 11.6\times10^3$ K) since the energetic atoms can ionize each other. The ions and electrons are influenced by their electric and magnetic fields and are often considered as two individual fluids. Each fluid can have density and pressure perturbations and generate electric and magnetic fields.

Electromagnetic (EM) waves may propagate in a plasma depending on the wave's frequency and the plasma's density. Because of the lower mass of the electron, the oscillating electric field of the high frequency EM wave can drive the electrons. The electron fluid equation of motion is

$$\frac{\mathrm{d}\boldsymbol{u}_\mathrm{e}}{\mathrm{d}t} = -\frac{e}{m}\boldsymbol{E}(\boldsymbol{x})\exp(-\mathrm{i}\omega_0 t) - \frac{\nabla p_\mathrm{e}}{m_\mathrm{e} n_\mathrm{e}}, \tag{2.1}$$

where $\frac{\mathrm{d}\boldsymbol{u}_\mathrm{e}}{\mathrm{d}t}$ is the material derivative of the velocity, defined as

$$\frac{\mathrm{d}\boldsymbol{u}_\mathrm{e}}{\mathrm{d}t} = \frac{\partial \boldsymbol{u}_\mathrm{e}}{\partial t} + \boldsymbol{u}_\mathrm{e}\cdot\nabla\boldsymbol{u}_\mathrm{e}. \tag{2.2}$$

In a homogeneous or large-scale plasma, the $\frac{\nabla p_\mathrm{e}}{m_\mathrm{e} n_\mathrm{e}}$ term is in the longitudinal direction of the EM wave, so it can be neglected when the plasma is cold. The $\nabla\boldsymbol{u}_\mathrm{e}$ tensor can also be neglected if the length scale of the flow velocity, $L_{u_\mathrm{e}} = |\boldsymbol{u}_\mathrm{e}|/\nabla\cdot\boldsymbol{u}_\mathrm{e}$, is much larger than the wavelength. As a result, the EM wave's electric field would drive a current in which the current density is

$$\boldsymbol{J} = -n_0 e\boldsymbol{u}_\mathrm{e} = \frac{\mathrm{i}\omega_\mathrm{pe}^2}{4\pi\omega_0}\boldsymbol{E}, \tag{2.3}$$

where $\omega_\mathrm{pe} = 4\pi e^2 n_0/m_\mathrm{e}$ is the plasma frequency, and n_0 is the unperturbed electron density.

To derive the wave equation of the EM wave in plasma, we need to solve Maxwell's equations. Faraday's Law becomes

$$\nabla \times \boldsymbol{E} = \frac{\mathrm{i}\omega_0}{c}\boldsymbol{B} \tag{2.4}$$

if the magnetic field $\boldsymbol{B} = \boldsymbol{B}(\boldsymbol{x})\exp(-\mathrm{i}\omega_0 t)$ is in the same form as $\boldsymbol{E}$. Ampere's Law gives

$$\nabla \times \boldsymbol{B} = \frac{1}{c}\left(\frac{\mathrm{i}\omega_{\mathrm{pe}}^2}{\omega_0}\boldsymbol{E} - \mathrm{i}\omega_0\boldsymbol{E}\right). \tag{2.5}$$

Then, taking the curl of Eq. 2.4 and substituting the $\nabla \times \boldsymbol{B}$ from Eq. 2.5 gives

$$\nabla \times (\nabla \times \boldsymbol{E}) = \frac{-1}{c^2}\left(\omega_{\mathrm{pe}}^2 - \omega_0^2\right)\boldsymbol{E}, \tag{2.6}$$

in which

$$\nabla \times (\nabla \times \boldsymbol{E}) = \nabla(\nabla \cdot \boldsymbol{E}) - \nabla^2\boldsymbol{E}. \tag{2.7}$$

Here, Gauss's law gives $\nabla \cdot \boldsymbol{E} = 4\pi n_{\mathrm{e1}}$, where n_{e1} is the electron density perturbation following the mass conservation law:

$$\frac{\partial n_{\mathrm{e1}}}{\partial t} + \nabla \cdot (\boldsymbol{u}_{\mathrm{e}} n_{\mathrm{e}}) = 0. \tag{2.8}$$

However, the density perturbation term is usually neglected when the plasma has a large density scale, reducing the $\boldsymbol{E}$ equation to

$$\nabla^2\boldsymbol{E} + \frac{\omega_0^2 - \omega_{\mathrm{pe}}^2}{c^2}\boldsymbol{E} = 0, \tag{2.9}$$

which is in the form of a wave equation. Similarly, the $\boldsymbol{B}$ equation can also be derived by taking the curl of Eq. (2.5) and substituting $\nabla \times \boldsymbol{E}$ from Eq. (2.4). The resulting equation includes the term $\nabla\omega_{\mathrm{pe}}^2$. This term can be neglected if the plasma is close to homogeneous. As a result, $\boldsymbol{B}$ obeys the same wave equation as $\boldsymbol{E}$. When assuming a planar wave where $\boldsymbol{E}(\boldsymbol{x}) = \boldsymbol{E}_0 \exp(\mathrm{i}\boldsymbol{k}\cdot\boldsymbol{x})$, the dispersion relation of the EM wave in a plasma becomes

$$\omega_0^2 = \omega_{\mathrm{pe}}^2 + k^2c^2. \tag{2.10}$$

Based on this dispersion relation, the phase velocity v_{ph} of the EM wave is higher than light speed in vacuum since

$$v_{\mathrm{ph}} = \frac{\omega_0}{k} = \frac{\omega_0 c}{\sqrt{\omega_0^2 - \omega_{\mathrm{pe}}^2}}. \tag{2.11}$$

The refractive index $\eta = c/v_{\mathrm{ph}} < 1$ depends on the plasma density, which means the phase front of the propagated EM wave contains the information of the density profile in the plasma. The related laser probe diagnostics are described in Sec. 3.3.3.

The dispersion relation, Eq. (2.10), also defines the region where the wave can propagate. In the $\omega_0 < \omega_{\mathrm{pe}}$ region, the wave number k would have an imaginary part, so the wave would decay within a skin depth of the plasma, $L_{\mathrm{skin}} = c/\omega_{\mathrm{pe}}$. Where $\omega_0 = \omega_{\mathrm{pe}}$, the electron density $n_{\mathrm{c}} = 1.1 \times 10^{21}/\lambda^2\ \mathrm{cm}^{-3}$, where λ is the vacuum light wavelength in μm. This density is known as the critical density of the EM wave.

Although the dispersion relation, Eq. (2.10), has a simple expression, deriving it neglected the density and velocity gradient based on the assumption that the plasma is cold and close to homogeneous. However, when a laser is probing a small scale plasma, the inhomogeneity can cause anisotropy of the permittivity tensor and thereby change the polarization [71, 72]. The EM wave frequency ω_0 would also be shifted by the Doppler effect if propagating in a flowing plasma. The magnetic field in the longitudinal direction of the EM wave would also adjust the dispersion relation of a circularly polarized EM wave. Consequently, the magnetic field would rotate the polarization plane of a linearly polarized EM wave. This effect is known as the Faraday rotation, which is useful in diagnosing the magnetic field in the plasma [73]. Simulations show that under inertial confinement fusion (ICF) conditions Faraday rotation is usually more substantial than the depolarization caused by the plasma inhomogeneities [74].

2.2 Inverse-bremsstrahlung absorption

The electrons quivering in the EM wave may collide with ions and deposit their energy. As a result, the plasma absorbs the EM wave energy. This collisional absorption is known as inverse-bremsstrahlung absorption [75, 76, 77].

Adding the collision term into the momentum equation, Eq. (2.1), gives

$$\frac{\mathrm{d}\boldsymbol{u}_{\mathrm{e}}}{\mathrm{d}t} = -\frac{e}{m}\boldsymbol{E}(x)\exp(-\mathrm{i}\omega_0 t) - \frac{\nabla p_{\mathrm{e}}}{m_{\mathrm{e}} n_{\mathrm{e}}} - \sum_{\mathrm{j=ions}} (\boldsymbol{u}_{\mathrm{e}} - \boldsymbol{u}_{\mathrm{j}})\nu_{\mathrm{ej}}, \tag{2.12}$$

in which ν_{ej} is the Maxwell-averaged momentum-loss collision frequency between the electrons and the j-th ion species, and $\boldsymbol{u}_{\mathrm{j}} \approx 0$ is the ion velocity. The Maxwell-averaged momentum-loss collision frequency, in SI units, is

$$\nu_{\mathrm{ej}} = \frac{4(2\pi)^{1/2}}{3} n_{\mathrm{j}} \left(\frac{Z_{\mathrm{j}} e^2}{4\pi\epsilon_0 k T_{\mathrm{e}}}\right)^2 \left(\frac{k_{\mathrm{B}} T_{\mathrm{e}}}{m_{\mathrm{e}}}\right)^{1/2} \ln\Lambda \sim 9\times 10^{10} Z_{\mathrm{j}}^2 \left(\frac{n_{\mathrm{j}}}{10^{21}\ \mathrm{cm}^{-3}}\right)\left(\frac{k_{\mathrm{B}} T_{\mathrm{e}}}{1\ \mathrm{keV}}\right)^{-3/2} \ln\Lambda\ \mathrm{s}^{-1}, \tag{2.13}$$

where n_{j} is the ion density, and $\ln\Lambda$ is the Coulomb logarithm [78]. Since $\omega_0 > \omega_{\mathrm{pe}}$, the Coulomb logarithm would be a function of the laser frequency ω_0 [77]. The total momentum-loss collision frequency of an electron is

$$\nu_{\mathrm{ei}} = \sum_{\mathrm{j=ions}} \nu_{\mathrm{ej}}. \tag{2.14}$$

With the revised equation of motion Eq. (2.12), the dispersion relation of the EM wave in the collisional plasma becomes

$$\frac{k^2c^2}{\omega_0^2} = 1 - \frac{\omega_{\mathrm{pe}}^2}{\omega_0(\omega_0 + \mathrm{i}\nu_{\mathrm{ei}})}. \tag{2.15}$$

As seen, the wave vector $\boldsymbol{k}$ has an imaginary term. When $\nu_{\mathrm{ei}} \ll \omega_0$, the spatial damping rate of the energy is

$$\kappa_{\mathrm{ib}} \approx \frac{\nu_{\mathrm{ei}}}{c}\frac{n_{\mathrm{e}}}{n_{\mathrm{c}}}(1 - \frac{n_{\mathrm{e}}}{n_{\mathrm{c}}})^{-1/2}, \tag{2.16}$$

which is twice the imaginary part of the wave vector $\boldsymbol{k}$ since the wave energy is proportional to $|\boldsymbol{E}|^2$.

As a result, most of the laser energy would be absorbed in regions with densities close to critical density since the spatial absorption ratio increases with the density. In shock ignition, in which the keV coronal plasma has a length scale ~300 μm, the region with $n_{\mathrm{e}} > 0.2n_{\mathrm{c}}$ would absorb >80% of the laser energy if only the inverse-bremsstrahlung absorption is considered.

High plasma temperatures also inhibit the collisional absorption by lowering the collision rate between the electrons and the ions. Previous research has analyzed the absorption of the spike laser in large scale plasma at different temperatures, showing that, compared with the 2 keV case, the energy absorption region in the 4 keV plasma is closer to n_{c} [79].

2.3 Laser–plasma instabilities

The EM wave propagating in a plasma can be unstable because of wave resonance, which is known as laser–plasma instability (LPI). The plasma's electron waves and ion-acoustic waves can scatter the EM wave through Thomson scattering. The superposition of the scattered light and the incident light forms a beat wave, which drives an oscillating ponderomotive force that amplifies the electron or ion-acoustic wave and enhances the Thomson scattering. Thus, the scattering and wave amplification form a positive feedback loop that can grow exponentially. This section discusses the three major LPIs: i) stimulated Raman scattering, in which an EM wave is resonant with the scattered EM wave and an electron plasma wave, ii) stimulated Brillouin scattering, in which an EM wave and the scattered light are resonant with an ion-acoustic wave, iii) two-plasmon decay, in which an EM wave decays into two electron plasma waves. Because they may deplete the laser pump and generate hot electrons, understanding LPIs is key to assessing laser–shock energy conversion for shock ignition.

2.3.1 Stimulated Raman scattering

Stimulated Raman scattering (SRS) is the LPI that converts an EM wave into a secondary EM wave and an electron plasma wave. For the three waves to resonate, the frequencies and wave vectors of the secondary EM wave and the plasma wave need to match those of the primary wave:

$$\omega_0 = \omega_\mathrm{s} + \omega_\mathrm{p} \tag{2.17}$$

$$\boldsymbol{k}_0 = \boldsymbol{k}_\mathrm{s} + \boldsymbol{k}_\mathrm{p}, \tag{2.18}$$

where ω_0 $\boldsymbol{k}_0$ and ω_s $\boldsymbol{k}_\mathrm{s}$ are the angular frequencies and wave vectors of the primary EM wave and the scattered EM wave, respectively, which obey the dispersion relation Eq. 2.10, and ω_p and $\boldsymbol{k}_\mathrm{p}$ are the plasma wave's angular frequency and wave vector, respectively, which obey the Langmuir wave's dispersion relation:

$$\omega_\mathrm{p}^2 = \omega_\mathrm{pe}^2 + 3k_\mathrm{p}^2 v_\mathrm{th}^2, \tag{2.19}$$

in which $\omega_{\mathrm{pe}} = 4\pi e^2 n_e/m_{\mathrm{e}}$ is the plasma frequency and $v_{\mathrm{th}} = \sqrt{T_{\mathrm{e}}/m_{\mathrm{e}}}$ is the thermal velocity of the electrons. As discussed in Sec. 2.1, the existence of a secondary EM wave requires $\omega_{\mathrm{s}} > \omega_{\mathrm{pe}}$. Based on Eq. (2.17), ω_{pe} needs to be less than $\frac{1}{2}\omega_0$, which suggests that the SRS can only occur when $n_{\mathrm{e}} \lesssim 0.25 n_{\mathrm{c}}$. When the scattering occurs at $0.25n_{\mathrm{c}}$, the scattered light has zero group velocity. This instability is called absolute SRS [80] and it has a low threshold. When the instability happens in the $n_{\mathrm{e}} \ll 0.25n_{\mathrm{c}}$ region, all three waves propagate, so it is called convective SRS and has a higher intensity threshold.

When the three waves resonate, the amplitudes of the scattered light and the plasma wave grow exponentially. The amplitude growth rate is [18]

$$\gamma_0 = \frac{k_{\mathrm{p}} v_{\mathrm{os}}}{4} \left[\frac{\omega_{\mathrm{pe}}^2}{\omega_{\mathrm{p}}(\omega_0 - \omega_{\mathrm{p}})} \right]^{\frac{1}{2}}. \tag{2.20}$$

For a given density, this growth rate maximizes when k_{p} maximizes, which corresponds to the backscattering SRS.

The damping of the electron plasma wave and the scattering light can reduce the growth rate to γ_{eff}, which can be solved from

$$(\gamma_{\mathrm{eff}} + \gamma_{\mathrm{p}})(\gamma_{\mathrm{eff}} + \gamma_{\mathrm{s}}) = \gamma_0^2, \tag{2.21}$$

where γ_{p} is damping rate of the plasma wave's amplitude including both Landau damping and collisional damping:

$$\gamma_{\mathrm{p}} = \left(\frac{\pi}{8}\right)^{1/2} \frac{\omega_{\mathrm{p}}^2}{k_{\mathrm{p}}^3 {\lambda_{\mathrm{De}}}^3 \omega_{\mathrm{pe}}} \exp\left[-\frac{1}{2k_{\mathrm{p}}^2 \lambda_{\mathrm{De}}^2} - \frac{3}{2} \right] + \nu_{\mathrm{ei}}/2, \tag{2.22}$$

in which $\lambda_{\mathrm{De}} = \sqrt{T_{\mathrm{e}}/m_{\mathrm{e}}}/\omega_{\mathrm{pe}} = v_{\mathrm{th}}/\omega_{\mathrm{pe}}$ is the Debye length, ν_{ei} is the electron-ion collision frequency (discussed in Sec. 2.2), and the first term is the Landau damping rate given by Eq. (9.18) in Ref. [18]. Because of the exponential dependence of γ_{p} on $k_{\mathrm{p}}\lambda_{\mathrm{De}}$, when

$k_\mathrm{p}\lambda_\mathrm{De} \gtrsim 0.3$, strong Landau damping inhibits the growth of SRS. The amplitude collisional damping rate of the scattered EM wave is

$$\gamma_\mathrm{s} = \frac{\nu_\mathrm{ei}}{2}\left(\frac{\omega_\mathrm{pe}}{\omega_\mathrm{s}}\right)^2. \tag{2.23}$$

Thus, $\gamma_\mathrm{eff} > 0$ is the threshold for SRS growth in a homogeneous plasma.

In an inhomogeneous plasma, the growth of SRS is limited by the coherent length of the three waves. The wave numbers k_0, k_s, and k_p shift during wave propagation, breaking the wave vector matching condition, thereby limiting the coherent length. The coherent length, known as the interaction length l_int, can be estimated as the propagation distance covered as the phase difference grows to π, which can be expressed as

$$\int_0^{l_\mathrm{int}} [k_0(z) - k_\mathrm{s}(z) - k_\mathrm{p}(z)]\mathrm{d}z \sim \frac{1}{2}. \tag{2.24}$$

The difference of wave vectors, $k_0(z) - k_\mathrm{s}(z) - k_\mathrm{p}(z)$, can be defined as $\Delta k(z)$. Because of the matching condition, $\Delta k(z)$ is approximately equal to its first-order Taylor expansion, $\Delta k' z$. As a result, $l_\mathrm{int} \sim \sqrt{1/\Delta k'}$. The waves need to grow in the interaction region, so the instability threshold to have an e-fold growth of the wave amplitude becomes

$$\gamma_\mathrm{eff}^2 \frac{l_\mathrm{int}^2}{v_\mathrm{gs} v_\mathrm{gp}} > 1, \tag{2.25}$$

where v_gs and v_gp are the group velocities of the scattered light and plasma wave, respectively. [81] The interaction distance depends on the plasma's length scale since $\Delta k'$ is inversely proportional to the length scale of the plasma $L_n = n_\mathrm{e}(z)(\partial n_\mathrm{e}/\partial z)^{-1}$. As a result, SRS can grow to a higher amplitude in a plasma with a larger scale length. The intensity thresholds of the convective ($n_\mathrm{e} \ll n_\mathrm{c}/4$) and absolute SRS ($n_\mathrm{e} \sim n_\mathrm{c}/4$) are summarized in

Ref. [82]:

$$I_{\mathrm{con,SRS}} = \frac{4\times10^{17}}{L_n(\mu\mathrm{m})\lambda_0(\mu\mathrm{m})}\mathrm{W/cm^2} \tag{2.26}$$

$$I_{\mathrm{abs,SRS}} = \frac{5\times10^{16}}{L_n^{4/3}(\mu\mathrm{m})\lambda_0^{2/3}(\mu\mathrm{m})}\mathrm{W/cm^2}. \tag{2.27}$$

For shock ignition where $L_n \sim 300$ μm and $\lambda_0 = 0.351$ μm, the convective SRS intensity threshold is $\sim 4\times10^{15}$ W/cm^2 and the absolute SRS threshold is $\sim 5\times10^{13}$ W/cm^2. Both are below the required intensity of the spike pulse.

SRS generates hot electrons. The damping or breaking of the plasma waves converts the wave energy to kinetic energy in the wave-trapped electrons. Particle-in-cell simulations [83] suggest that the temperature of the accelerated hot electrons is approximately equal to the kinetic energy of an electron moving with the plasma wave's phase velocity ($v_{\mathrm{ph}} = \omega_{\mathrm{p}}/k_{\mathrm{p}}$):

$$T_{\mathrm{hot}} \sim m_{\mathrm{e}} v_{\mathrm{ph}}^2/2. \tag{2.28}$$

For the backscattering SRS, the hot electron temperatures depend on the local density. Since k_{p} decreases and ω_{p} increases as the density increases, the phase velocity increases with plasma density. This estimate implies that the backscattering SRS near the $n_{\mathrm{c}}/4$ region would generate the hottest electrons, $T_{\mathrm{hot}} \sim 70$ keV. The experiments presented in this dissertation measured the wavelength of the scattered light, which can indicate the local density of the SRS source, $k\lambda_{\mathrm{De}}$, and T_{hot} as shown in Fig. 2.1. The role of these hot electrons in shock ignition is introduced in Sec. 2.5.2.

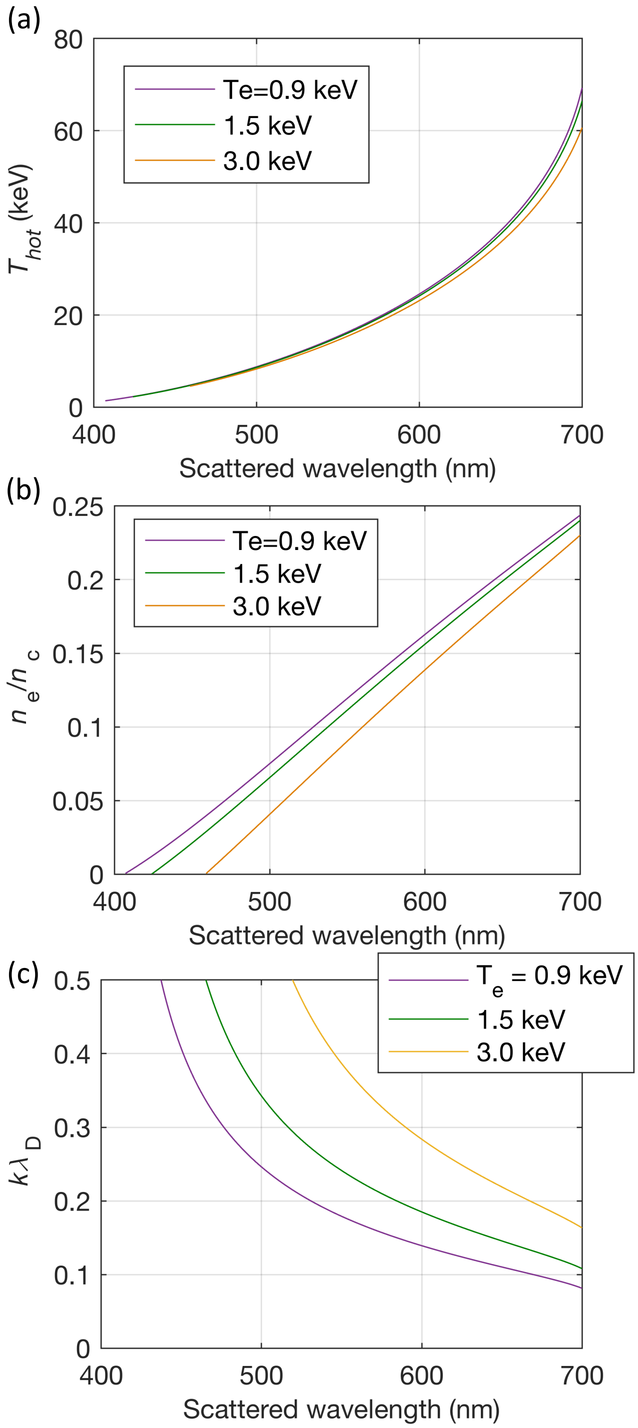

Figure 2.1: The dependence of (a) the SRS-induced hot electron temperature, (b) plasma density, (c) $k_\mathrm{p}\lambda_\mathrm{De}$ on the wavelength of the measured scattered light. The incident laser's wavelength is 351 nm.

2.3.2 Two-plasmon decay

An EM wave can decay into two electron plasma waves through two-plasmon decay (TPD), in which the wave frequency and vector matching conditions are

$$\omega_0 = \omega_{\mathrm{p1}} + \omega_{\mathrm{p2}} \tag{2.29}$$

$$\boldsymbol{k}_0 = \boldsymbol{k}_{\mathrm{p1}} + \boldsymbol{k}_{\mathrm{p2}}. \tag{2.30}$$

Since ω_{p1} and ω_{p2} are approximately equal to ω_{pe}, the instability would happen near the $n_{\mathrm{c}}/4$ region where $\omega_{\mathrm{pe}} \approx \omega_0/2$.

For a homogeneous plasma, the growth rate of TPD can be expressed as [18]

$$\gamma(\boldsymbol{k}) \simeq \frac{\boldsymbol{k}\cdot\boldsymbol{v}_{\mathrm{os}}}{4}\left|\frac{(\boldsymbol{k}-\boldsymbol{k}_0)^2 - k^2}{k|\boldsymbol{k}-\boldsymbol{k}_0|}\right|, \tag{2.31}$$

in which $\boldsymbol{k} = k_x\hat{x} + k_z\hat{z}$ is wave vector of one plasma wave, $\hat{x}$ is the direction of the laser's electric field, $\hat{z}$ is the laser's longitudinal direction, and $\boldsymbol{k_0} - \boldsymbol{k}$ is the wave vector of the other plasma wave.

The dependence of the TPD growth rate on k_x and k_z, as shown in Fig. 2.2, suggests that the growth rate peaks when $k_x \sim k_z$ for $k \gg k_0$. This feature implies that in the region away from $n_{\mathrm{c}}/4$, the largest TPD-induced plasma waves propagate at $\sim 45^\circ$ off the laser direction, resulting in TPD-generated hot electrons with a wide divergence, which is confirmed experimentally. [84]

2.3.3 Stimulated Brillouin scattering

Stimulated Brillouin scattering (SBS) is a process that can convert the EM wave into an EM wave of the scattered light and an ion-acoustic wave. Like SRS and TPD, SBS

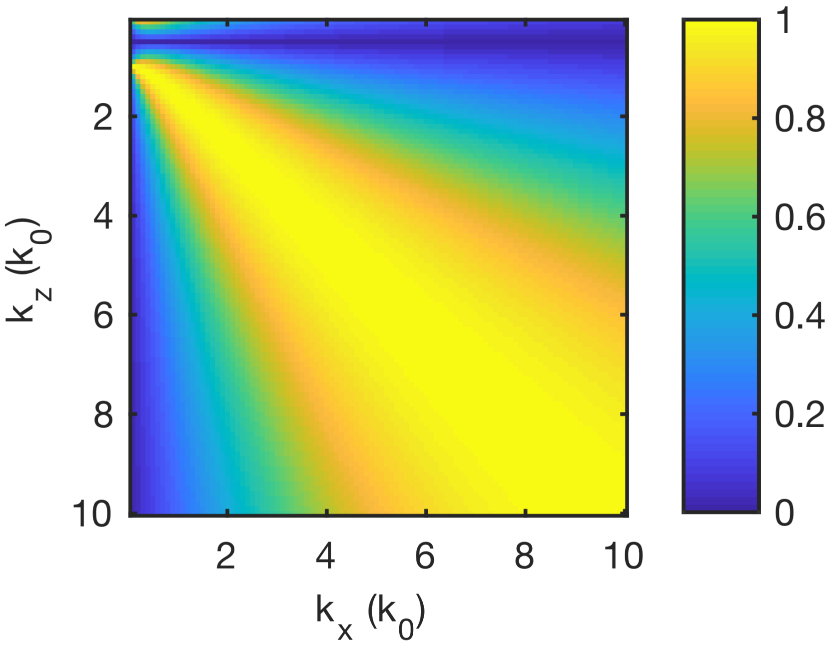

Figure 2.2: The dependence of TPD growth rate γ on k_x and k_z following Eq. (2.31). γ in this figure is in units of $v_{\mathrm{os}}k_0/4$.

follows the wave frequency and wave vector matching conditions

$$\omega_0 = \omega_{\mathrm{s}} + \omega_{\mathrm{i}}, \tag{2.32}$$

$$\boldsymbol{k}_0 = \boldsymbol{k}_{\mathrm{s}} + \boldsymbol{k}_{\mathrm{i}}, \tag{2.33}$$

in which the ion-acoustic wave's frequency ω_{i} and wave vector $\boldsymbol{k}_{\mathrm{i}}$ would obey its dispersion relation. The dispersion relation is the zeros of the plasma dielectric function $\epsilon(k,\omega)$ as shown in Eq. (1) of Ref. [85]:

$$\epsilon(k,\omega) = 1 + \chi_{\mathrm{e}} + \sum_j \chi_{\mathrm{i}j} = 0, \tag{2.34}$$

in which χ_e is the electron susceptibility, and $\chi_{\mathrm{i}j}$ is the ion susceptibility of the j^th species. The susceptibilities are functions of the plasma dispersion function $Z(\xi)$ [86]:

$$\chi_\mathrm{e} = -\frac{\omega_\mathrm{pe}^2}{2k^2 v_\mathrm{e}^2} Z'\left(\frac{\omega}{\sqrt{2}kv_\mathrm{e}}\right) \tag{2.35}$$

$$\chi_{\mathrm{i}j} = -\frac{\omega_{\mathrm{pi}j}^2}{2k^2 v_{\mathrm{i}j}^2} Z'\left(\frac{\omega}{\sqrt{2}kv_{\mathrm{i}j}}\right), \tag{2.36}$$

where $v_{\mathrm{i}j}$ is the j^th ion species's thermal velocity $\sqrt{T_\mathrm{i}/m_{\mathrm{i}j}}$, and $\omega_{\mathrm{pi}j}$ is this ion species's ion-plasma frequency. The plasma dispersion function $Z(\xi)$ was originally expressed in Ref. [87]. The dispersion relation, Eq. (2.34), can be simplified to

$$\omega_\mathrm{i} = c_\mathrm{s} k_\mathrm{i}, \tag{2.37}$$

where c_s is the sound velocity $\sim \sqrt{ZT_\mathrm{e}/m_\mathrm{i}}$, where Z is the ionization level. The sound velocity is about $0.1\% c$ for a 1-keV H^+ plasma. For SBS, $k_\mathrm{i} < 2k_0$ and $\omega_\mathrm{i} < 2c_\mathrm{s}/c$, leading to $\omega_\mathrm{i} \ll \omega_0$. As a result, only a small fraction ($\omega_\mathrm{i}/\omega_0$) of the laser energy involved in SBS can be absorbed, with the majority of the energy scattered. For a plasma consisting of two ion species, two modes of ion-acoustic waves can exist according to the dispersion relation Eq. (2.34). Solving Eq. (2.34) would also give the sound velocity for each mode.

Similar to backscattering SRS, backscattering SBS has the largest growth rate since it is proportional to $\sqrt{k_\mathrm{i}}$ as

$$\gamma_\mathrm{SBS} = \frac{\omega_\mathrm{pi} v_\mathrm{os} \sqrt{k_\mathrm{i}}}{4\sqrt{\omega_\mathrm{s} c_\mathrm{s}}} \tag{2.38}$$

according to Eq. (8.11) in Ref. [18]. Since $\omega_\mathrm{i} \ll \omega_0$ and $\omega_\mathrm{s} \approx \omega_0$, the growth rate peaks when k_i maximizes, which occurs when the scattered light is going backwards ($k_\mathrm{i,max} \approx 2k_0$). However, as a result of laser filamentation and side scattering, a large fraction of the Brillouin-reflected light would go out of the lens. Experiments [88, 89] and simulations [90] have shown that, under strong scattering conditions (reflectivity> 60%), the energy in the side-scattered light is about 1–4 times the energy of backscattering.

The growth rate above is derived under the assumption of weak coupling, $\gamma_{\mathrm{SBS}} \ll k_{\mathrm{i}} c_{\mathrm{s}}$. For strong coupling, $\gamma_{\mathrm{SBS}} \gg k_{\mathrm{i}} c_{\mathrm{s}}$, the dispersion relation of SBS becomes

$$\omega \simeq {\frac{k_0^2 v_{\mathrm{os}}^2 \omega_{\mathrm{pi}}^2}{2\omega_0}}^{1/3} \left[\frac{1}{2} + \mathrm{i}\frac{\sqrt{3}}{2}\right]. \tag{2.39}$$

In shock ignition, the strong coupling mode of SBS may occur with certain laser intensities and plasma densities. In the rest of this dissertation, strong coupling SBS is not considered since $\gamma_{\mathrm{SBS}} \lesssim k_{\mathrm{i}} c_{\mathrm{s}}$ in these experiments.

Unlike SRS, the threshold of SBS is determined by the scale length of the flow velocity, especially in inertial confinement fusion, since the inhomogeneity of the flow velocity can cause Doppler shifts for all three waves, breaking coherence. The inhomogeneity of the plasma's expanding velocity can be described by the velocity scale length as

$$L_v = \frac{c_{\mathrm{s}}}{\partial u(x)/\partial x}, \tag{2.40}$$

where $u(x)$ is the local plasma expanding velocity. In 1-dimensional conditions, $L_v \sim L_n \sim c_{\mathrm{s}} t$ [91]. The threshold of SBS limited by the velocity inhomogeneity is [82]

$$I_{\mathrm{t,SBS}} \simeq \frac{7 \times 10^{15}}{L_v(\mu\mathrm{m})\lambda_0(\mu\mathrm{m})} T_{\mathrm{e}}(\mathrm{keV}) \frac{n_{\mathrm{c}}}{n_{\mathrm{e}}}\ \mathrm{W/cm^2}. \tag{2.41}$$

In shock ignition, where $L_v \sim$ 300 μm and $T_{\mathrm{e}} \sim 3$ keV, the $\sim 10^{16}$ W/cm^2 intensity of the spike laser ($\lambda_0 = 0.351$ μm) exceeds the SBS threshold in the $n_{\mathrm{e}} > 0.02 n_{\mathrm{c}}$ region.

Because of the low threshold and high growth rate, SBS can strongly affect shock ignition through its strong scattering. particle-in-cell and fluid-model simulations suggest that SBS can reflect over 50% of laser light [33, 34, 35, 90]. Previous experiments have used calorimeters to measure the energy of backscattering, side-scattering, and plasma absorption. In these experiments, the SBS in a preformed plasma reflected > 60% of the energy of a ~ 10^{16} W/cm^2 laser [88, 89, 92, 93].

SBS saturates when the amplitude of the ion-acoustic wave reaches its limit. Wave breaking (strong trapping) may occur when the ion's quivering velocity is close to the wave's phase velocity:

$$Ze\phi = m_{\mathrm{i}} v_{\mathrm{quiver}}^2/2 = m_{\mathrm{i}} c_{\mathrm{s}}^2/2, \tag{2.42}$$

where ϕ is the potential of the wave. The density perturbation in this ion-acoustic wave δn is also related to the potential:

$$\delta n/n_0 \simeq e\phi/T_{\mathrm{e}}. \tag{2.43}$$

When the ions are heated, the wave breaking condition becomes

$$Ze\phi = \frac{M}{2}\left(c_{\mathrm{s}} - \sqrt{3}v_{\mathrm{i}}\right)^2 \tag{2.44}$$

under an assumption of a waterbag distribution (constant in $[-\sqrt{3}v_{\mathrm{i}}, +\sqrt{3}v_{\mathrm{i}}]$), where $v_{\mathrm{i}} = \sqrt{T_{\mathrm{i}}/m_{\mathrm{i}}}$ is the ion's thermal velocity. This model suggests that when the ions are heated up, a possible consequence of SBS, the wave breaking reduces the wave amplitude as well as the reflectivity nearly to zero. This wave breaking model can explain the slow laser penetration observed in experiments. The model–experiment comparison is presented in Ch. 4.

Besides wave breaking, ion-trapping would also detune the SBS and limit reflectivity, which is observed in experiments [94]. The ion-trapping can shift the frequency of the ion-acoustic wave by

$$\frac{\delta\Omega}{\omega_j} \approx -\eta\left(\frac{\delta n}{n_\mathrm{e}}\right)^{1/2}, \tag{2.45}$$

in which ω_j is the frequency of the ion-acoustic wave dominated by the j^{th} ion species, and the detuning parameter η is

$$\eta = -\frac{f_j}{\sqrt{2\pi}}(v^4 - v^2)\exp(-v^2/2)\sqrt{Z_j T_\mathrm{e}/T_\mathrm{i}}, \tag{2.46}$$

where $v = c_\mathrm{s}/v_{\mathrm{i}j} \sim \sqrt{Z_j T_\mathrm{e}/T_\mathrm{i}}$ since $v_{\mathrm{i}j} = \sqrt{T_\mathrm{i}/m_j}$ is the thermal velocity of the j^{th} ion species; f_j is the number fraction of the j^{th} ion species. Because of the exponential dependence, the detuning parameter η is sensitive to Z_j. If $T_\mathrm{e}/T_\mathrm{i} = 3$, η for Be^{4+} would be 7 times higher than for C^{6+}. This Z dependence implies that detuning would more effectively suppress the SBS with the low-Z ion mode.

2.4 Laser filamentation

A laser beam may break into filaments during its propagation in a plasma, which can increase the local intensity and enhance LPIs. Laser filamentation can be driven by several mechanisms such as laser ponderomotive forces [95], thermal forces [96], and relativistic effect [97].

Similar to SBS, ponderomotive-force-induced filamentation is a mutual amplification between the perturbations of the density and the EM waves. The nonuniformity of the laser intensity profile would create ponderomotive force in the transverse direction, which pushes the electrons and ions out, reducing the local density and increasing the refractive index according to Eq. (2.10). The local high refractive index focuses the laser and further increases the ponderomotive force. These processes form a positive feedback loop.

According to Eq. (19) in Ref. [95], the relation between the filamentation's spatial growth rate κ and the perturbation wave vector in the laser's transverse direction k_y can be expressed as

$$4k_0^2\kappa^2 = (E_0^2\epsilon'\frac{\omega^2}{c^2} - k_y^2)k_y^2, \tag{2.47}$$

where E_0 is peak electric field in the laser EM wave, and the plasma dielectric constant is

$$\epsilon = 1 - \left(\frac{\omega_{\rm pe}}{\omega_0}\right)^2 = 1 - \left(\frac{\omega_{\rm pe0}}{\omega_0}\right)^2 \exp\left[\frac{-e^2\langle E^2\rangle}{2m_{\rm e}\omega_0^2(T_{\rm e}+T_{\rm i})}\right] \tag{2.48}$$

and

$$\epsilon' = \frac{\partial\epsilon}{\partial\langle E^2\rangle} = \left(\frac{\omega_{\rm pe0}}{\omega_0}\right)^2 \frac{e^2}{2m_{\rm e}\omega_0^2(T_{\rm e}+T_{\rm i})}\exp\left[\frac{-e^2\langle E^2\rangle}{2m_{\rm e}\omega_0^2(T_{\rm e}+T_{\rm i})}\right], \tag{2.49}$$

where $\langle E^2\rangle = E_0^2/2$ is the averaged square of the electric field in the EM wave, and $\omega_{\rm pe0}$ is the original plasma frequency without the density perturbation. Based on Eq. (2.47), the mode that has the largest growth rate would have

$$k_y^2 = \frac{1}{2}(E_0^2\epsilon')\frac{\omega^2}{c^2}. \tag{2.50}$$

Substituting ϵ',

$$k_{y,\max} = \frac{\omega}{c}\frac{\omega_{\rm pe0}}{\omega_0}\sqrt{\frac{m_{\rm e}v_{\rm os}^2}{4(T_{\rm e}+T_{\rm i})}}\exp\left[\frac{-m_{\rm e}v_{\rm os}^2}{4(T_{\rm e}+T_{\rm i})}\right]. \tag{2.51}$$

This k_y expression is different from Eq. (21') in Ref. [95] since that equation included a mistake and did not explicitly define $V_{\rm T}$.

Substituting Eq. (2.51), the largest spatial growth rate is

$$\kappa_{\max} = \frac{k_{y,\max}^2}{2k_0}. \tag{2.52}$$

Thus,

$$\kappa_{\max} = \frac{k_0}{8}\frac{\omega_{\mathrm{pe0}}^2}{\omega_0^2}\frac{m_{\mathrm{e}}v_{\mathrm{os}}^2}{T_{\mathrm{e}}+T_{\mathrm{i}}}\left[1-\left(\frac{\omega_{\mathrm{pe0}}}{\omega_0}\right)^2\right]^{-1}\exp\left[\frac{-m_{\mathrm{e}}v_{\mathrm{os}}^2}{2(T_{\mathrm{e}}+T_{\mathrm{i}})}\right], \tag{2.53}$$

and $1/\kappa_{\max}$ is the critical plasma length L_{c} for the filamentation to grow.

In the dissertation's experiments, the UV laser creating the plasma generated the filamentation in the $0.1-0.25n_{\mathrm{c}}$ region. The UV laser had $\lambda_{\mathrm{L}} = 0.351$ μm and 2×10^{14} W/cm^2; thus, $m_{\mathrm{e}}v_{\mathrm{os}}^2 = 9$ eV. The plasma it created had $T_{\mathrm{e}} = 1.5$ keV and $T_{\mathrm{i}} = 0.5$ keV. In this condition, the critical length would be $L_{\mathrm{c}} \sim 600$ μm and $k_{y,\max} = 0.012k_0$, which suggests that the filaments have a perturbation width of $2\pi/k_{y,\max} \sim 80\lambda_{\mathrm{L}} \sim 30$ μm.

2.5 Ignition shock generation

As discussed in Sec. 1.4, the spike laser in shock ignition needs to convert sufficient energy to generate a shock that has >300 Mbar ablation pressure. [30] In shock ignition, two mechanisms may convert the energy: collisional absorption and direct heating by the hot electrons.

2.5.1 Ablation by collisional absorption

As discussed in Sec. 2.2, the laser deposits its energy into the plasma through the collision between the quivering electrons and ions, which is known as inverse-bremsstrahlung. Since the absorption rate is proportional to n_{e}^2 and the laser can only propagate in the region with $n_{\mathrm{e}} < n_{\mathrm{c}}$, most of the laser energy would be absorbed near the n_{c} region. Then, this energy diffuses into the denser region through thermal diffusion, which heats the dense shell. The heated shell expands outward acting as the rocket's jet, forming an ablation pressure to drive the inward shock.

The scaling law for the ablation pressure has been developed by C. Max et al. [31, 98, 99]. When the flux limiter is assumed to be $f = 0.1$, the ablation pressure p_{a} can be expressed as Eq. (A3) in Ref. [31]

$$p_{\mathrm{a}} \simeq 9.0\left[\left(\frac{I_{\mathrm{P}}}{10^{14}\ \mathrm{W/cm^2}}\right)^{0.67}\left(\frac{1\ \mu\mathrm{m}}{\lambda_{\mathrm{L}}}\right)^{0.67}\right]\ \mathrm{Mbar} \tag{2.54}$$

where I_{P} is the absorbed laser power divided by $4\pi R_{\mathrm{a}}^2$, and R_{a} is the radial position of the ablation front. The absorption intensity at the critical position (r_{c}) is $I_{\mathrm{c}} = I_{\mathrm{P}}(R_{\mathrm{a}}/r_{\mathrm{c}})^2$. Typically, $R_{\mathrm{a}}/r_{\mathrm{c}}$ is about 0.7–1 according to the scaling law Eq. (A1) and (3) in Ref. [31]. According to Eq. (2.54), to achieve the required 300 Mbar ablation pressure, the absorbed intensity at the ablation front needs to reach $\sim 6.5\times10^{15}$ W/cm^2. Under the assumption of a 50% energy absorption rate and $R_{\mathrm{a}} \sim 0.85 r_{\mathrm{c}}$, this ablation pressure requires lasers with $\lambda_{\mathrm{L}} = 0.351$ µm to have an overlapped intensity $\sim 10^{16}$ W/cm^2 at the critical density surface.

2.5.2 Ablation by super-thermal electrons

The LPI-induced hot electrons may be capable of driving the ignition shock. [47] This mechanism is efficient since the hot electrons can deposit the energy where the shock is generated, rather than heating up the sub-critical coronal plasma hundreds of micrometers away from the shock.

The shock generated by stopping the monoenergetic intense hot electron beam was first discussed in Ref. [47]. References [48, 49] discussed the shock generated by the hot electrons in an exponential energy distribution. When an intense hot electron beam hits a compressed (10 g/cm^3) Deuterium–Tritium shell, the beam can heat up the shell in the electrons' stopping range. The heated shell would generate rarefaction wave, leading to a shock moving forward. The stopping range (ρR_0) of the DT shell is related to the hot electron energy ϵ_0 by

$$\rho R_0 = \frac{2}{5}\frac{\epsilon_0^2}{S_0}, \tag{2.55}$$

where $S_0 = \pi e^4 Z \ln \Lambda / m_{\mathrm{i}}$. [49] For an exponential distribution, the average stopping range $\rho R_{\exp}$ has been derived in Ref. [48] as

$$\rho R_{\exp} = \frac{3}{2} \frac{T_h^2}{S_0}. \tag{2.56}$$

Thus, the average stopping range of electrons with energy exponentially distributed is close to that of a monoenergetic electron beam with $\epsilon_0 = \sqrt{15/4} T_{\mathrm{h}}$. For example, the T = 30 keV electrons would have an averaged stopping range of 6.5 mg/cm^2, which is close to the stopping range of a 60-keV monoenergetic electron beam. [47, 48]

The stopping range ρR, the shell density ρ, and the electron beam intensity on the shell I_{b} determine the loading time t_{h} and the peak pressure p_{h}. Loading time t_{h} is the time for the shock to reach its peak pressure. It is also the time for the rarefaction wave to pass the heated zone. The rarefaction wave propagates at the sound speed $c_{\mathrm{s}} \sim \sqrt{ZT/m_{\mathrm{i}}}$; thus, $t_{\mathrm{h}} \sim x_{\mathrm{h}}/c_{\mathrm{sh}}$, in which c_{sh} is the maximum sound speed and $T = \frac{I_{\mathrm{b}} t_{\mathrm{h}}}{3(Z+1) n_{\mathrm{i}} x_{\mathrm{h}}}$. Ref. [49] summarizes this model and gives scaling laws for t_{h} and P_{h}:

$$t_{\mathrm{h}} \sim 0.111 (\rho R) I_{\mathrm{b}}^{-1/3} \rho^{-2/3} \text{ ns} \tag{2.57}$$

$$P_{\mathrm{h}} \sim 175 I_{\mathrm{b}}^{2/3} \rho^{1/3} \text{ Mbar}, \tag{2.58}$$

where I_{b} is in units of 10^{15} W/cm^2, ρ is the compressed shell density in g/cm^3, and ρR is the average stopping range in mg/cm^2.

Compared with the shock generated by monoenergetic ϵ_0 electrons, an electron beam with an exponential energy distribution ($T_{\mathrm{h}} = 0.516 \epsilon_0$, same average stopping range ρR) would preheat the upstream region and reduce the shock strength, P_2/P_1, in which P_2 is the downstream shock pressure and P_1 is the upstream pressure [48]. However, in both cases, the shock pressure P_2 would reach the same maximum pressure P_{h} at the shock loading time t_h. Then, P_2/P_1 of the shock generated by the exponential electron beam would continue growing and reach its maximum at ~ $3t_\mathrm{h}$. At that time, the shock front reaches $3x_\mathrm{h}$. In addition, the shock strengths at ~ $3t_\mathrm{h}$ are similar in both cases.

According to this model, using hot electrons to generate a 300 Mbar shock in a 10 g/cm^3 compressed DT shell would require an electron beam with $I_\mathrm{b} > 7 \times 10^{14}$ W/cm^2 on the shell surface. If the electrons have a temperature of about 50 keV, the beam duration needs to be longer than $t_\mathrm{h} = 0.4$ ns for the shock pressure to reach 300 Mbar. The average stopping depth for this T_h = 50 keV beam would be x_h = 15 μm. The shock would have its maximum strength when passing through the outer ~45 μm of the shell. As a result, the hot electron temperature and the beam intensity would limit the design space of the shock ignition's capsule.

Chapter 3

Experimental and Simulation Methods

As discussed previously, shock ignition requires the laser spike pulse to generate a ~300 Mbar shock. The energy conversion from the laser to the shock depends on the laser–plasma instabilities and the generation of the hot electrons. The dissertation's experiments conducted at the OMEGA EP and OMEGA-60 laser facilities characterized the hot electrons and the nonlinear laser–plasma instabilities under high intensities (~10^{16} W/cm^2) and large plasma length-scales, $L_n \sim 300 - 500$ µm. In these experiments, the hot electrons were quantified by diagnosing bremsstrahlung x-rays as well as the Cu K-shell fluorescence. The plasma perturbation induced by the laser–plasma instabilities has also been captured by using the angular filter refractometer and shadowgraphy images. The stimulated Raman and Brillouin scattering were measured using the subaperture backscattering spectrometers on OMEGA EP. Radiation–hydrodynamic simulations were performed using open source code FLASH to simulate the plasma formation process. GEANT4 Monte Carlo code was used to simulate bremsstrahlung emission and infer the hot electron temperatures and energies. The laser facilities, diagnostics, data analyses, and simulation tools used for these projects are discussed in this chapter.

3.1 OMEGA EP and OMEGA 60-beam laser facilities

OMEGA EP (Extended Performance) and OMEGA (60-beam) are the multi-beam laser facilities built and operated by the Laboratory and Laser Energetics at the University of Rochester. OMEGA EP has four kilojoule-class laser beamlines. All four beams can be frequency-tripled ($\lambda_L = 0.351$ μm) UV lasers. These lasers can provide 0.1–10 ns pulses at up to 1 TW per beam. The pulses of two beams can be compressed to 700 fs–100 ps without a frequency convestion ($\lambda_L = 1.054$ μm) using optical parametric chirped-pulse amplification (OPCPA) [100, 101]. Consequently, the IR pulse has a broad 3 nm bandwidth. All four beams were integrated with a frequency modulator resulting in a bandwidth of 0.1 THz for the UV light, which suppresses the stimulated Brillouin scattering in the optical system. [102] The UV beams are focused by $f/6.5$ lenses. Distributed phase plates [103] can be installed for the UV beams to smooth the beam profile and create a super-Gaussian focal spot. IR beams are focused by the off-axis parabolic mirrors (OAP). The beam profile incident on the OAP (near-field) is a square of 32 cm and the OAP has a 1 m focal length. Thus, the IR beams have a focal ratio of $f/3.2$. In addition, the two IR beams can be focused by the same OAP in co-propagation mode, which can combine two 100 ps pulses into a single 200 ps pulse.

The OMEGA-60 laser facility has 60 beamlines, powered by nanosecond UV lasers which can deliver a total of 30 kJ energy onto the target with a peak power of 0.5 TW per beam. These lasers are spherically distributed around the chamber, resembling a soccer ball. The short-pulse IR lasers of OMEGA EP can also be injected into the OMEGA-60 chamber.

These nanosecond kilojoule-class lasers are ideal to study the laser–plasma instabilities for shock ignition. In the experiments presented in this dissertation, the UV lasers with phase plates acted as the implosion pulse of shock ignition, irradiating the target with intensities of $10^{14} - 10^{15}$ W/cm^2 to create the large and hot plasma. 1–2 ns after the onset of the low-intensity lasers, ~10^{16} W/cm^2 UV or IR lasers were injected, acting as the spike pulse in shock ignition. When using the UV laser, this intensity was achieved by tightly focusing the laser to a spot of 80–100 μm in diameter, at 1 TW per beam in a 1-ns pulse. The IR lasers (up to 2.5 kJ, 100 ps pulse) were set to have a ~300 μm diameter spot on the plasma's quarter critical density surface ~1 mm above the target surface. At this location, the laser is still focusing, and the best focus is near the target surface.

3.2 Target design

Two major target types were used in these experiments: a 3-layer disk and a multilayer sphere, as shown in Fig. 3.1 and Fig. 3.2, respectively. The basic 3-layer disk target comprises a CH layer of 25 μm Parylene-N (PN) or polystyrene (PS), coated (PN) or glued (PS) onto a 20 μm Cu layer, which is attached to a 50 μm Al layer. The Al layer is used to provide extra stopping power for the hot electrons and inhibit electron refluxing. A revised version of the planar target has a low-density (1.1 g/cm^3) Cu foam cylinder glued to the back of the CH layer, as shown in Fig. 3.1(b). These planar targets were used in the OMEGA EP experiments.

The spherical targets used in the OMEGA-60–OMEGA EP joint experiments are of two types. One type has a 1.2 g/cm^3 Cu foam ball coated with a layer of 30 μm PN, as shown in Fig. 3.2(a). In the coating process, PN penetrated ~85 μm deep into the foam and filled about 30% of the pore space. The penetration depth was measured using a scanned electron microscope (SEM) to image the cross-section of a target that has been cut in half. The space fill ratio is inferred from the mass difference of the target before

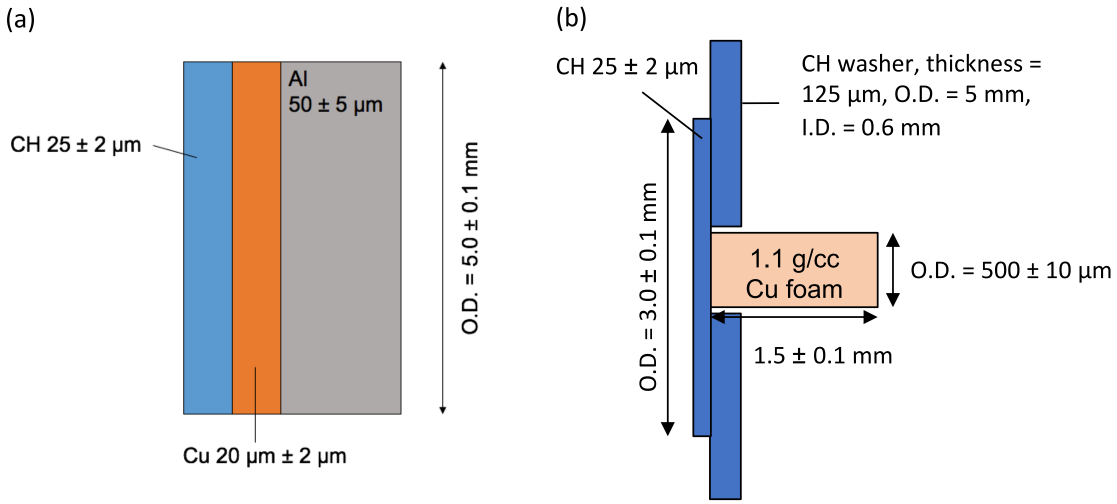

Figure 3.1: Planar target configuration. (a) 3-layer disk target. (b) Cu foam cylinder target.

and after coating. The other spherical target, as shown in Fig. 3.2(b), has an 8 µm layer of Cu/B co-sputtered onto a CH bead. A 30 µm PN layer is then coated onto the Cu/B layer. The co-sputtering is applied to reduce the surface roughness (<1 µm). The average Cu density in this layer is 6.5 g/cm^3.

3.3 Diagnostics and analysis tools

3.3.1 Bremsstrahlung spectrum measurement

The main method for measuring the hot electrons is diagnosing the spectra of the bremsstrahlung x-rays using a Bremsstrahlung MeV X-ray Spectrometer [69]. The deceleration of the hot electrons in the target emits hard x-rays through the bremsstrahlung process. Fitting synthetic spectra from Monte Carlo simulations to the measured spectra gives the hot electrons' temperatures and energies.

The two BMXSs used in this project are identical. Each of them has a stack of 15 filters alternating with 15 image plates. These filters and image plates are placed inside

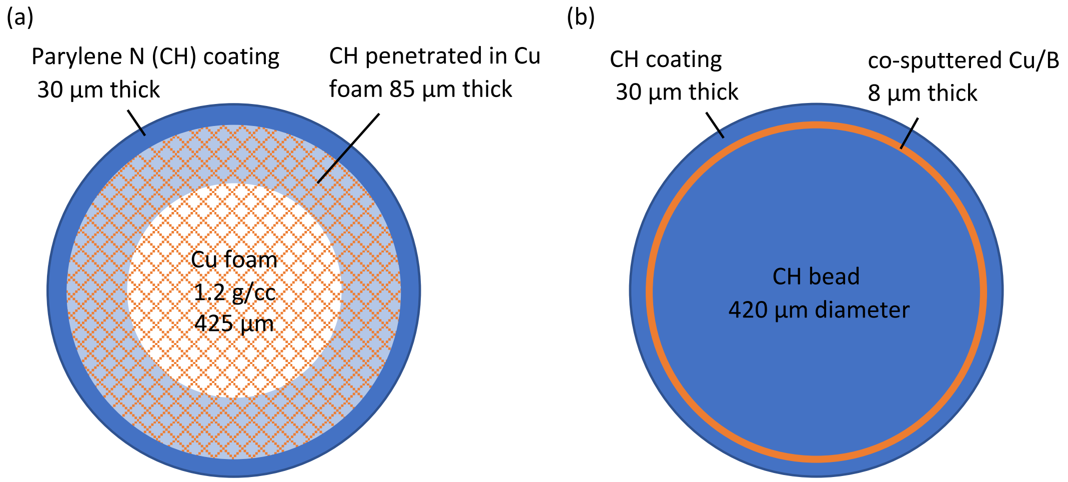

Figure 3.2: Spherical target configuration. (a) Cu foam ball target. (b) CH ball target with a Cu layer embedded.

a Delrin cartridge loaded into a lead housing. The filters are listed in Fig. 3.3. In the OMEGA EP experiment, BMXSs were placed outside of a 3 mm Kodial Borosilicate glass window. The distance from the detector aperture to the target chamber center (TCC) is 190.3 cm. The visible field of view is 5.11 cm at the target chamber center (TCC). The completely visible field of view is 0.95 cm at TCC, which is much larger than a typical size of the target (~5 mm). In the OMEGA-60 chamber, the BMXS is placed 1.34 m away from the TCC. Blast shields made of 100 µm Al + 250 µm PET covered the front of the BMXS in our 2016 experiments. In the 2018 experiments, it was placed 1.92 m from the TCC, covered by blast shields made of 25 µm Al + 250 µm PET. The low-energy filter pack was used in the 2018 experiments; the high-energy filter pack was used in other experiments.

Since each image plate is filtered by a different filter components, the image plates respond differently to x-rays. Their response functions are shown in fig. 3.4. These response functions are calculated by using integrated TIGER series (ITS) 3.0 Monte Carlo simulation code [70]. These simulations calculated the deposited energy on the active layer of each image plate from x-ray bins, which were logarithmically spaced into 150

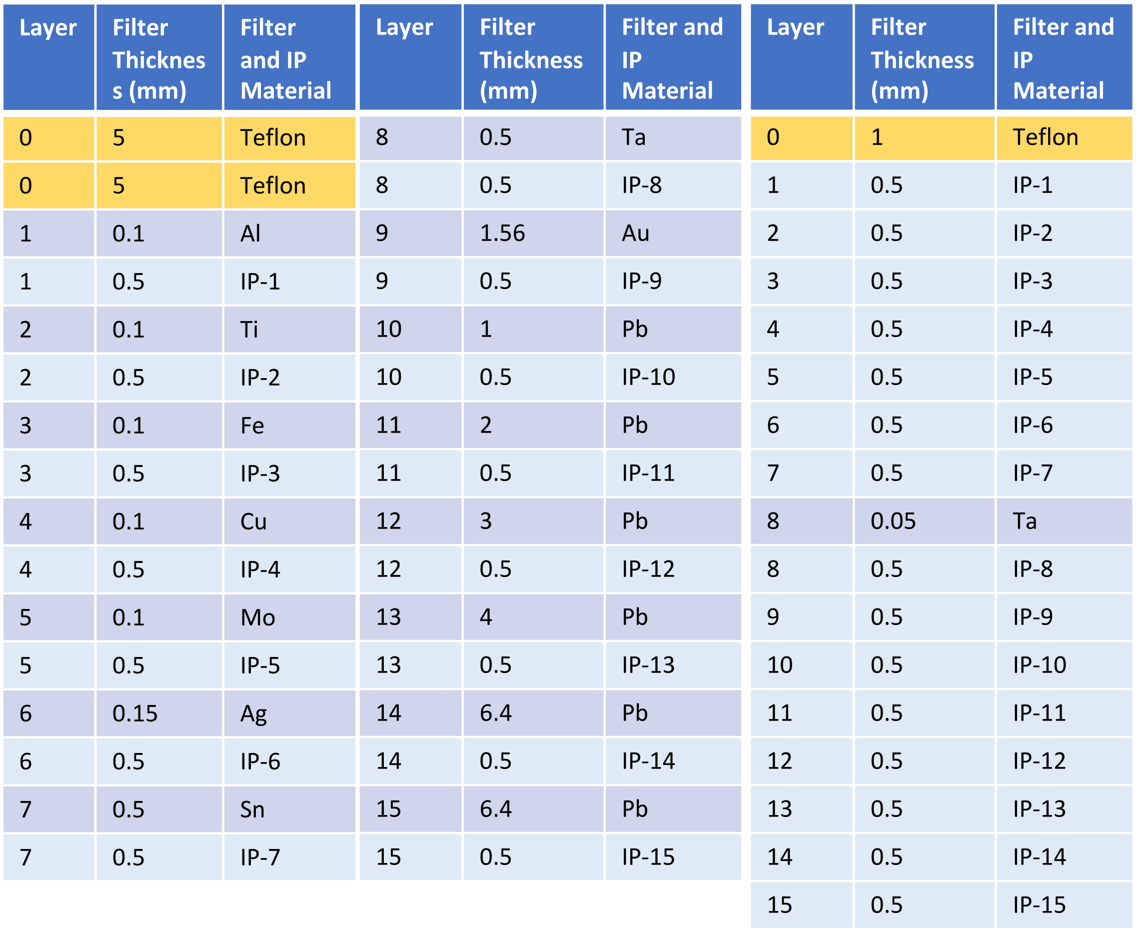

Layer	Filter Thickness (mm)	Filter and IP Material	Layer	Filter Thickness (mm)	Filter and IP Material	Layer	Filter Thickness (mm)	Filter and IP Material
0	5	Teflon	8	0.5	Ta	0	1	Teflon
0	5	Teflon	8	0.5	IP-8	1	0.5	IP-1
1	0.1	Al	9	1.56	Au	2	0.5	IP-2
1	0.5	IP-1	9	0.5	IP-9	3	0.5	IP-3
2	0.1	Ti	10	1	Pb	4	0.5	IP-4
2	0.5	IP-2	10	0.5	IP-10	5	0.5	IP-5
3	0.1	Fe	11	2	Pb	6	0.5	IP-6
3	0.5	IP-3	11	0.5	IP-11	7	0.5	IP-7
4	0.1	Cu	12	3	Pb	8	0.05	Ta
4	0.5	IP-4	12	0.5	IP-12	8	0.5	IP-8
5	0.1	Mo	13	4	Pb	9	0.5	IP-9
5	0.5	IP-5	13	0.5	IP-13	10	0.5	IP-10
6	0.15	Ag	14	6.4	Pb	11	0.5	IP-11
6	0.5	IP-6	14	0.5	IP-14	12	0.5	IP-12
7	0.5	Sn	15	6.4	Pb	13	0.5	IP-13
7	0.5	IP-7	15	0.5	IP-15	14	0.5	IP-14
						15	0.5	IP-15

Figure 3.3: Filter and image plate stacks in the BMXS cartridge. The left and middle columns are the high energy configuration which can resolve the x-ray spectrum up to 1 MeV. The right column is the low-energy configuration which is designed to resolve the x-rays up to 100 keV.

bins ranging from 1 keV to 100 MeV. The n^{th} simulation injects 2×10^6 x-ray photons with energies randomly distributed from $10^{5(n-1)/150}$ keV to $10^{5n/150}$ keV into the BMXS, then calculates the average deposited energy on the active layer. The simulated cannon response functions are benchmarked to experiments [69, 104]. In addition, the measured photo-stimulated luminescence, $\mathrm{PSL}_{\mathrm{raw}}$, is proportional to the energy deposited in the active layer as [69, 104, 105, 106, 107]

$$\mathrm{PSL}_{\mathrm{raw}} = f\,\mathrm{PSL}_{\mathrm{corr}} = f\,\alpha E_{\mathrm{dep}}, \tag{3.1}$$

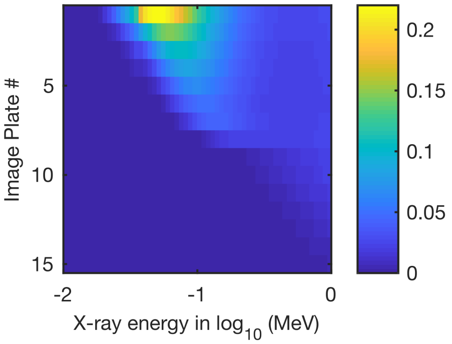

(a) MeV filter configuration with 3 mm glass in front of the cartridge.

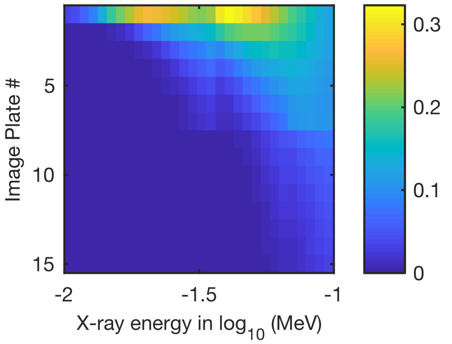

(b) Low-energy (<100 keV) filter configuration with 25 μm Al + 250 μm PET covering the cartridge front.

Figure 3.4: BMXS response functions of each image plate's active layer: photon-deposited energy in unit area density of the image plate's active layer, in units of $\mathrm{MeVg^{-1}cm^{2}ph^{-1}}$. The area density of the active layer in a BAS-MS image plate is 0.038 $\mathrm{g/cm^2}$.

in which for the Fuji BAS-MS image plate, $\alpha = 0.75 \pm 0.11$ PSL/MeV when the scan pixel size is 50 μm [107], and $\alpha = 0.54$ PSL/MeV when the pixel size is 100 μm, which is corrected by the resolution multiplier listed in Table IV of Ref. [106], and $f = 0.9$ is the fading factor for the BAS-MS image plate (scan delayed 45 min) [108]. In the experiments described in this dissertation, the scan pixel size for BMXS is always 100 μm. The scan sensitivity is S4000, and the latitude is L5. For the low-energy x-rays (<10 keV), a more complicated model is proposed in Ref. [107], which considers the transmission of the scanner and PSL photons. For > 20 keV x-rays, photons would deposit uniformly in the depth of the active layer. Therefore, Eq. 3.1 is a suitable model for BMXS [107].

3.3.2 Cu Kα radiation diagnostics

Besides the BMXS, this project has also used Cu Kα diagnostics—a spherical crystal imager (SCI) [109] and a zinc von Hamos spectrometer (ZVH) [110]—to quantify the hot electrons. After a hot electron knocks out one of the bound electrons in the inner shell (K-shell), a second-shell (L-shell) electron may fall into the K-shell, emitting a Cu Kα x-ray. The cross-section of the Kα emission has been characterized in Ref. [111]. In this experiment, the hot electrons would need to penetrate the CH layer before reaching the Cu layer. The 25 μm-thick 1 g/cm^3 CH would slow 40 keV electrons to ~10 keV [112], which suggests that only hot electrons with > 40 keV energy would induce the Cu K-shell emission.

Spherical crystal imager

To image Cu Kα x-rays, the SCI uses a quartz crystal, spherically bent, to reflect the x-rays. The spherical crystal has a curvature radius of 500 mm. The focal distance is half of the curvature radius. This crystal was cut along the 2131 (211) planes for a $2d$ spacing of 0.3082 nm, in which d is the lattice distance. The reflection order is 2 for the Cu Kα. The Bragg angle is 88.7°, which is close to the surface normal direction. This imager has a magnification of 9.63 on OMEGA EP and 14.7 in OMEGA-60 chamber. An image plate is used as the signal detector.

The crystal also reflects the continuous bremsstrahlung x-rays around the Cu Kα emission. Because of their wide bandwidth, these x-rays would spread and become the background signal. This background was fitted by a 3$^{\text{rd}}$-order 2D polynomial model and subtracted.

Zinc von Hamos spectrometer

The zinc von Hamos spectrometer (ZVH) uses a curved highly oriented pyrolytic graphite (HOPG) crystal placed in von Hamos geometry to resolve the x-ray spectrum around the Zinc Kα and Kβ x-rays. In these experiments, this diagnostic was inserted by 4 mm to center the Cu Kα and Kβ (~8.9 keV). The crystal reflectivities were calibrated for the Cu Kα and Kβ x-rays [110]. In this calibration, the ZVH used a Fuji BAS-MS image plate as the x-ray detector. This image plate was scanned with S4000 sensitivity, 50 μm resolution and L5 latitude. The same parameters were applied in the experiments described in this dissertation. To protect the crystal and control the signal level, blast shield and image plate filters covered the front of the ZVH and the image plate respectively. The data were processed in several steps to obtain the total Cu Kα yield from the measured spectrum: spectrum calibration, detector filtration correction, background subtraction, fitting Gaussian functions to the Cu Kα spike and finally target filtration correction, following Ref. [113]. The target filtration correction is performed because the 20 μm-thick Cu layer inside the target can block ~50% of the emitted Cu Kα, causing uncertainties when comparing the measured yields, especially for those experiments that have the ZVH detector placed in a different direction. Although the correction is also imprecise because the emission's distribution inside the Cu layer cannot be determined, by assuming the Cu layer emits the x-rays uniformly or from its front, this correction can give the upper and lower bounds of the total emission yield.

The ZVH-measured Cu Kα yield can also be compared with the yield calculated in ITS 3.0 simulations. When the simulation gives a synthetic bremsstrahlung spectrum fitting the BMXS measurement, it also calculates the Cu Kα emission which is compared with the ZVH measurement, as discussed in Sec. 5.4.2. The inconsistencies are not significantly above the uncertainties of the ZVH and BMXS (20%). In addition, the inconsistency can also be induced by the collective effect of the electron propagation. [114]

3.3.3 4ω probe diagnostic system

On OMEGA EP, a fourth-harmonic laser (10 ps, 10 mJ, $\lambda_\mathrm{p} = 263$ nm) was injected to probe the plasma with a suite of diagnostics [115] including angular filter refractometry (AFR) [116], shadowgraphy, polarimetry [117]. The probe laser can illuminate a ~4-mm diameter region at the target chamber center. The light passing through the plasma is collected by an $f/4$ telescope. The imaging system also has a bandpass filter which blocks wavelengths more than 2 nm away from 263 nm.

Angular filter refractometer

An angular filter refractometer (AFR) [116] is installed to capture the plasma perturbations induced by laser–plasma instabilities. The AFR has concentric rings placed on the Fourier plane of the 4ω probe measuring the map of the refraction angle of the 4ω probe after passing through the plasma. The refraction angle map can show the density perturbation is because the refraction index depends on the plasma density as discussed in Sec. 2.1

$$\eta = \left(1 - \frac{n_\mathrm{e}}{n_\mathrm{c}}\right)^{1/2}, \tag{3.2}$$

in which $n_\mathrm{c} = 1.6 \times 10^{22}\ \mathrm{cm}^{-3}$ is the critical density of the 4ω probe laser. The probe's phase front ($\phi(x, y)$ in radian) after passing through the plasma is

$$\phi(x, y) = \frac{\pi}{\lambda_\mathrm{p} n_\mathrm{c}} \int_{-\infty}^{\infty} n_\mathrm{e}(x, y, z)\mathrm{d}z, \tag{3.3}$$

assuming $n_\mathrm{e} \ll n_\mathrm{c}$, and z is the direction of the probe axis, $\lambda_\mathrm{p} = 263$ nm which is the probe's wavelength . The refraction angle of the probe (θ_p in radian) is proportional to the gradient of the phase as

$$\theta_\mathrm{p}(x, y) = \frac{\lambda_\mathrm{p}}{2\pi} |\nabla \phi(x, y)|. \tag{3.4}$$

To visualize the map of the refraction angle, the concentric rings placed on the Fourier plane can block certain bands of angles, creating shadows on the image plane. This filtered image shows the contour map of the probe's refraction angle. With a carefully designed filter, the AFR can measure a wide range of densities ($10^{19} - 10^{21}$ cm^{-3} on OMEGA EP).

Shadowgraphy and inversion

Shadowgraph images of the 4ω probe were also captured to diagnose the density perturbations induced by either laser–plasma instabilities or laser filamentation. The density depression inside the perturbation would act as a focusing lens, since the refractive index in the low-density region is higher than that in the high-density region. If the density depression is in front of the object plane, it focuses the probe, creating a high-intensity spot on the object plane; when the density depression is behind the object plane, effectively, it creates a lower-intensity spot on the object plane.

The quantitative analysis of the shadowgraphy image in laser–plasma experiments has been proposed in Ref. [118], using a linear deflection model. This model suggests that the intensity of the probe laser on the object plane $I(x,y)$ depends on the density profile of the plasma as [119]

$$\left(\frac{\partial^2}{\partial x^2}+\frac{\partial^2}{\partial y^2}\right)\int_0^{\Delta z}\ln\eta(x,y,z)\mathrm{d}z=\frac{1}{L}\frac{I(x,y)-I_0}{I_0}, \tag{3.5}$$

in which I_0 is the original intensity of the probe, and L is the distance between the plasma and the object plane. This linear model is appropriate if the deflection-induced light displacement on the object plane ($L\theta_\mathrm{p}$) is much smaller than the scale of the density perturbation.

If the displacement ($L\theta_\mathrm{p}$) is large, the deflection becomes nonlinear. Since the deflection angle $\boldsymbol{\theta}_\mathrm{p} = -\nabla \int \ln \eta(x_0, y_0, z_0)\mathrm{d}z_0$, the deflection potential can be defined as

$$\Phi(x_0, y_0) = -\int \ln \eta(x_0, y_0, z_0)\mathrm{d}z_0, \tag{3.6}$$

in which x_0, y_0, z_0 are coordinates in the plasma. The probe light passing through (x_0, y_0) would be deflected to (x, y) on the object plane, in which

$$x = x_0 + \theta_{\mathrm{p},x} L, \tag{3.7}$$

$$y = y_0 + \theta_{\mathrm{p},y} L. \tag{3.8}$$

The intensity on the object plane $I(x, y)$ becomes

$$I(x, y) = \frac{I_0(x, y)}{\left|\frac{\partial(x,y)}{\partial(x_0,y_0)}\right|} \tag{3.9}$$

where $\left|\frac{\partial(x,y)}{\partial(x_0,y_0)}\right|$ is the determinant of the Jacobian matrix of (x, y) respect to (x_0, y_0).

In the nonlinear regime where Eq. 3.5 is invalid, the reconstruction of $\Phi(x_0, y_0)$ can give the density profile by forward-fitting the simulated intensity map $I(x, y)$ to the measured shadowgraphy images. The reconstruction algorithm is described in Ref. [120]. The current version of this code is available online [121], which implements an improved computational algorithm as described [122]. The reconstructed deflection potential $\Phi(x, y)$ gives the amplitude and typical size of the density perturbations, as discussed in Ch. 6. However, in most of the laser–plasma interaction experiments, the object plane of the probe's imaging system was set on the center of the plasma. As a result, the distance between the perturbations and the object plane L is unknown. Since density perturbations far from the object plane would cause larger deflection displacements, dominating the intensity perturbation, L is assumed to be at its upper limit, which is the radius of the perturbation region (300 μm) in the dissertation's experiment.

3.4 Radiation–hydrodynamic code: FLASH

FLASH [123] is an open-source radiation–hydrodynamics code used in this project to simulate the laser heating and the plasma generation. FLASH was originally designed to simulate plasma hydrodynamics for astrophysics research; it has been improved to include the physics of laser energy deposition and light deflection in plasmas. Therefore, FLASH is capable of simulating the high-energy-density physics (HEDP) experiments conducted at multi-beam laser facilities such as OMEGA and NIF.

The simulations for this project were developed based on the LaserSlab unit, which simulates a laser irradiating a solid slab target. The plasmas generated by these nanosecond lasers are usually non-equilibrium: electrons, ions, and radiation have different temperatures. To simulate this non-equilibrium condition, the LaserSlab unit applies three-temperature (3T) hydrodynamics physics models, including radiation transportation, as well as the energy exchange between the electrons and ions. The radiation's emission, absorption, and transmission are calculated based on the multigroup opacity tables generated from PROPACEOS [124], in which the radiation energy was logarithmically spaced over 6 groups from 0.1 eV to 100 keV. The equation of states of the plasma is also interpolated from the PROPACEOS EOS tables. The plasma formation was simulated in 2D cylindrical ($r-z$) coordinates, assuming that the plasma is symmetric in the azimuthal direction. The laser ray-tracing and the inverse-bremsstrahlung absorption are calculated in 3D Cartesian coordinates. Then, the deposited energy is projected onto the 2D $r-z$ coordinates.

3.4.1 Benchmark

The simulated plasma profiles agree with the experimentally measured profiles, as described in Ch. 5. FLASH has also been benchmarked with the thermal conduction experiments performed at the Nova laser facility [125]. This experiment used eight beams (four beams on each side) to irradiate a 1.5 μm Ti foil. The four beams on each side delivered 11 ± 0.5 kJ energy in a 2 ns flat-top pulse. The lasers were focused 3800 μm above the target surface without phase plates. The lasers penetrated the target, creating a x-ray ring on the target surface expanding outward. X-ray cameras captured the radius changing with time. To benchmark FLASH, we simulated the laser beams irradiating the 1.5 μm Ti foil with 750 μm diameter spots (8th order super-Gaussian shape) and the same incident angles as the experiment (50°off the target normal). The overlapped spot diameter on the target surface is about 1100 μm. Flux limiter ($f = 0.06$) is used in the simulation, same as that in other simulations for this dissertation. The x-ray emission ring (bright spot at $r = 570$ μm) is shown in Fig. 3.5, which is the map of the $n_\mathrm{e}^2 T_\mathrm{e}$, since x-ray brightness is proportional to $n_\mathrm{e}^2 T_\mathrm{e}^\alpha$, in which α was chosen to be 1.0 in this benchmark. The ring position versus time is plotted in Fig. 3.6, which agrees well with the experimental results (blue points).

3.4.2 Limitations

Despite the agreement between the simulations and the experiments, the simulations still produces discrepancies from the experiments because of the $r-z$ coordinates and the lack of the laser–plasma interaction physics. First, the cylindrical symmetry in simulations is inconsistent with the experiment. In the experiments, the one or two laser beams were heating the plasma in different directions. However, in the 2D $r-z$ simulations, a ring of laser beams above the target are heating the target because of the

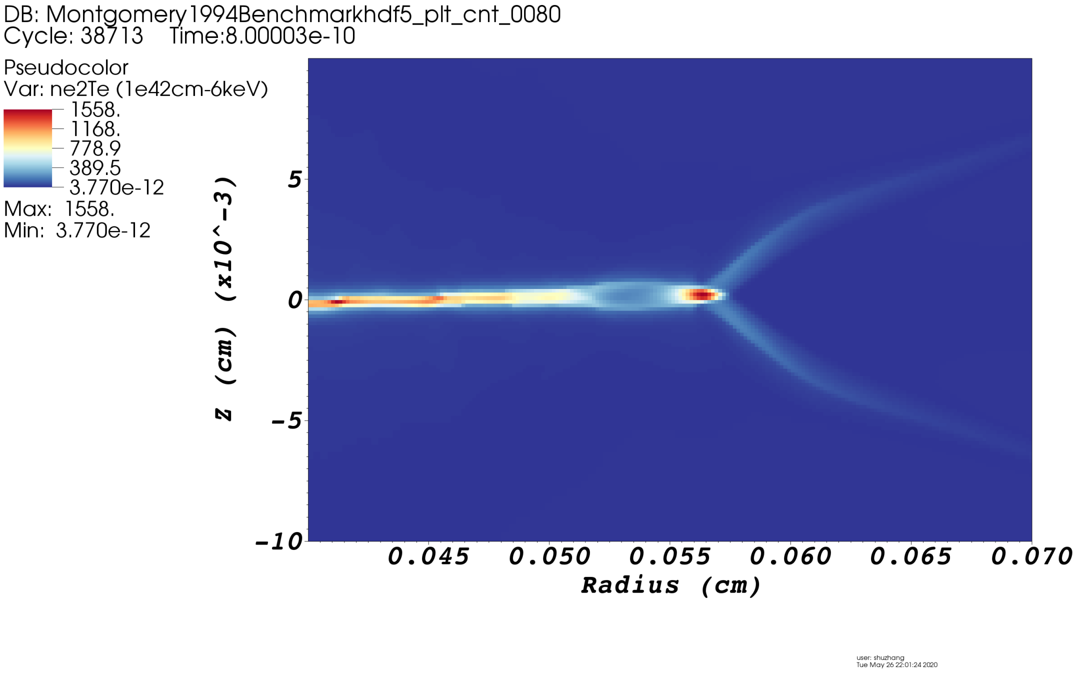

Figure 3.5: x-ray emission ($n_e^2 T_e$) map for the benchmark simulation at 800 ps. The ring emission is the bright dot at $r = 0.057$ cm

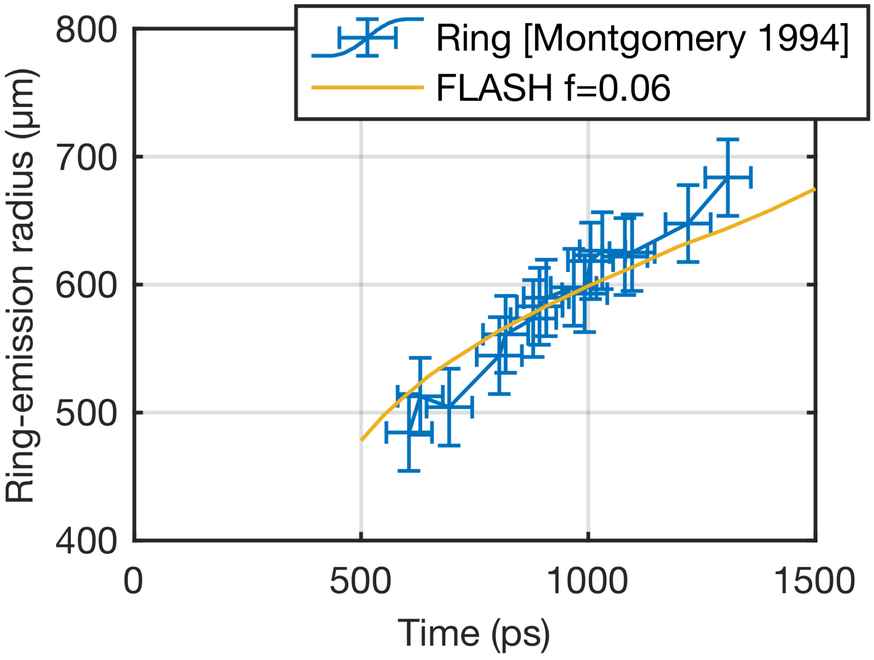

Figure 3.6: Ring radius versus time. Blue points are the measured ring positions from Ref. [125], the yellow line is the ring position versus time in the FLASH simulation.

3D-in-2D ray-tracing model, which enlarges the spot size and reduces the laser intensity on the target surface by $1-\cos(23°)=8\%$. The enlarged spot size would also enlarge the length-scale of the plasma. Second, the laser–plasma interaction model in FLASH considers only the inverse-bremsstrahlung absorption, without any laser–plasma instability (LPI) model. The lack of LPI physics limits the accuracy of simulating the experiments with $I_{\mathrm{L}} > 10^{15}$ W/cm^2 lasers, in which LPIs are strong. However, this discrepancy can be used to infer the role of LPIs. The analyses are presented in Ch. 4.

3.5 Monte Carlo code: GEANT4

GEANT4 is an open-source simulation toolkit that has been used to simulate the target response functions in this project, which describes the x-ray emissions due to a hot electron hitting the target. Since most of the hot electrons' energies are <10 MeV, and atomic de-excitation and its induced x-ray fluorescence are important in this electron energy range, the low-energy electromagnetic physics models in GEANT4, such as the Livermore physics model or the Penelope model, are suitable to be applied. For this project, the *G4EmLivermorePhysics* physics list constructor was chosen, and the atomic deexcitation processes are turned on, which includes fluorescence, Auger electrons, and particle-induced x-ray emission. The x-ray absorption is also simulated self-consistently.

The target response function simulation was modified from the x-ray fluorescence simulation unit provided as one of the advanced examples in GEANT4, version 10.03. A total of 81 simulations were conducted to cover the 10 keV–100 MeV energy range. Each simulation injects 10^8 hot electrons with energy

$$E_{\mathrm{HE},i} = 10^{1+\frac{i-1}{20}}\ \mathrm{keV}. \tag{3.10}$$

The simulations record the energies and the directions of the electrons and the photons that escape from the target. The recorded x-rays are binned into 150 energy groups and 36 angular groups. The x-ray energy bins have logarithmically spaced edges from 1 keV to 100 MeV. The angle bins are spaced linearly from 0° to 180° off the electron direction. Thus, the dependence of the x-ray emission on the hot electron energy can be summarized as a target response matrix (TRM) with $81\times150\times36$ elements. For a BMXS cannon located at θ angle off the laser direction, the vector of the synthetic PSL ($\mathrm{PSL}_{\mathrm{syn}}$, 1×15) becomes

$$\mathrm{PSL}_{\mathrm{syn}} = f_{\mathrm{HE}} \times \mathrm{TRM}_{\theta} \times \mathrm{CRM}, \tag{3.11}$$

in which f_{HE} is the electron spectrum binned as a 1×81 vector, TRM_{θ} is an 81×150 matrix chosen from TRM based on the BMXS's line-of-site, and CRM is the 150×15 cannon response matrix as discussed in Sec. 3.3.1. Fitting $\mathrm{PSL}_{\mathrm{syn}}$ to the measured PSL by tuning f_{HE} can give the hot electron's temperature and energy. The analyses are detailed in Sec. 5.4.1.

Chapter 4

Pump-Depletion Dynamics and Saturation of Stimulated Brillouin Scattering in Shock Ignition Relevant Experiments

4.1 Introduction

As discussed in Ch. 1 and Ch. 2, the laser–shock energy coupling in shock ignition remains uncertain, since the spike pulse may lose energy because of laser–plasma instabilities (LPIs), such as stimulated Raman scattering (SRS), stimulated Brillouin scattering (SBS), and two-plasmon decay (TPD). This chapter reports on a series of experiments to study the laser propagation and LPI physics with SI-relevant high intensity (~10^{16} W/cm^2) in large-scale (L_n ~ 260–330 μm) keV plasmas, an unexplored regime. The blast wave profile suggests that a strong laser pump-depletion starts at the low-density (n_e ~ $0.02 n_\mathrm{c}$) plasma and progresses into the higher density ($n_\mathrm{e} > 0.1 n_\mathrm{c}$) region in 0.5 ns.

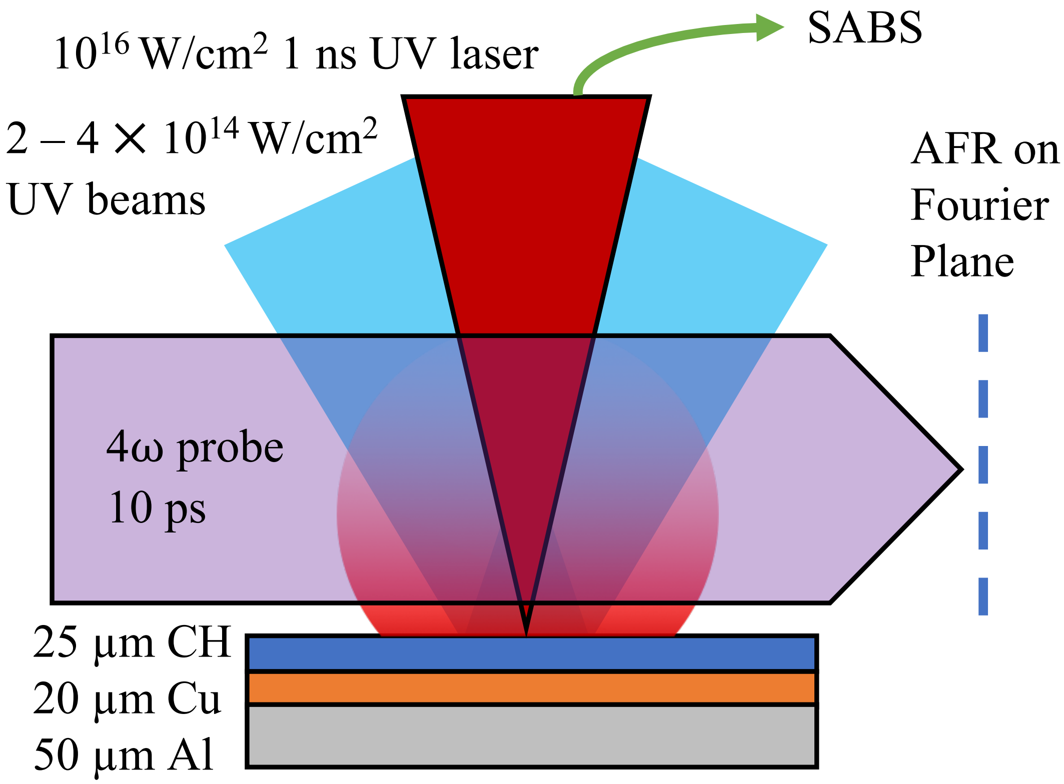

Figure 4.1: The experimental setup. One-two 2 kJ 2 ns UV lasers (blue) irradiated the disk target to generate the plasma (light red). One tight focused 1.25 kJ UV laser (red triangle) was injected to interact with the plasma. A 4ω laser (purple) probed the plasma immediately after the laser–plasma interaction.

Such ns-scale pump-depletion dynamics can be explained by the local SBS saturation induced by the breaking of the ion-acoustic wave (IAW). This SBS saturation help resolve the long-standing discrepancy on the reflectivity data between PIC simulations [33, 34, 35] and previous experiments [46, 56, 63, 64, 65, 40, 67]. These findings have significant implications for future SI experiments with megajoule-class laser facilities and other high energy density experiments where IAWs with high amplitudes may occur.

4.2 Experimental setup

The experiments were performed on the OMEGA EP laser facility [68] at the Laboratory for Laser Energetics, Rochester, US. To produce a shock ignition relevant plasma, one or two 2 kJ, 2 ns UV lasers irradiated a 3-layer disk target (25 μm CH/20 μm Cu/50 μm Al) acting as a hot electron collector [126, 127], as shown in Fig. 4.1. These 2-ns lasers were smoothed by 750 μm 8th-order super-Gaussian distributed phase plates. Delayed by 1.0–1.5 ns relative to the 2-ns beam onset, a 10^{16} W/cm^2 (1 ns, 1.25 kJ) UV pulse was then injected into the plasma along the target normal direction. The beam was focused on the target surface with a ~80 μm diameter spot without a phase plate, which may maximize the hot electron generation. It created a conical blast wave expanding radially from the laser axis. Immediately after the interaction pulse, the blast wave was captured on the refraction map of a 4ω probe laser ($\lambda = 263$ nm, 10 ps) by an Angular Filter Refractometer (AFR) [116]. The streaked Sub-Aperture Backscattering Spectrometer (SABS) temporally resolved the spectrum of the backward SRS (430–750 nm). The blast wave and the SRS spectrum evolution have shown similar pump-depletion features in all of our 6 large-scale experiments. We also used the radiation-hydrodynamic code FLASH [123, 128] to simulate the plasma formation and the blast wave generation. FLASH has no LPI physics but can simulate the laser focusing, refraction, and collisional absorption. The simulated plasma formation has been benchmarked [126, 129] and the thermal transportation in FLASH is also benchmarked to a NOVA experiment [125].

4.3 Plasma profiles

We have used 2D $R-z$ FLASH to simulate the plasma generation driven by the low-intensity UV lasers. The plasmas' density and temperature profiles along the laser axis are shown in Fig. 4.2. The plasma generated by the 2 kJ UV laser has $L_n \sim 330$ μm

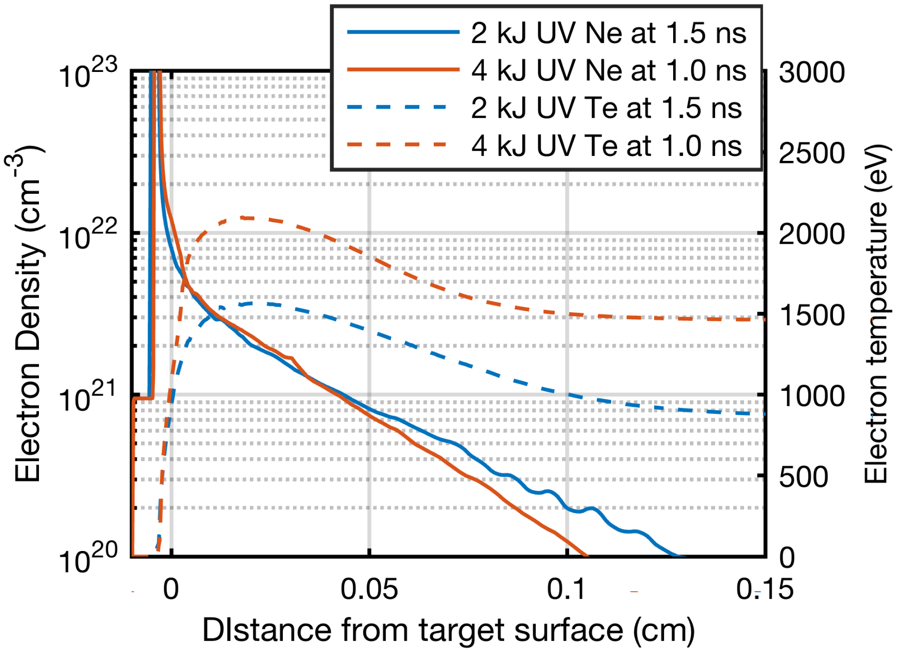

Figure 4.2: Simulated plasma density and temperature profiles along the target normal axis before the start of the interaction laser.

and $T_e \sim 1.5$ keV) at 1.5 ns; the plasma generated by the 4 kJ UV lasers has a higher temperature (2.0 keV) and a shorter scale length (260 μm) at 1.0 ns. The profiles are similar to that described in Ch. 5. The length scales and the temperatures were given by the profiles in the $n_c/10 - n_c/4$ ($0.9 \times 10^{21} - 2.25 \times 10^{21}\text{cm}^{-3}$) region. The 1.0 ns (or 1.5 ns) was the timing for the high-intensity interaction laser relative to the start of the plasma creation beam(s).

4.4 Blast wave

4.4.1 AFR measurement

The shapes of the blast waves, shown as the red dashed lines in AFR images (Fig. 4.3), indicate that the high-intensity laser is strongly pump-depleted. The experimental blast wave was captured in the AFR image, Fig. 4.3(a), at the end of the inter-

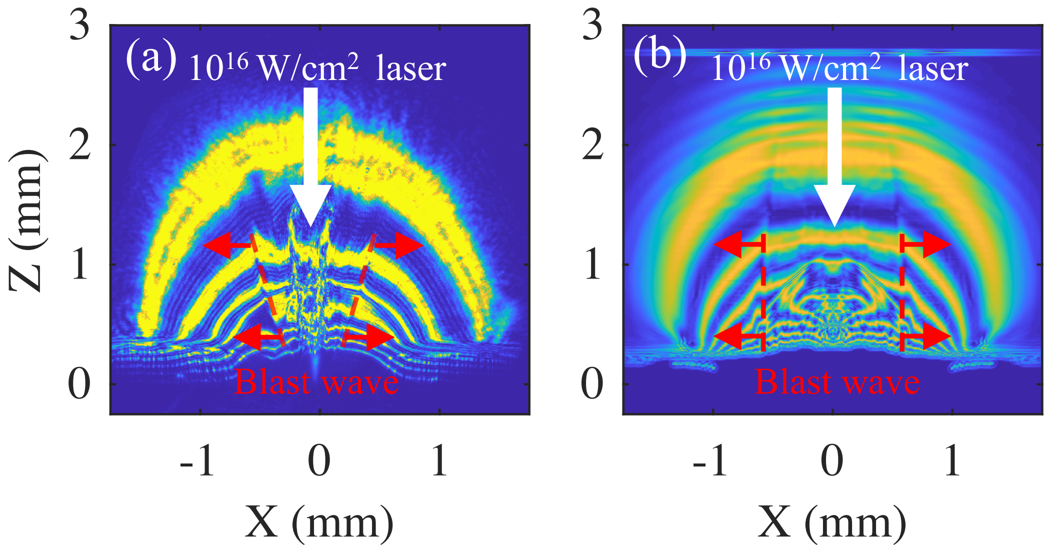

Figure 4.3: (a) The experimental AFR image; (b) the FLASH simulated AFR image. The target surface is at $z = 0$. White arrows show the directions of the high-intensity UV interaction lasers. The red dashed lines and arrows mark the blast wave fronts and their moving directions.

action laser. This high-intensity laser was delayed by 1.5 ns relative to the start of the 2 kJ 2-ns beam. At the start of the interaction pulse, the plasma has $T_e \sim 1.5$ keV and exponential density length scale $L_n \sim 330$ μm in the $n_c/10$–$n_c/4$ region. Experimentally, the high-intensity laser generated a conical blast wave as shown in Fig. 4.3(a). The blast wave diameter at the laser entrance, $\phi = 960 \pm 60$ μm at $z = 1.2$ mm ($n_e \sim 0.02 n_c$), is 90% larger than the diameter $\phi = 500 \pm 60$ μm at $z = 0.4$ mm ($n_e \sim 0.1 n_c$).

4.4.2 FLASH simulations

Instead of the conical-shaped blast wave in the experiment, 2D FLASH simulation shows a cylindrical blast wave in the synthetic AFR image in Fig. 4.3(b). The simulation has the same $f/6.5$ focusing laser corresponding to the experiments but did not include any LPI physics. These blast waves have similar diameters at the laser entrance ($z = 1.2$ mm) (1.14 mm versus 0.96 mm). However, at $z = 1.0$ to 0.4 mm, the experimental blast wave has 20–60% smaller diameters than the one in the simulation.

This smaller blast wave at $z < 1.2$ mm can be due to the LPI-induced pump depletion. According to Sedov's self-similar model for a cylindrical blast wave [130], the blast wave radius $r \propto t^{1/2}(E/\rho)^{1/4}$, where t is the time after the explosion, E is the absorbed laser energy per axial length and ρ is the medium density. Thus, the smaller blast wave at $z = 0.4$–1.0 mm can either be due to a strongly inhibited laser absorption or a shortened interaction time. However, the Sedov model's scenario may be unsuitable for this experiment, in which the blast wave is driven by a continuous laser in a high pressure, inhomogeneous plasma. We would need simulations to understand the conical shape in the experiment.

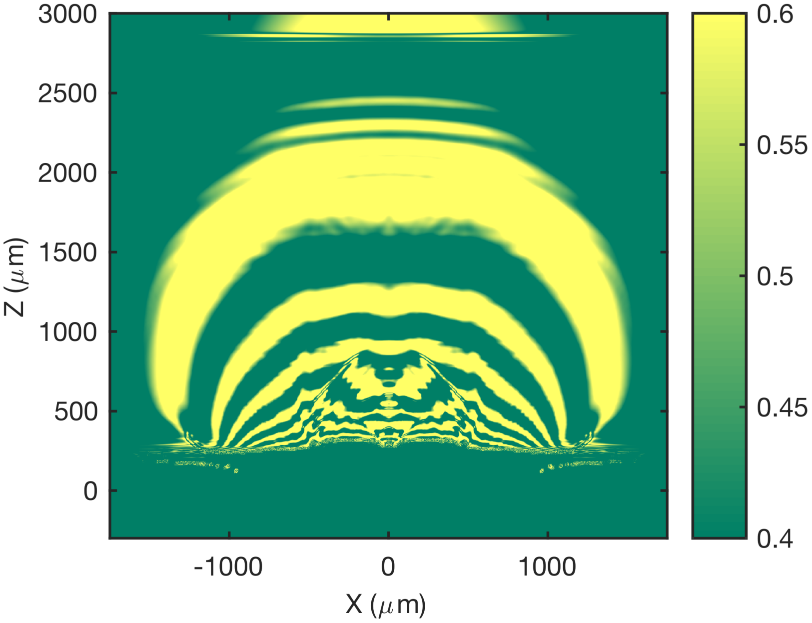

Figure 4.4: Synthetic AFR image for the simulation that has 50% power-reduced laser

To verify the dependence of the blast wave on the laser power, we preformed a 2D FLASH simulations with a power reduced (50% of the original power) high-intensity laser beam. The blast wave is still in a conical shape and has a diameter $\phi = 1.10$ mm at $z = 1.0$ mm, and $\phi = 1.04$ mm at $z = 0.5$ mm as shown in the synthetic AFR image

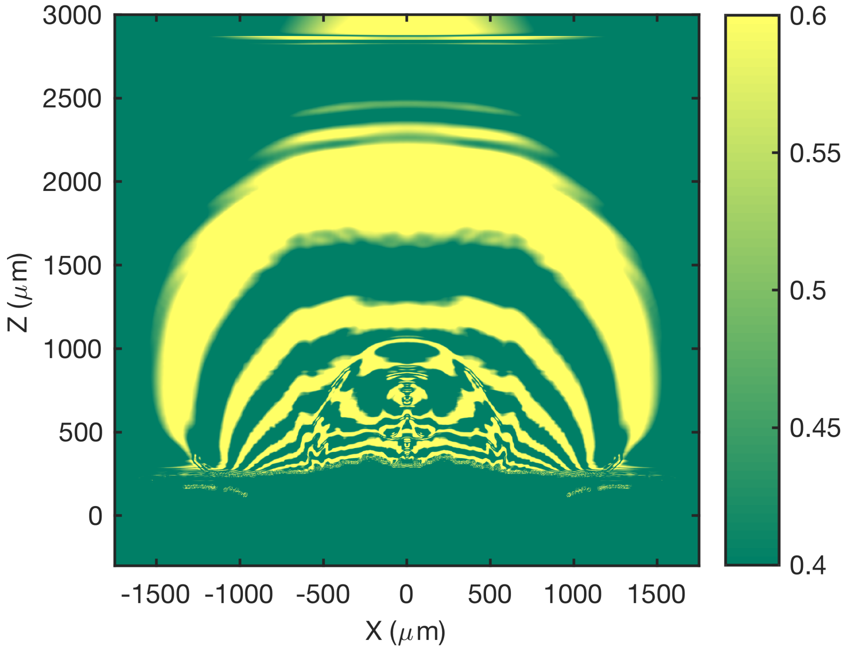

Figure 4.5: Synthetic AFR image for the simulation that has an f/3 focusing laser, mimicking the effect of self-focusing.

Fig. 4.4, similar to that in Fig. 4.3(b). Besides the laser power, since the laser may self-focus because of its ponderomotive force, we also performed a FLASH simulation with an $f/3$ laser to verify the dependence of the blast wave shape on the laser focusing. As shown in Fig. 4.5, the $f/3$ laser still drives a conical blast wave.

Blast wave model

To understand the cause of the conical blast wave, we performed 1D cylindrical FLASH simulations to rebuild the blast wave model.

In these 1D blast wave simulations, we scanned the laser power P_{L} and the laser duration respectively. Variation of the laser power is equivalent to variation of the absorption energy. The 1D simulation is an extracted thin layer at $z = 0.5$ mm of the 2D simulation at 1.5 ns adding reflective top and bottom boundaries. The laser has a

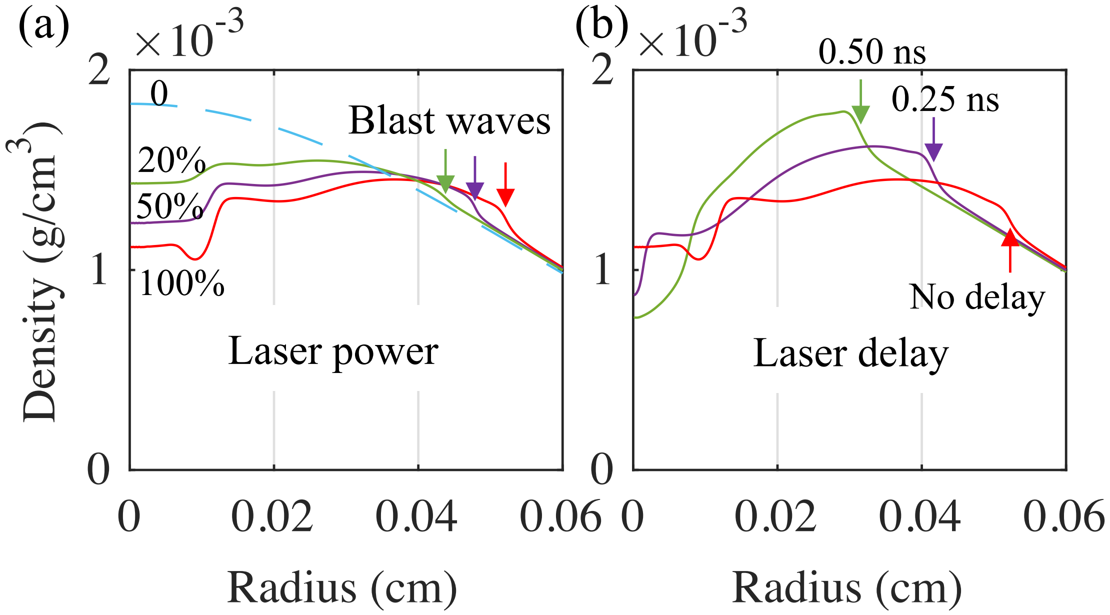

Figure 4.6: The simulated density profiles after the laser interaction (a) with different laser power, and (b) with different laser delays. The arrows mark the fronts of the blast wave.

200 μm diameter spot on this layer and the laser absorption is still calculated by inverse-bremsstrahlung. The density profile after the laser interaction is shown in Fig. 4.6(a) (for varying laser power) and Fig. 4.6(b) (for varying pump-depletion time). The radial positions of the blast waves are at the locations of the steep density gradients, marked by arrows. As shown in Fig. 4.6(a), the laser power weakly affects the position of the blast wave. When the laser power is reduced to 20% of the original, the blast wave's radial position only decreases by 18% to 430 ± 10 μm (green line), which is still 50% larger than the experimental radius at $z = 0.5$ mm ($r = 290 \pm 30$ μm). Further reducing the laser power to 5% would flatten the wave front to unobservable (profile not shown). No reduced laser power can reproduce the small and clear blast wave found in the experiment; however, a delayed laser onset can. As shown in Fig. 4.6(b), when the first 0.25 ns (purple line) or 0.50 ns (green) of the laser is fully pump-depleted—the remaining 0.75 ns or 0.50 ns pulse has the original power—the radius decreases linearly from 520 ± 10 μm (r_0) to 420 ± 10 μm

or 320 ± 10 μm, respectively. The relative change of the blast wave radius $(r_0 - r)/r_0$ is proportional to the pump-depletion time (t_{PD}) as

$$\frac{r_0 - r}{r_0} = \frac{t_{\mathrm{PD}}}{1.3\ \mathrm{ns}}. \tag{4.1}$$

This model is also validated by the 1D simulations at $z = 1.0$ mm. These simulations also show the model is insensitive to the laser spot size. Figure 4.7(a) are the plasma profiles in the simulations that have a 200 μm diameter laser spot (same spot size as the simulation at $z = 0.5$ mm); fig. 4.7(b) shows the simulations with a 300 μm spot (considering a larger spot at $z = 1.0$ mm due to the laser focusing geometry). Despite the changing of z and laser spot size, the relative change of the blast wave radius is still proportional to laser delay time as

$$\frac{r_0 - r}{r_0} = \frac{t_{\mathrm{PD}}}{1.25\ \mathrm{ns}} \tag{4.2}$$

in the 200 μm spot simulations and

$$\frac{r_0 - r}{r_0} = \frac{t_{\mathrm{PD}}}{1.31\ \mathrm{ns}} \tag{4.3}$$

in the 300 μm spot simulations. Both results agree well with Eq. 4.1 given by the $z =$ 0.5 mm simulations. This consistency also shows that although the spot size can affect the intensity and the blast wave size, it would not impact the relative change of the blast wave radius. Thus, Eq. 4.1 is valid despite that the density and the spot diameter are changing along the laser axis.

The weak energy-dependence and the linear time-dependence suggest that the LPI-induced pump-depletion blocks the first hundreds of picoseconds of the high-intensity laser. Then the pump-depletion is mitigated and the laser intensity returns to the order of the original and generate a smaller blast wave due to the delayed onset. Meanwhile,

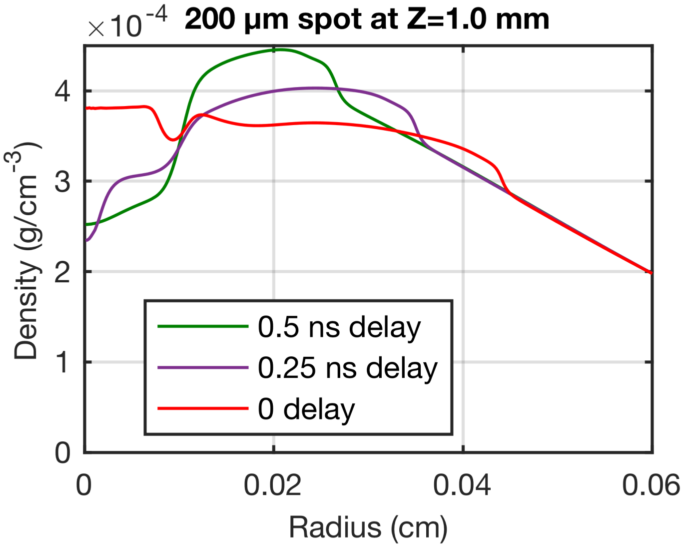

(a) The spot size is 200 µm, same as the spot size of the $z = 0.5$ simulations.

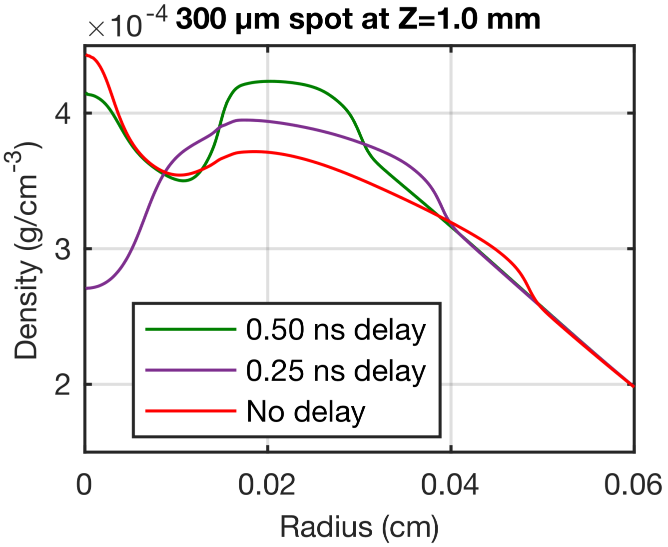

(b) The spot size is 300 µm.

Figure 4.7: 1D FLASH blast wave simulations with varied laser delays and spot sizes at $z = 1.0$ mm.

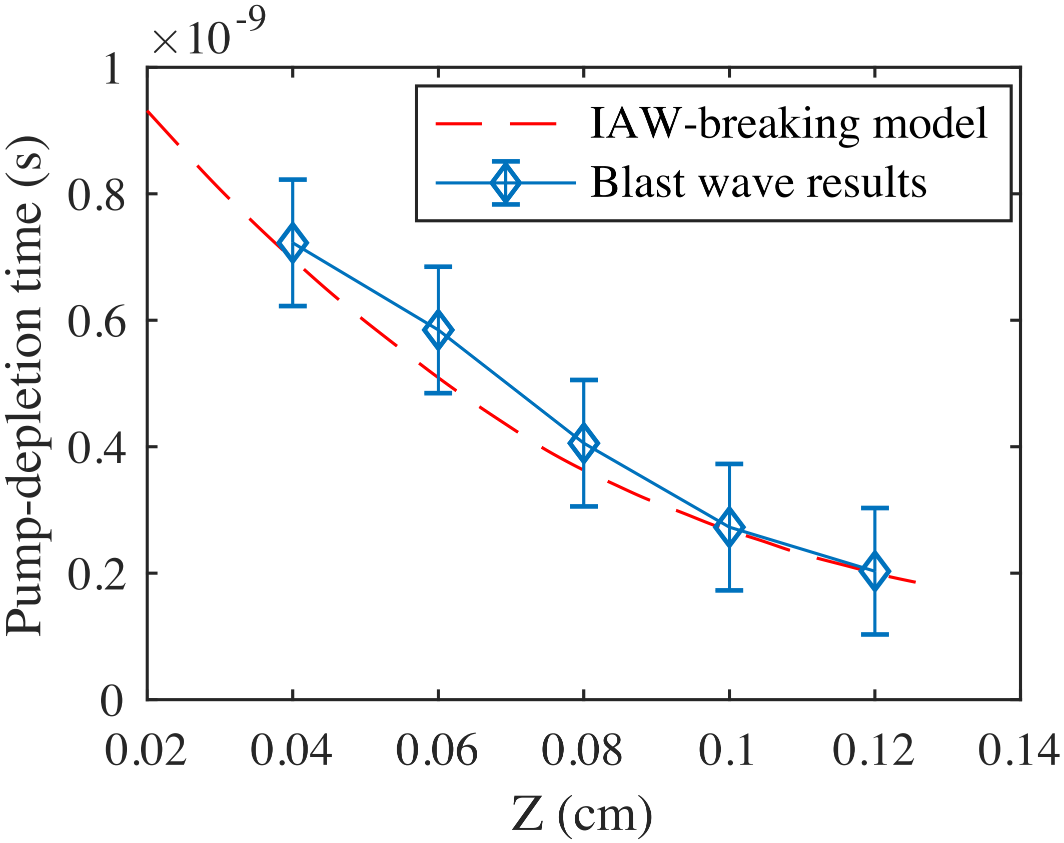

Figure 4.8: The pump-depletion times (t_{PD}'s) at different distances above the target (Z). Blue diamonds are the experimental t_{PD}'s from the blast wave analyses. The red dashed line is the t_{PD} predicted by the IAW breaking model.

the pump-depletion region moves inward, so the laser is slowly penetrating the plasma.

4.5 Time-dependent pump depletion

With the time-dependent blast wave model Eq. (4.1), we can calculate the pump-depletion time t_{PD} along the laser axis using the ratio of experimental radius to 2D FLASH simulated radius as $t_{\mathrm{PD}}(z) = (1 - r_{\mathrm{exp}}(z)/r_{\mathrm{sim}}(z)) \times 1.3$ ns. As shown in Fig. 4.8, from $z = 1.2$ mm to 0.4 mm, the pump-depletion time t_{PD} increases by 0.5 ns indicating the pump-depletion region is moving inward with a speed of 0.5% c (v_{PD}). This speed agrees with an IAW-breaking SBS saturation model shown as the red dashed line, which

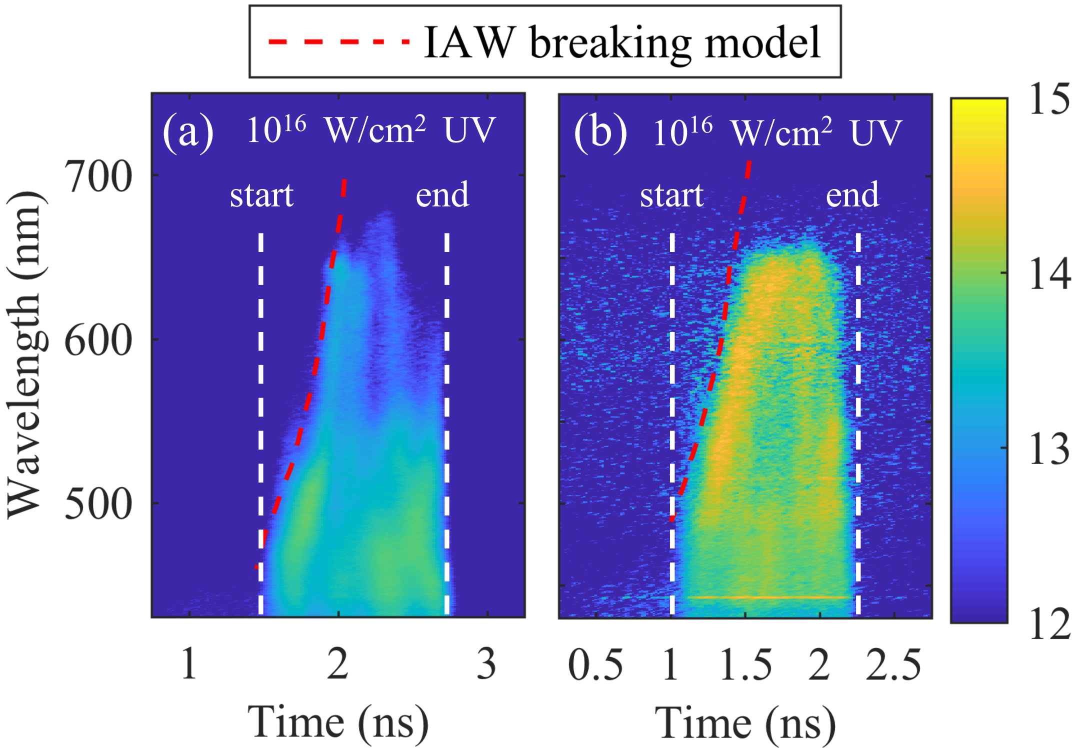

Figure 4.9: Streaked SRS spectra from two experiments in different plasma conditions. (a) Same laser and plasma conditions to the blast wave shot ($L_n \sim 330$ µm, $T_e \sim 1.5$ keV); (b) The plasma has higher temperature (2.0 keV) and shorter scale length (260 µm), and the interaction beam is delayed by 1.0 ns. Time=0 is the start of the low-intensity UV lasers. The color scale is in $\log_{10}$. Red dashed lines are pump-depletion positions predicted by the IAW breaking model.

is discussed later in this chapter.

4.6 Time-resolved spectrum of stimulated Raman scattering

Consistent with the blast waves, the time-resolved SRS spectra also show strong pump-depletion and a slow laser penetration in the 0.02–0.2 n_c plasma. Fig. 4.9 shows two SRS spectra from experiments in different plasma conditions. The experiment in Fig. 4.9(a) is under the same conditions as the blast wave experiment shown above ($L_n \sim$

330 μm, $T_{\mathrm{e}} \sim 1.5$ keV). The SRS signal from $n_{\mathrm{e}} < 0.02\ n_{\mathrm{c}}$ low-density region ($\lambda \sim 450$ nm) starts with the high-intensity UV laser. Then the SRS signal from the deeper region (0.02–0.20 n_{c}) gradually shortens. The experiment in Fig. 4.9(b) has a plasma with smaller $L_n \sim 260$ μm and higher $T_{\mathrm{e}} \sim 2.0$ keV generated by two 2-ns beams. The high-intensity laser is delayed by 1.0 ns. Similar to Fig. 4.9(a), the backscattered SRS starts at the short wavelength region (<500 nm corresponding to $n_{\mathrm{e}} < 0.06\ n_{\mathrm{c}}$). The onset of 500–650 nm SRS (0.06–0.20 n_{c}) is delayed by up to 0.5 ns. During the first 0.5 ns, the absence of SRS in the high-density region is contrary to the trend of the SRS convective gain, which increases slightly with the density in this plasma [131]. This discrepancy indicates that the first 0.5 ns of the laser pulse is depleted in the low-density region, which agrees with the pump-depletion evolution observed in the blast wave.

4.7 Ion-acoustic-wave-breaking SBS saturation model

The inward movement of the pump-depletion region can be explained by the IAW-breaking in SBS. An IAW would break when the ion quiver velocity (v_{quiver}) is close to the wave's phase velocity (c_{s}), as $v_{\mathrm{quiver}} \approx c_{\mathrm{s}}$ [132, 133]. Two IAW modes can grow in a CH plasma: a fast mode dominated by H^{+} ions and a slow mode dominated by C^{6+} ions. The phase velocities of each mode (c_{fast} and c_{slow}) are calculated by the kinetic model, expressed as Eq. (20) in Ref. [85], with $T_{\mathrm{e}}(z)$, $T_{\mathrm{i}}(z)$, and $n_{\mathrm{e}}(z)$ from the corresponding FLASH simulations. Under our conditions, $c_{\mathrm{fast}} \sim 1.1\sqrt{T_{\mathrm{e}}/m_{\mathrm{H}}}$ and $c_{\mathrm{slow}} \sim (0.6\text{–}0.8)\sqrt{T_{\mathrm{e}}/m_{\mathrm{H}}}$. v_{quiver} can be calculated from the energy of the IAW (E_{IAW}) since half of E_{IAW} is the ion kinetic energy and the other half is the potential energy. In strong SBS where the laser is fully scattered, IAW would constantly gain energy based on its wave frequency as,

$$\frac{\mathrm{d}E_{\mathrm{IAW}}}{\mathrm{d}t} = \frac{\omega_{\mathrm{cs}}}{\omega_0} P_{\mathrm{L}}, \tag{4.4}$$

where ω_{cs} and ω_0 are the angular frequencies of IAW and the laser, respectively, and P_{L} is the laser power. When the light is backscattered, the IAW's wave number k_{IAW} would approximately equal to $2k_{\mathrm{L}}$ to match the momentum conservation [18], so $\omega_{\mathrm{cs}}/\omega_0 \approx 2c_{\mathrm{s}}/c$. Accordingly, each IAW mode would reach the breaking condition in a small volume $S_{\mathrm{L}}\Delta z$ when

$$\frac{c_{\mathrm{fast}}}{c}P_{\mathrm{L}}\Delta t \approx \frac{1}{2}N_{\mathrm{H}}m_{\mathrm{H}}c_{\mathrm{fast}}^2 \tag{4.5}$$

for the fast mode, and

$$\frac{c_{\mathrm{slow}}}{c}P_{\mathrm{L}}\Delta t \approx \frac{1}{2}N_{\mathrm{C}}m_{\mathrm{C}}c_{\mathrm{slow}}^2 \tag{4.6}$$

for the slow mode, where N_{H} and N_{C} are the numbers of H^+ and C^{6+} ions in volume $S_{\mathrm{L}}\Delta z$, so $N_{\mathrm{H}} = N_{\mathrm{C}} = n_{\mathrm{e}}S_{\mathrm{L}}\Delta z/7$. Here a square pulse with a constant power P_{L} is assumed, and Δt is each SBS's growing time in this volume and S_{L} is the laser cross-section at position z. When both modes grow simultaneously following Eq. (4.4), they would share the laser power P_{L}. However, the slow mode would saturate ~8 times slower than the fast mode because of the large mass of the C^{6+} ion, so we only considered the slow mode when calculating the SBS saturation. After all C^{6+} ions in this volume are accelerated to the IAW phase velocity, SBS would stop amplifying the IAW and stop reflecting, so the laser can propagate into the next region. The pump-depletion front would move inward with speed v_{PD} expressed as

$$v_{\mathrm{PD}}(z) = \frac{\Delta z}{\Delta t} \approx \frac{14P_{\mathrm{L}}}{c_{\mathrm{slow}}(z)n_{\mathrm{e}}(z)S_{\mathrm{L}}(z)\,c\,m_{\mathrm{C}}}. \tag{4.7}$$

This model can predict the moving positions of the pump-depletion, shown as the red dashed lines in Fig. 4.8 and 4.9. The laser cross section $S_{\mathrm{L}}(z) = \pi(z/6.5 + 80\ \mu\mathrm{m})^2/4$ representing an $f/6.5$ focusing laser with an 80 μm focal spot at $z = 0$. Although the plasma conditions and the measurement methods are different, the predicted pump-depletion positions in the 0.02–0.20 n_c region agree well with all three experimental results.

4.8 Discussion

4.8.1 Other mechanisms for the conical blast wave

Although mechanisms other than pump-depletion may exist and affect the blast wave generation in these experiments, such as self-focusing and the inhibition of inverse-bremsstrahlung absorption due to the non-Maxwellian distributions, they cannot generate the conical blast wave. Self-focusing is weak in this experiment since the shape of the laser-induced channel agrees with the theoretical shape of the $f/6.5$ focusing laser. In a 2D FLASH test simulation, an $f/3$ laser also produced a cylindrical blast wave, as shown in Fig. 4.5, which suggests that the shape of the blast wave is insensitive to the focusing. In addition, the inverse-bremsstrahlung in the $n_e < 0.2n_c$ can only absorb <20% of the laser power. The absorption may be inhibited by a non-Maxwellian distribution; however, this inhibition is equivalent to reducing the laser power, which cannot generate the conical blast wave as shown in Fig. 4.6(a). Filamentation and self-focusing may increase the local intensity and reduce the absorption; however, this intensity increase will enhance SRS, which is against the delayed SRS in the $n_e > 0.05n_c$ region as discussed.

4.8.2 Density depression

Besides the blast waves, the high-intensity laser also generated a low-density channel with perturbations inside and a narrow and high-density wall around, as shown in Fig. 4.3(a). FLASH simulations have also shown density depression near the laser axis, as shown in Fig. 4.10. However, the narrow and high density wall is only observable experimentally, which may indicate a collective heating as suggested in PIC simulations [33].

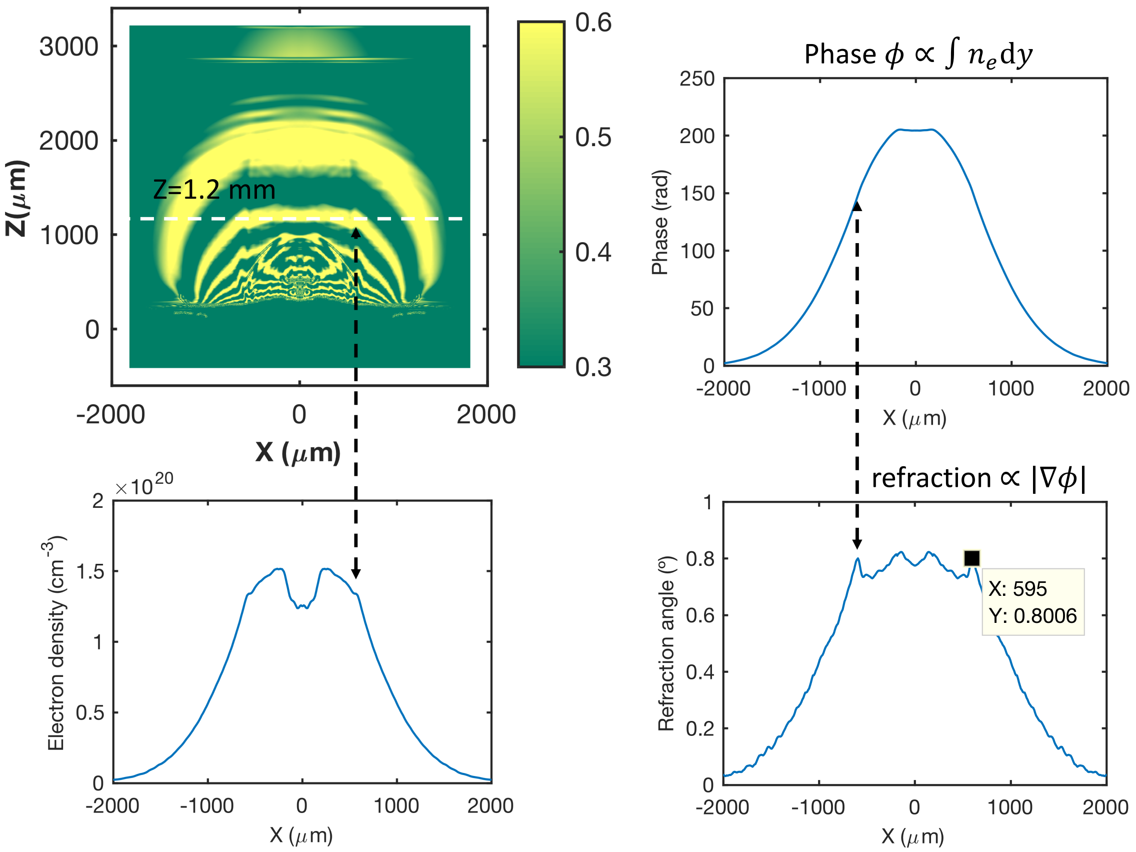

Figure 4.10: Synthetic AFR image, electron density profile at $z = 1.2$ mm, phase lineout of the wave front, refraction angle lineout. The dashed lines indicate the position of the blast wave ($x = 595$ μm). The density depression in the center is shown in the density profile.

4.9 Strong SBS in large-scale PIC simulations

The mechanism of the pump-depletion cannot be confirmed directly due to the lack of the spectrally-resolved SBS measurements. However, large-scale 2D PIC simulations suggest that non-linear SBS bursts can grow in the $n_e < 0.05\ n_c$ region depleting the laser [131]. This SBS location agrees with the observed pump-depletion at the laser onset. The simulation covered a 900 μm longitudinal length where n_e increased from 0.01 to 0.28 n_c. On average, only 25% laser energy can reach $0.05n_c$. However, its 10 ps simulation period is not long enough to show the ns-scale pump-depletion dynamics.

4.9.1 SBS saturation in reduced-scale or hybrid PIC simulations

This dynamic pump-depletion has also been observed in small length-scale PIC or ns-scale hybrid simulations, in which the SBS reflectivity drops to a few percent after a high-reflectivity period [134, 135, 136, 137]. Ref. [134, 135] have studied a 10^{16} W/cm^2 1-μm laser penetrating a 40 μm thick $0.3n_c$ H^+ plasma. The SBS reflectivity dropped at 6.5 ps after the laser onset. This fast saturation is consistent with Eq. (4.5) which predicts that IAWs in this small plasma would break at 6.2 ps. The few percent reflectivity after the saturation also supports the laser penetration observed in our experiments.

4.9.2 Implications

This ns-scale dynamic pump-depletion can explain why most PIC simulations show stronger SBS than the experiments do. The simulations in Ref. [33, 34, 35] have ~mm sized plasmas but the simulation times (<100 ps) are not long enough for the SBS to saturate. According to Eq. (4.7), the SBS in their simulations would saturate after 500 ps. Although Ref. [61] simulated a smaller (160 μm) D^+ plasma, the simulation time (5 ps) is still one order shorter than the calculated SBS saturation time from Eq. (4.5). These simulations are still in the SBS growth phase, so the calculated high reflectivity is reasonable. On the other hand, in the previous experiments [46, 56, 63, 64, 65, 40, 67], the low SBS reflectivity may be caused by the small plasma scale and the low temperature. Our experiments show no obvious pump-depletion with a smaller plasma ($L_n \sim 140$ μm), since the signals of SRS from $n_\mathrm{e} > 0.1\ n_\mathrm{c}$ region appeared simultaneously with the interaction laser. Eq. (4.5) (4.6) also suggest that the SBS would saturate faster in a low-temperature small-scale plasma. Thus, the measured low SBS reflectivity in previous experiments is not in disagreement with our model.

This strong pump-depletion can affect the laser–shock energy coupling in multiple ways. First, the pump-depletion can block the laser from reaching the high density (up to n_c) region, where the collisional absorption dominates. Thus, the collisional absorption would be greatly reduced. On the other hand, the pump-depletion may benefit electron shock ignition [47, 48, 49, 50]. As shown in Fig. 4.9, the strong pump-depletion can inhibit and delay TPD, which can generate >100 keV electrons. SRS in low density (<0.2 n_c) region only generates hot electrons with moderate temperature $T_\mathrm{hot} < 50$ keV since $T_\mathrm{hot} \sim m_\mathrm{e} v_\mathrm{ph}^2/2$. Effectively, the pump-depletion can lower the hot electron temperature, which may explain why T_hot's are lower in our experiments [127] (~40 keV) than those in small-scale experiments [46, 45] (60–70 keV). This effect favors the electron shock ignition since the low-T_hot electrons were predicted to be able to generate the ignition shock more efficiently [48].

4.10 Conclusion

In conclusion, the first experiments to characterize LPI at full-scale shock ignition-relevant laser intensity and plasma conditions have shown evidence of strong pump-depletion of the spike pulse, which is in contrast with previous smaller-scale experiments where SBS was suppressed. This pump-depletion was observed to start at the ~0.02 n_c low-density region and progress into 0.1–0.2 n_c region over the first 0.5 ns of the spike pulse. This dynamic agrees with the IAW-breaking SBS saturation model. This SBS saturation mechanism can explain the reflectivity discrepancy between previous PIC simulations and experiments, where simulations with significantly shorter time-scale overpredicted SBS and low SBS is expected in previous experiments with either low intensities or small-scale plasmas. The IAW-breaking may further perturb the plasma and impact other LPIs [138], which has not been considered in SI-scheme so far. Furthermore, the strong pump-depletion would inhibit the collisional laser absorption in the megajoule-scale SI scheme, but may benefit electron shock ignition by reducing the TPD generated high energy electrons. Effects of the overlapped beams on LPI and hot electron generation in SI require further investigation.

This chapter is currently being prepared for the publication: "Pump-depletion Dynamics and Saturation of Stimulated Brillouin Scattering in Shock Ignition Condition", S. Zhang, J. Li, C. M. Krauland, H. Reynolds, S. Muller, F. N. Beg, W. Theobald, C. Ren, C. Stoeckl, D. Haberberger, T. Filkins, D. Turnbull, R. Betti, E. M. Campbell, J. Trela, D. Batani, R. Scott, M. S. Wei. The dissertation's author is the primary investigator and author of this paper.

Chapter 5

Experimental Study of Hot Electron Generation in Shock Ignition Relevant High-Intensity Regime with Large Scale Hot Plasma

5.1 Introduction

As shown in Ch. 4, laser–plasma instabilities deplete nearly 100% of the laser energy, which would inhibit the collisional laser absorption. However, previous simulations predicted that the hot electrons with the temperature $T_{\text{hot}} < 150$ keV may benefit the full-scale shock ignition with a significant gain increase as well as expand the parameter space for robust ignition designs. [25, 22] Since the plasma density scale-length and the temperature can influence the competition in LPIs, such as that between stimulated Raman scattering (SRS) and two-plasmon decay (TPD) [54, 60], the characterization experiments for $\sim 10^{16}$ W/cm^2 lasers in large scale ($L_n > 300$ μm) and high temperature

(>keV) plasmas are warranted. With the capability to create those large plasmas [116], a planar geometry experiment on OMEGA EP is an efficient platform to characterize the LPIs and the hot electrons for the SI-relevant ~10^{16} W/cm^2 lasers.

In this chapter, a planar target experiment on OMEGA EP is presented, where hot electron generation in SI-relevant plasmas was characterized and compared for the first time with multi-kilojoule infrared (IR) and ultraviolet (UV) lasers at shock ignition relevant intensities. It is found that the IR laser generated hot electrons have a moderate temperature ($T_{\mathrm{hot}} \sim 90$ keV) with the energy conversion efficiency of ~2.4%, while the UV laser couples ~0.8% energy to hot electrons with $T_{\mathrm{hot}} \sim 27$ keV. With the moderate temperature and the higher energy conversion efficiency, IR or green lasers may be viable for generating the ignition shock in the SI scheme. Therefore, studies of LPIs at SI-relevant intensities with IR lasers (i.e., this dissertation) are an important step in scoping the viability of such a proposal.

This chapter is organized as follows. The experimental setup is shown in Sec. 5.2. The large plasma profiles are characterized and compared to the radiation hydrodynamic simulations as detailed in Sec. 5.3. The hot electron results are described in Sec. 5.4.1 and Sec. 5.4.2. The low coupling in the UV laser case may be due to its off-normal incidence, and the resultant refraction in the large plasma as discussed in Sec. 5.4.3. A discussion and summary is provided in Sec. 5.5.

5.2 Experimental setup

The planar target experiment was performed using the 4-beam OMEGA EP laser facility [68] at the Laboratory for Laser Energetics (LLE), University of Rochester. Figure 5.1 depicts the beam configuration and the viewing directions of the main diagnostics. One or two 3ω UV ($\lambda_{\mathrm{UV}} = 0.351$ μm) lasers smoothed by 8th order super-Gaussian 750

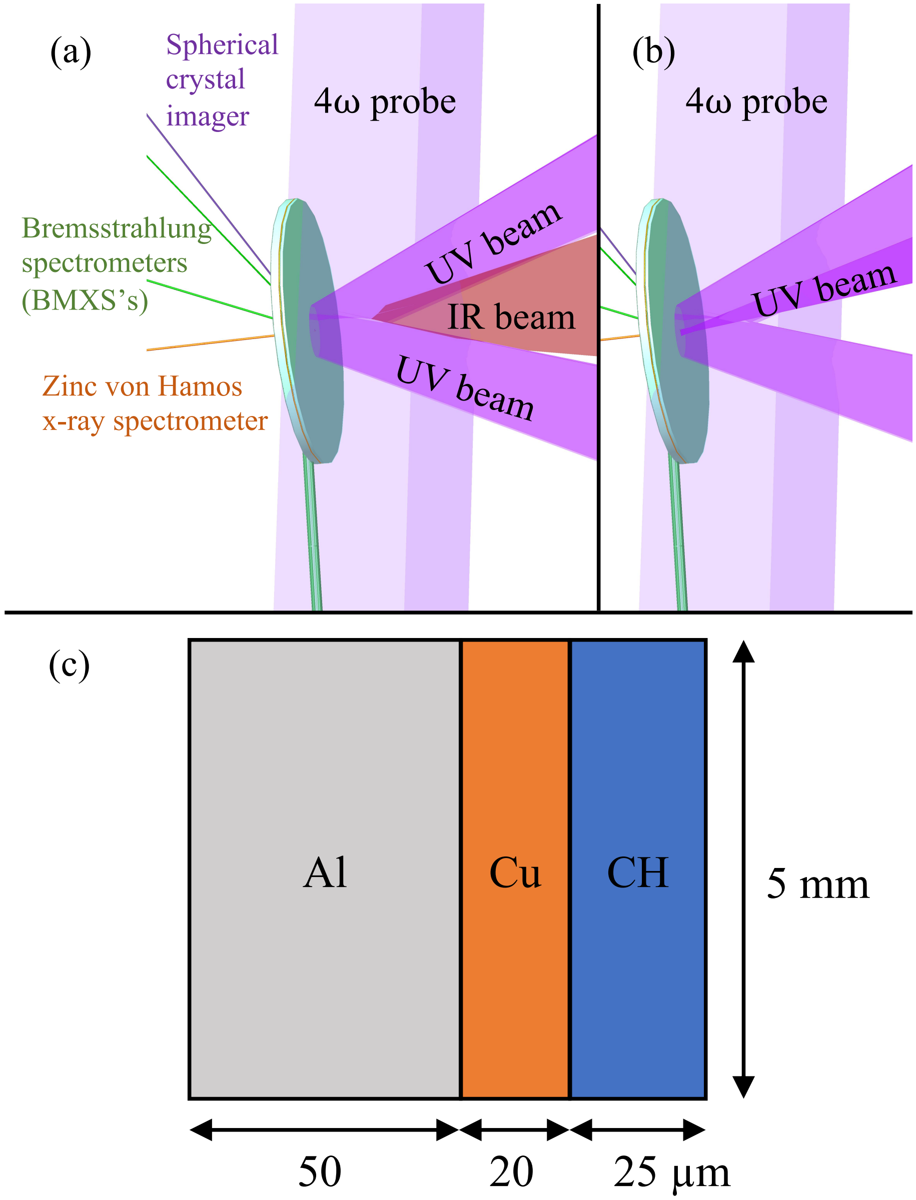

Figure 5.1: Laser, main diagnostic and target configurations with (a) IR interaction beam and (b) UV interaction beam. One or two long-pulse UV beams with the overlapped intensity of 2.0–3.6$\times 10^{14}$ W/cm^2 were used to create the large-scale plasma. A 4ω probe diagnostic system was used to characterize the electron density profile. Bremsstrahlung emission spectra were detected by two BMXSs. The hot electron excited Cu Kα radiation was measured by a spherical crystal imager and an x-ray spectrometer. (c) is the target configuration with CH ablator facing lasers.

μm spot size distributed phase plates (SG8-750 DPP) [103] delivered 1.8 kJ (one beam) or 6.4 kJ (two beams) total energy in a 2-ns (one beam) or 4-ns (two beams) square pulse to the target ablation surface with the overlapped average intensity of 2.0–3.6×10^{14} W/cm^2 to create a high temperature ($1.1-1.8$ keV) and long scale-length plasma ($L_n \sim 330$ μm in the UV's 0.1–0.25 n_c region, and $L_n \sim 380$–450 μm in the IR's 0.1–0.25 n_c region). The plasma conditions and the characterizations are described in Sec. 5.3 and listed in Table 5.1. The plasma-creation beams were followed by the main-interaction beam that was timed at 1.5 ns after the start of the plasma-creation beams. This interaction beam was either a high-intensity UV laser (1.4 kJ, $f/6.5$, $\sim10^{16}$ W/cm^2 in vacuum) in a 1-ns square pulse at 23° off the target normal, or a normal incident IR beam (∼100 ps, up to 2.5 kJ, $\lambda_{\mathrm{IR}} = 1.054$ μm, $f/3.2$). The UV interaction beam was tightly focused with a focal spot size of ∼100 μm on its quarter critical density plane ($n_c/4 = 2.25\times10^{21}$ cm^{-3}), which was 200 μm above the initial solid target surface. The IR beam was defocused with a 60 μm spot (for the 1 kJ case) or a 300 μm spot (for the 0.7 kJ and the 2.5 kJ cases) at its quarter critical density position ($n_e = 2.5\times10^{20}$ cm^{-3}), which was ∼1 mm above the initial solid CH surface according to the radiation-hydrodynamic simulations described in Sec. 5.3. The average vacuum intensity of the 2.5 kJ IR beam is 2×10^{16} W/cm^2. To quantify the laser hot spots, we used a focal-spot-diagnostic [139] to indirectly measure the spot profile at 1.7 mm above the target surface. This shows that the hot spot regions where the localized intensity is two times higher than the average intensity contains less than 10% of the total energy. The actual average intensities could be reduced to 1.5×10^{15} W/cm^2 for the 0.7 kJ laser and 5×10^{15} W/cm^2 for the 1.0 kJ and 2.5 kJ lasers given that the 300 μm spot of the 2.5 kJ IR laser was observed to spread to 670 μm and the 60 μm spot of the 1.0 kJ IR beam spread to 410 μm from the measured 4ω probe data (see Fig. 5.4)

The experiments used a 3-layer planar solid target (25 μm CH/20 μm Cu/50 μm Al), shown in Fig. 5.1(c). The low-intensity long pulse UV beams irradiated the CH front layer to form a CH coronal plasma. The Cu layer served as a tracer for hot electrons' detection since they excite Cu Kα x-rays (8.05 keV). The 50 μm Al back layer provided the extra stopping power for the hot electrons to inhibit their recirculation.

To characterize the plasma density profiles including the laser–induced perturbations, an ultrafast (10-ps) fourth-harmonic 4ω probe beam [115] ($\lambda_p = 263$ nm) was used to capture the angular filter refractometer [116] and shadowgraphy images. To diagnose the hot electrons' characteristics and energy deposition in the target, several types of x-ray diagnostics were deployed. The total yield of the Cu Kα fluorescence emission excited by the hot electrons was measured by a calibrated Zinc von Hamos x-ray spectrometer (ZVH) [110]. This spectrometer uses a curved HOPG crystal in von Hamos geometry [140] to diagnose x-ray spectrum in the range of 7 – 10 keV. A spherical crystal imager (SCI) [109] was used to image the Cu Kα spot to infer the hot electron angular spread. The hot electron-produced bremsstrahlung from the target was mainly diagnosed by two identical bremsstrahlung hard x-ray spectrometers (BMXSs) [69] at 25°, and 65° off the target rear normal, respectively. The BMXSs use a stack of 15 image plates as detectors with plastic and metal filters interleaved in-between. It can measure the x-rays in the range from 17 keV up to 800 keV. X-ray pinhole cameras (XRPHC) with 152.4 μm Be filters were used to image the x-ray emission in the energy range from 2 to 7 keV [141].

5.3 Plasma characterization

We used both experimental measurements and simulations to characterize the large coronal plasma. Two-dimensional radiation-hydrodynamic simulations using the FLASH code [123, 128] were performed to model the plasma generated by the low-intensity UV long pulse lasers. The simulation was conducted in 2D cylindrical coordinates with 3D-in-2D laser ray tracing, which traces the laser rays in 3D and then

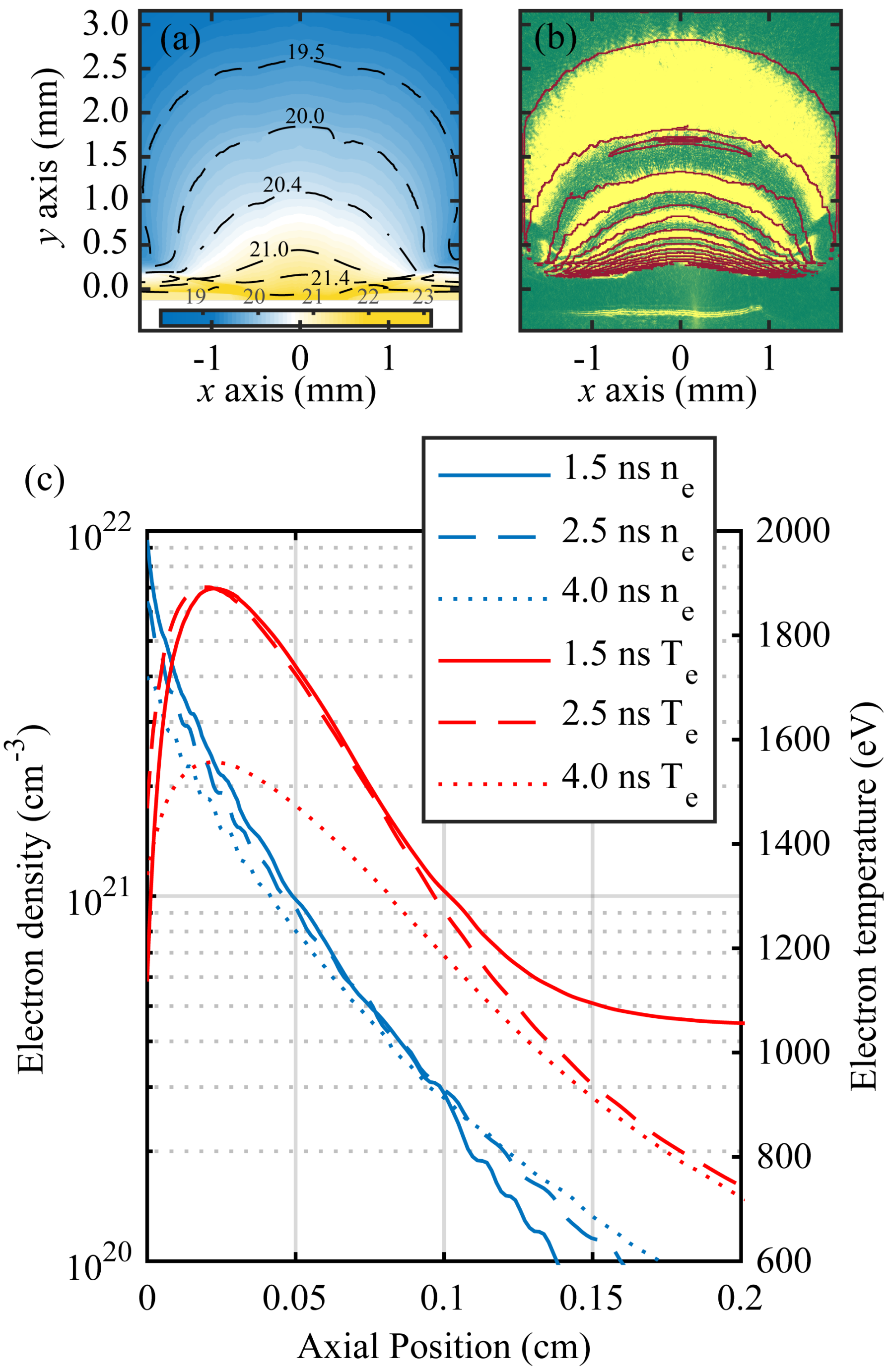

Figure 5.2: Simulated plasma profiles, experimental and synthetic AFR images: (a) the electron density profile $\log_{10}(n_\mathrm{e})$ at 4.0 ns simulated by FLASH, n_e is in cm^{-3}. The contours with $\log_{10}(n_\mathrm{e}) = 20.0, 20.4, 21.0, 21.4$ represent the positions of IR's $n_\mathrm{c}/10$, $n_\mathrm{c}/4$, n_c, and the UV's $n_\mathrm{c}/4$; (b) the experimental AFR image at 4.0 ns overlapped with the contour of the synthetic AFR image, which is calculated with the density profile in (a). The initial target position captured by the 4ω probe registration shot is marked with yellow straight lines. $y = 0$ is the original target surface in (a) and (b). (c) FLASH simulated electron density and temperature profiles along the axis normal to the target center at 1.5 ns, 2.5 ns, and 4.0 ns.

projects the deposited energy on the R-z plane. The laser energy deposition was calculated based on the inverse-bremsstrahlung model. The FLASH simulations used the same experimental laser and target parameters. Tabulated equation of state (EOS) and multigroup opacity models for the solid CH used in the FLASH simulation are obtained with IONMIX4 [142]. Figure 5.2(a) shows the FLASH-simulated electron density profile with density contours (dashed lines) at the end of the UV plasma creation beam (4.0 ns). The density contours from 10^{20} to $10^{21.4}$ cm^{-3} represent the positions of the IR's $0.1, 0.25, 1\ n_c$, and the UV's $0.25 n_c$.

In our experiments, electron density profiles were diagnosed by a refraction angle contour map of the 4ω probe beam with an Angular Filter Refractometer (AFR) [116]. In the AFR images, certain bands of refraction angles are blocked by the filter made of concentric opaque rings on the Fourier plane of the 4ω probe beam imaging system. Because the refraction angle is proportional to the transverse gradient of the accumulated phase of the probe beam traversing through the plasma, the electron density profile can be calculated with cylindrical symmetry assumption since the refractive index is related to the plasma density. With these refraction angle contour maps, the 4ω AFR diagnostic can measure electron densities up to 10^{21} cm^{-3}. [116]

Figure 5.2(b) shows the experimentally measured AFR image (green and yellow) captured at 4.0 ns overlapped by the red contour of a synthetic AFR image. The synthetic AFR image was simulated by the AFR imitation program based on the simulated density profile as shown in Fig. 5.2(a). The synthetic AFR image agrees with the measured AFR image in the experiment. The AFR images captured right after the main interaction beam (at 2.5 ns for UV and 1.6 ns for IR) were also compared to the corresponding synthetic AFR images. Both synthetic AFR images agree well with the experimental images except for the region where the main interaction occurs. For example, Fig. 5.6(b) and Fig. 5.4 show that the plasmas were strongly perturbed by the high-intensity UV and IR beams.

The agreement between the synthetic and measured AFR images at various times provides us with confidence in the FLASH simulated plasma conditions for our experiments. Fig. 5.2(c) shows the simulated electron density and temperature profiles along with the target normal axis at 1.5 ns (before the high-intensity IR and UV interaction beams), 2.5 ns (at the end of the high-intensity UV interaction beam), and 4.0 ns. These density profiles can be fitted with a simple exponential function in the $n_c/10 - n_c/4$ region:

$$n_e = n_0 \exp(-x/L_n), \tag{5.1}$$

where x is the distance from the target surface, and L_n is the density scale length. For the IR interaction laser incident at 1.5 ns, the plasma had $L_n \sim 380$ μm and $T_e \sim 1.2$ keV in the IR's $n_c/10 - n_c/4$ region (1.0×10^{20}–2.5×10^{20} cm^{-3}). For the UV interaction laser from 1.5 ns to 2.5 ns, the plasma had $L_n \sim 330$ μm with $T_e \sim 1.8$ keV in the UV's $n_c/10 - n_c/4$ (0.90×10^{21} cm^{-3} $- 2.25 \times 10^{21}$ cm^{-3}) region. These plasma parameters are summarized in Table 5.1. These plasma length scales are one-two times larger than previous OMEGA spherical experiments [56, 46] but similar to the length scale of the previous planar experiment with $\sim 10^{15}$ W/cm^2 lasers [41] and close to the predicted scales in the SI designs for NIF [25].

5.4 Experimental Results

5.4.1 Measurement of the hot electron temperature and total energy

The temperature and total energy of the hot electrons generated by the UV or IR interaction beam were inferred from the bremsstrahlung x-ray spectra measured by BMXSs. The first 8 layers of Image Plates (IP) dosimeters in the BMXS recorded x-ray signal with the energy range from 17 keV to 180 keV. This sufficiently covers the bremsstrahlung x-ray emission produced by the hot electrons with a temperature < 100 keV. Figure 5.3 shows the sample measured doses in the IP dosimeters of the BMXS at 25° off the target back normal as well as the synthetic BMXS doses fitting these measured doses. To extract the temperature and total energy of the hot electrons from the measured bremsstrahlung spectra, we fit the synthetic BMXS doses to the measured signals. These synthetic doses were simulated by using Monte-Carlo code ITS-3.0 [70] to calculate the emitted x-ray spectrum from the target as well as the BMXS IP detectors' response to these x-rays. To model the target emission for any electron spectrum, we injected 81 narrow spectral bins of hot electrons logarithmically spaced from 10 keV to 100 MeV and recorded the emitted x-ray spectra at different target lines of sight. The target absorption of the x-rays is considered in ITS-3.0. These simulations were performed with a compressed target profile from the 1D HYADES simulation with SESAME EOS tables, in which the laser energy was scaled down by 50% to compensate for the lack of the transverse expansion. With this scaled energy, the simulated coronal plasma profile is consistent with the 2D FLASH simulation. The hot electrons were injected normal to the target in the ITS calculations with a 1D relativistic Maxwell-Jüttner energy distribution,

$$f(E) \propto \left(1+\frac{E}{m_\mathrm{e}c^2}\right)\left[\left(1+\frac{E}{m_\mathrm{e}c^2}\right)^2-1\right]^{\frac{d-2}{2}} e^{-E/T_\mathrm{hot}} \tag{5.2}$$

where E is the hot electron kinetic energy, $m_\mathrm{e}c^2$ is the rest energy of an electron (0.511 MeV), d is the dimension (chosen as 1) and T_hot is the hot electron temperature. For the high-intensity IR laser interaction experiments (1.0 kJ and 2.5 kJ cases), this directional beam assumption is supported by the observed small Cu Kα spots recorded by the SCI diagnostic (470 ± 10 μm full-width-half-max) which are similar to the sizes of the spread laser spots (410 μm for the 1.0 kJ IR as shown in Fig. 5.4 and 670 μm for the 2.5 kJ

Table 5.1: Laser and plasma parameters, and the generated hot electron temperature (T_{hot}) and the energy conversion efficiency ($E_{\mathrm{hot}}/E_{\mathrm{L}}$). T_{hot} and $E_{\mathrm{hot}}/E_{\mathrm{L}}$ are the weighted averages of the best fitting parameters for each BMXS. The doses due to the plasma creation beam have been subtracted for the analysis of the interaction beam produced hot electrons. T_{e} and L_n are the plasma electron temperature and density length scale in the $n_{\mathrm{c}}/10$–$n_{\mathrm{c}}/4$ region from the FLASH simulations. The errors are the change of the temperature and the length scale in this region. The intensities were calculated according to the AFR-measured spot size at the $n_{\mathrm{c}}/4$.

Laser energy	Intensity (10^{15} W/cm^2)	T_{e} (keV)	L_n (μm)	T_{hot} (keV)	$E_{\mathrm{hot}}/E_{\mathrm{L}}$
6.4 kJ UV	0.4	1.8 ± 0.1	330 ± 40	24 ± 3	$0.7 \pm 0.2\%$
1.4 kJ UV	10	1.8 ± 0.1	330 ± 40	27 ± 9	$0.8 \pm 0.7\%$
1.0 kJ IR	5	1.1 ± 0.1	450 ± 20	65 ± 9	$2.7 \pm 0.5\%$
2.5 kJ IR	5	1.2 ± 0.1	380 ± 30	87 ± 10	$2.4 \pm 0.4\%$

IR [127]). In addition, the Cu layer is ~1 mm away from the source of the hot electrons produced by TPD and/or SRS, which can only occur in the $n_{\mathrm{e}} \leq n_{\mathrm{c}}/4$ region. In our experiments, the beam divergence cannot be characterized by quantifying the anisotropy of the x-ray emissions, since the x-ray emissions induced by the low energy electrons are close to isotropic.

We fit the synthetic x-ray doses on IPs to each BMXS separately and average the two sets of fitting results to infer the T_{hot} and the $E_{\mathrm{hot}}/E_{\mathrm{L}}$ as listed in Table 5.1. To fit these synthetic doses to the measured BMXS signals, we tuned T_{hot} and E_{hot} of the hot electron spectrum to minimize the weighted, reduced (per degree of freedom) χ^2 value as described in Ref. [69]. Fig. 5.3 illustrates the experimental 25° BMXS x-ray doses on each IP (points) and their best fitted synthetic doses (lines). The confidence intervals for each fitting is calculated by error propagation. Then we combined the confidence intervals of each fitting with the differences of the two sets of fitting results to calculate the confidence intervals of the averaged fitting results as listed in Table 5.1.

Both the plasma-creation lasers and the high-intensity UV laser generated $T_{\mathrm{hot}} \sim$ 25 keV hot electrons. In Fig. 5.3, the 25° BMXS spectrum from only the 6.4 kJ low-

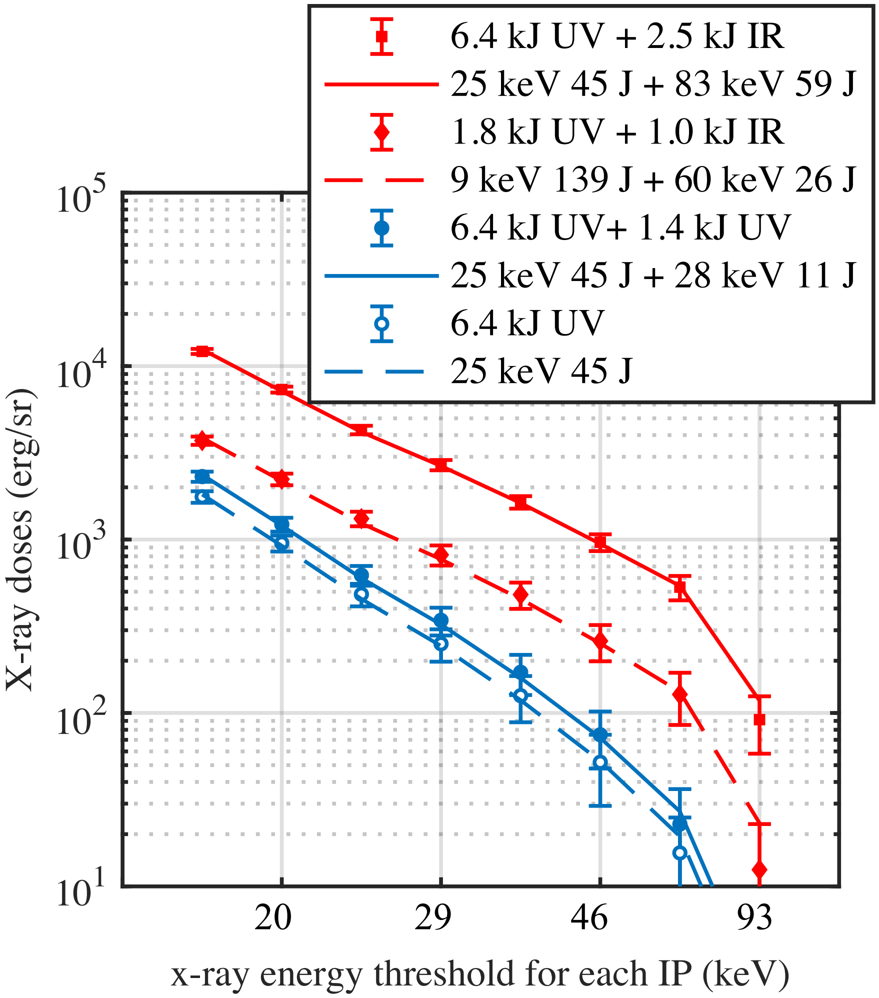

Figure 5.3: Hard x-ray energy doses on the phosphor layers in the 25° BMXS IPs. Points represent the experimental total doses, and lines are the synthetic doses from Monte Carlo simulations, which fit the 25° BMXS doses. The temperature and the beam energy in those simulations are labeled. The first components are the hot electrons in the reference experiments with only the plasma creation beams. The second components are the hot electrons from the interaction lasers. The inferred electron beam energy of the 1.8 kJ UV plasma creation laser have a large uncertainty 170% due to this low temperature.

intensity UV lasers (hollow blue circles) can be fitted for the hot electrons with T_{hot} = 25±5 keV and a total energy of 45±20 J (dashed blue line). With the additional 1.4 kJ high intensity UV interaction beam injected, the x-ray doses in each IP rose by 28%–47% shown as the blue dots in Fig. 5.3. These increased doses can be fitted by a 11 ± 15 J, 28 ± 15 keV hot electron beam. Averaged the fittings for both BMXS results, $T_{\text{hot}} = 27 \pm 9$ keV and $E_{\text{hot}}/E_{\text{L}} = 0.8 \pm 0.7\%$ as listed in Table 5.1. These large uncertainties are due to the low signal increase compared with the uncertainty of the doses from the 6.4 kJ UV lasers.

Compared to the UV interaction laser, the 2.5 kJ IR interaction laser created higher temperature hot electrons ($T_{\text{hot}} = 87 \pm 10$ keV) with higher energy conversion efficiency $E_{\text{hot}}/E_{\text{L}} = 2.4 \pm 0.4\%$. The x-ray doses induced by the 6.4 kJ UV lasers have been subtracted in these fittings. Besides the 1D Maxwell-Jüttner distribution, we have also tested the spectrum of the exponential energy distribution with the same spectral bins (10 keV–100 MeV), which suggests $T_{\text{hot}} = 75 \pm 9$ keV and $E_{\text{hot}}/E_{\text{L}} = 2.2 \pm 0.4\%$. The two-temperature spectrum was also tested; however, in the best fit, the two components have the same temperature.

The hot electron generation from the IR interaction laser is sensitive to the laser intensity. A low-intensity (~1.5×10^{15} W/cm^2) 0.7 kJ IR interaction laser only raised the x-ray doses on BMXS by ~10% which are in the range of the uncertainties of the dosimeters. If we assume $T_{\text{hot}} = 25$ keV, the fitting resulted in $E_{\text{hot}}/E_{\text{L}} \sim 0.7\%$, similar to that of the UV plasma creation lasers. In this experiment, the AFR image shows no clear perturbation. Since the 0.7 kJ IR laser was focused with the same spot size (300 μm) at $n_c/4$ as the 2.5 kJ IR laser, we expect the beam would spread to 670 μm as the 2.5 kJ laser, resulted in this ~1.5×10^{15} W/cm^2 low intensity. This low intensity may explain the inefficient hot electron generation measured in the experiment. When we increase the laser intensity by focusing the laser to a nominal 60 μm spot in the 1.0 kJ IR laser experiment, this IR laser created an electron beam with $T_{\text{hot}} = 65 \pm 9$ keV and $E_{\text{hot}}/E_{\text{L}} = 2.7 \pm 0.5\%$ similar to the 2.5

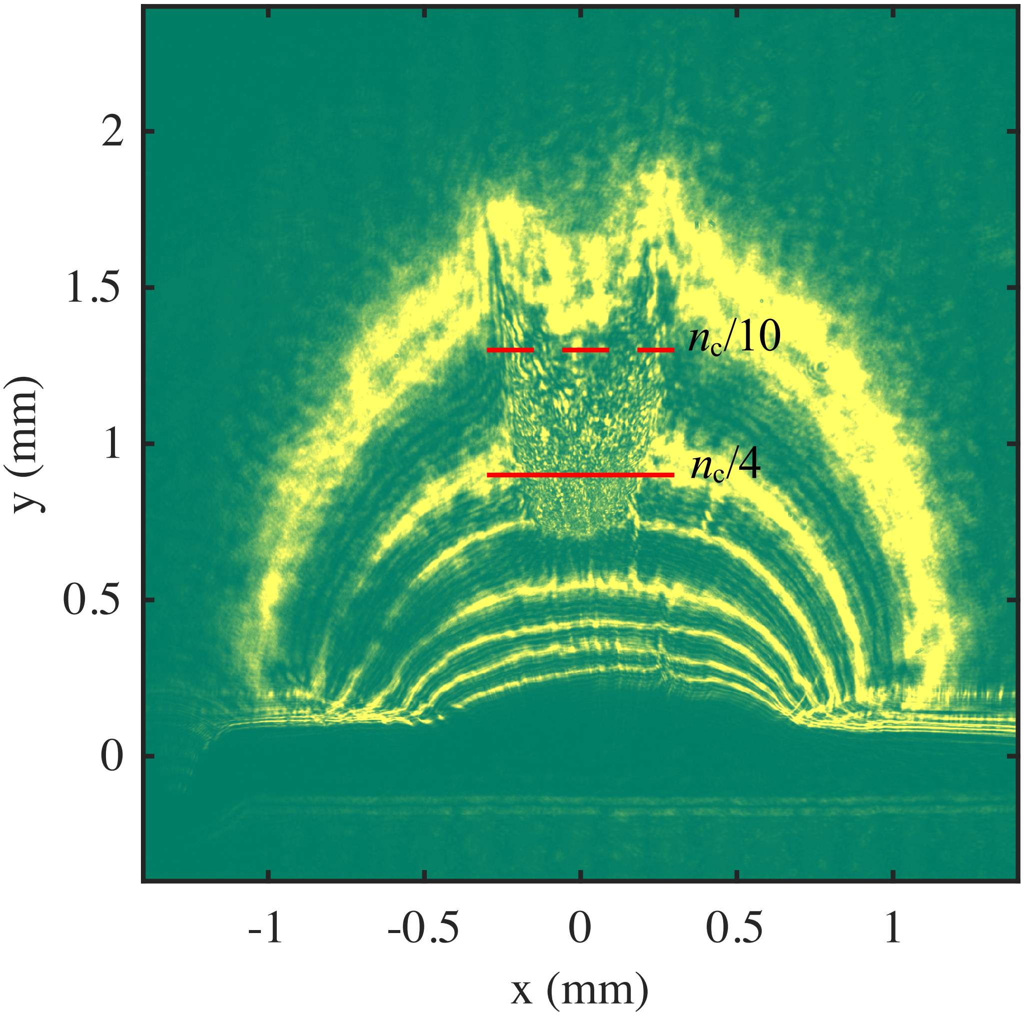

Figure 5.4: AFR image of the 1 kJ IR shot. The original 60 μm laser spot spread to a 410 μm wide interaction region. The dashed and solid red lines represent the IR's $n_c/10$ and $n_c/4$ positions of the plasma, respectively.

kJ IR experiment. This laser spot spread to 410 μm, as shown in Fig. 5.4, resulted in a ~5×10^{15} W/cm^2 actual intensity similar to the 2.5 kJ laser. The plasma in this experiment has similar parameters (L_n = 450 μm and T_e = 1.1 keV) which was created by a 1.8 kJ 2-ns 2×10^{14} W/cm^2 UV laser before the incidence of the IR interaction laser at 1.5 ns. In this analysis of the IR-induced hot electrons' characteristics, we subtracted the x-ray doses induced by the 1.8 kJ UV laser, which was scaled down linearly from the doses in a reference experiment with a 2.0 kJ UV laser. Figure 5.4 also shows strong perturbations in the $n_\mathrm{e} \sim 0.1$–$0.25\ n_\mathrm{c}$ region which induced the missing band at $y \sim 1$ mm. This location indicates that the strong density perturbation is induced by SRS and/or TPD.

5.4.2 Hot electron induced Cu Kα emission

Besides the bremsstrahlung signal, the measured Cu Kα radiation also independently demonstrate the generation of hot electrons from both UV and IR interaction lasers. Hot electrons with energies higher than the Cu K-shell binding energy (8.98 keV) reaching the Cu layer can produce Kα x-rays. Figure 5.5 displays the Cu Kα yields as a function of the main interaction laser beam energy, which are the total yields subtracted by the yield of the UV background shot, with target transparency corrected assuming a uniform emission. The yield induced by the 1.0 kJ IR was calculated by subtracting the yield of the 2.0 kJ low-intensity UV laser. Since in this 1.0 kJ IR experiment, the ZVH was placed at the laser side, but in other experiments, the ZVH was placed at the back of the target, the assumption of the uniform emission may cause the overcorrection of the Cu layer transparency. This potential overcorrection is plotted as the negative 50% uncertainty in Fig 5.5. For reference, the 6.4 kJ UV plasma creation beams produced hot electrons which resulted in $7.8\pm1.6\times10^{11}$ photon/sr of Cu Kα yield. The linear scaling of the 6.4 kJ UV laser is shown as the blue dashed line, in which the slope is its yield divided by the incident laser energy, 1.2×10^{11} photon/(sr·kJ).

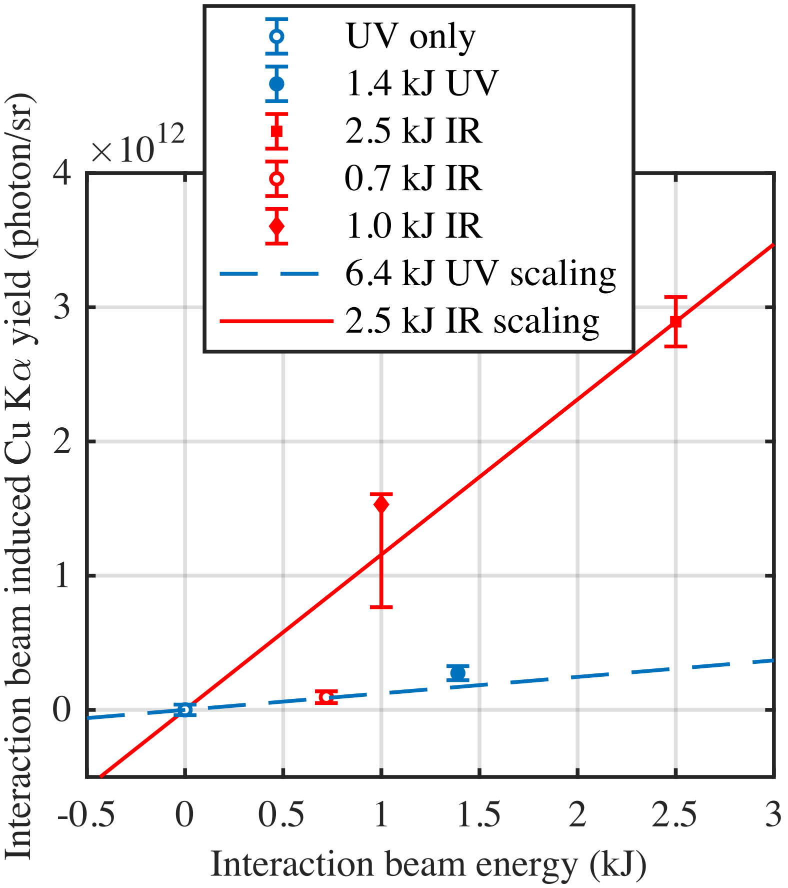

Figure 5.5: Cu Kα yield induced by the interaction beam versus the interaction laser energy with target transparency corrected. The UV plasma creation laser components of the Cu Kα were subtracted from the original results. The dashed blue line represents the linear yield scaling with the energy of the UV plasma creation lasers. The slope of the dashed line is the Cu Kα yield induced by the UV plasma creation lasers (7.8×10^{11} photon/sr) divided by the laser energy (6.4 kJ). The red solid line represents the linear yield scaling of the 2.5 kJ IR laser in which the slope is the Cu Kα yield induced by the IR laser (2.9×10^{12} photon/sr) divided by the 2.5 kJ laser energy. The uncertainty in the plot is the 5% random error induced by the ZVH's alignment uncertainty. The large negative error (50%) for the 1.0 kJ IR is due to potential overcorrection of the target transparency since the ZVH was placed at a different line-out-sight in this experiment. The 20% systematic uncertainty of the yield calibration was not plotted.

The UV interaction laser produced Cu Kα with higher yield per laser energy than the plasma creation lasers, shown in the Fig. 5.5 as the solid blue point (2.7×10^{11} photon/sr) compared to the blue dashed line. The increased ZVH signal induced by this high-intensity UV laser is beyond the ZVH's alignment-induced random error (5%). The yield in unit laser energy is also 70% higher than that from the plasma creation UV lasers. This increase of the yield in unit laser energy is consistent with the increase of the beam temperature and the energy conversion efficiency from laser to hot electrons discussed in Sec. 5.4.1.

Enhanced generation of hot electrons from the IR interaction laser is also confirmed by the measured Cu Kα x-rays. In Fig. 5.5, the solid red square and diamond points are from the 2.5 kJ and 1.0 kJ IR laser respectively, the same experiments discussed in Sec. 5.4.1 with the interaction intensity at 5×10^{15} W/cm^2. The overlaid red solid line is the linear scaling of the 2.5 kJ IR laser, in which the slope is the Cu Kα yield per unit IR laser energy as 1.2×10^{12} photon/(kJ$\cdot$sr). This is six times of the yield per unit laser energy from the UV interaction laser. The yield induced by the 1.0 kJ IR is also consistent with the linear scaling. This IR-induced increase in the Cu Kα yield is also consistent with the higher hot electron energy coupling and the higher hot electron temperatures as shown in Table 5.1. In the ITS simulations fitting the BMXS spectra, the simulated Cu Kα yield in the 2.5 kJ IR shot is also 6 times as much as the simulated yield of the 1.4 kJ UV shot. Compared to the ITS simulations, the measured Cu Kα yields are 36% (1.4 kJ UV) and 40% (2.5 kJ IR) less than the simulated yields, which are within the error of the ZVH's absolute calibration (20%) [110] and the BMXS's fitting errors listed in Table 5.1. In addition, this lower Cu Kα emission may also be due the effect of the resistive electrostatic field and the magnetic field around the beam. This field effect is not considered in the ITS simulations.

In contrast to the high-intensity IR cases, the low-intensity IR beam (red circle) produced Cu Kα with a similar efficiency to the UV plasma creation beams. This also agrees with the analyses of the bremsstrahlung spectra, since they indicate that this low-intensity IR laser and the UV plasma creation beams produced hot electrons with the same temperature and the same efficiency.

5.4.3 Refraction of the UV interaction beam in the underdense plasma

The observed weak coupling of the UV interaction laser to the target via hot electrons may be caused by the refraction of the laser light in the plasma, as shown in the AFR and the x-ray images in Fig. 5.6. Due to the laser configuration limitation in the OMEGA EP chamber, the high-intensity UV beam was incident at 23° off the target normal. The bent channel created by the refracted laser is shown in the AFR image in Fig. 5.6(b). Resonance absorption might occur in this turning point, since the x-ray image in Fig. 5.6(a) shows a bright dot in the bottom right, which is 270 μm away from the center of the plasma. The spot location agrees with the channel in the AFR image. The laser deflection can be induced by the ponderomotive force piling up the plasma in a transverse flow. [143] This phenomenon has also been observed in the experiments on NOVA [144, 145] and LULI-6F [36]. A refined OMEGA EP experiment with normal incident UV laser is shown in Ch. 4 and Ch. 6, in which a stable and narrow channel consistent with the $f/6.5$ UV beam focusing geometry was created along the high intensity UV beam axis (the target normal axis). This normal incident laser converted more energy (~2%) to the hot electrons primarily produced by SRS. It should be noted that, the strong refraction observed in the planar geometry with the oblique incident laser might also inhibit the laser energy absorption in spherical geometry, especially if large spot lasers were overlapped to reach the required 10^{16} W/cm^2 high intensity.

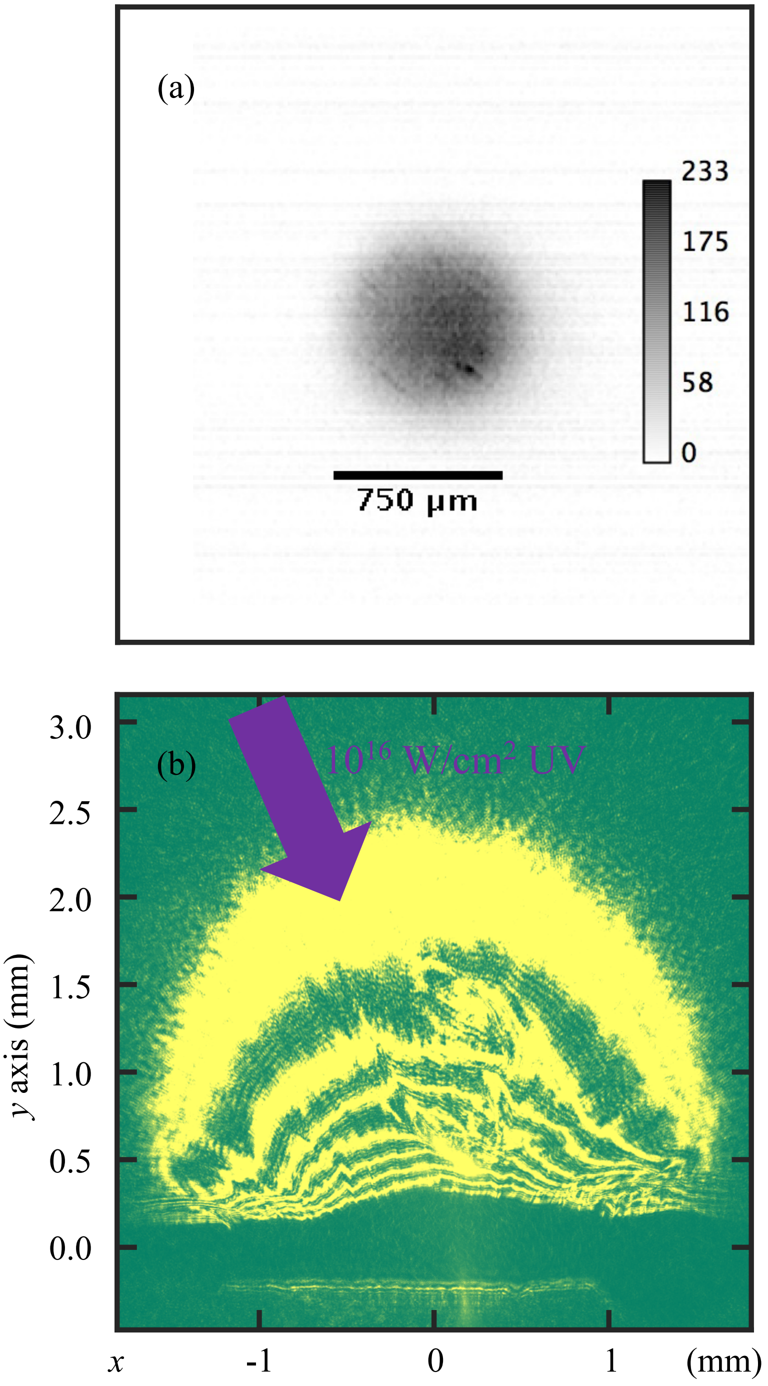

Figure 5.6: (a) X-ray image captured by x-ray pinhole camera showing the refracted UV laser illuminated bright x-ray spot 270 μm away from the plasma center (bottom right of the spot). The scale bar is the spot size of the plasma creation beam. (b) AFR image showing a bent channel generated by the UV interaction beam. The purple arrow shows the direction of the interaction UV laser.

5.5 Discussion and summary

The hot electrons generated by the IR lasers with $T_{\text{hot}} < 100$ keV could be useful for electron shock ignition, which is a shock ignition design using the hot electrons to generate the required 300 Mbar ignition shock. [50] During the spike laser, these hot electrons would be stopped by a compressed layer of CH ablator or the outer layer of the DT fuel. Their average stopping range is 22–50 mg/cm^2 in DT or 5–12 mg/cm^2 in CH [49], which means a high-pressure shock can be formed in this 5–50 μm thin layer at the surface of the compressed capsule ($\rho \sim 10$ g/cm^{-3}), as suggested in an analytical model. [48, 47] This model also shows that the peak pressure only depends on the electron beam intensity and the density of the compressed layer stopping the electrons, which indicates that with the higher conversion efficiency, the IR laser can have a lower intensity than the UV laser to generate the same high pressure. However, with the higher hot electron temperature, IR shock ignition would need a longer stopping range and consequently, a longer shock loading time, which is proportional to the stopping range. The loading time can be shortened by using a thicker CH layer to stop these hot electrons.

Compared with previous experiments, our experiments with a single high-intensity UV laser interaction beam shows a lower conversion efficiency but similar low temperature as the previous experiments when the UV laser is tightly focused to ~8×10^{15} W/cm^2. [56, 146] This low temperature suggests that these hot electrons might be generated by SRS or resonance absorption. Our experiments and particle-in-cell simulations have also shown that stimulated Brillouin scattering in this large plasma can block the high-intensity laser from reaching the $n_c/4$ region. [131] The previous IR experiments on PALS [147] have observed a similar ~90 keV hot electron component with ~2% of energy conversion efficiency and a ~40 keV component with ~4% conversion efficiency. However, that experiment was conducted with a single IR beam (~700 J in an ~300 ps full-width-half-max Gaussian pulse) interacting with the self-generated plasma ($L_n < 150$ μm), which may induce the discrepancy between that experiment and our experiment. To determine the source of the hot electrons in the IR experiments would require a spectral resolved scattered light measurement.

In summary, we have demonstrated experimentally for the first time hot electrons generation with multi-kilojoule laser energies at shock ignition high intensities in the planar geometry using both UV and IR lasers in a large-scale plasma. Inferred from the measured bremsstrahlung spectra, the high-intensity IR laser produced hot electrons with higher temperature (60–90 keV) and ~2.5% energy conversion efficiency higher than those hot electrons from UV interaction beam (27 ± 9 keV, $0.8 \pm 0.7\%$). This wavelength dependence is also shown by the measured Cu Kα yield. Besides the wavelength dependence, our experiments also show that the hot electron generation is sensitive to the laser intensity and incidence angle. With the more efficient hot electron generation and the demonstrated moderate hot electron temperature, IR lasers could be considered as the spike pulse for the electron-assisted shock ignition. More experiments will be required to further study laser–plasma instabilities and the resulting hot electron generation as well as the hot electron energy deposition in the spherical geometry.

This chapter is a reprint of the publication: “Experimental Study of Hot electron Generation in Shock Ignition Relevant High-intensity Regime with Large Scale Hot Plasmas”, S. Zhang, C. M. Krauland, J. Peebles, J. Li, F. N. Beg, N. Alexander, W. Theobald, R. Betti, D. Haberberger, E. M. Campbell, R. Yan, E. Borwick, C. Ren, and M. S. Wei, *Physics of Plasma* 27, 023111 (2020). The dissertation’s author is the primary investigator and author of this paper.

Chapter 6

Generation of Collimated Moderate Temperature Electron Beam and Laser–Plasma Interaction for Megajoule Shock Ignition

6.1 Introduction

As discussed in Sec. 2.5.2, simulations and analytic models suggest that hot electrons created from laser–plasma instabilities (LPIs), such as stimulated Raman scattering (SRS) [38] and two-plasmon decay (TPD) [39], can effectively generate this "ignition shock" [47, 48, 49]. The experimental platform where laser parameters are designed to optimize electron production for this purpose is called electron shock ignition [50]. Reference [50] suggests that 10 – 40 kJ of hot electrons in 200 ps can generate the full-scale ignition shock, citing the hot electron measurement from the reduced-scale experiments [46, 45]. This calculation assumes that T_{hot} is independent of laser intensity and electron beam intensity scales linearly with laser intensity, the authors conclude that ~10^{16} W/cm^2 lasers would produce the required hot electrons. However, many experiments [56, 41, 42, 58, 148] indicate that LPIs, $E_{\mathrm{hot}}/E_{\mathrm{L}}$, and T_{hot} are sensitive to laser and plasma conditions. In order to evaluate the feasibility of electron shock ignition, experimental studies were performed to characterize the properties of the hot electrons and the relevant laser–plasma instabilities in the full-scale conditions.

This chapter presents the experimental setup, the measurement of the hot electron divergence, and the diagnose of the LPI-induced plasma perturbations. Independent of wavelength, the laser pulses produce small divergence and moderate temperature hot electron beams as observed from a buried fluorescence layer. This directional electron beam and the observed plasma density perturbations suggest that the hot electrons are mainly generated by SRS. Corresponding Particle-in-Cell (PIC) simulations support these data. Based on the characterization, electron shock ignition would be feasible when 0.8 ns 310 TW IR or 0.3 ns 540 TW UV spherically symmetric lasers are used to generate the ignition shock.

6.2 Experimental setup

We performed the experiments on the multi-kilojoule OMEGA EP laser facility [68] at Laboratory for Laser Energetics. To produce a surrogate shock ignition coronal plasma, $2-6$ kJ UV lasers irradiate the CH coated side of a disk target, shown in Fig. 6.1(a). We use distributed phase plates to focus a 750 um uniform spot. After this large scale plasma is created, a $1-2\times10^{16}$ W/cm^2 pulse is injected into the plasma with a $100-300$ μm focal spot at the corresponding laser wavelength's quarter critical density contour surface. This location is based on radiation hydrodynamic simulations using FLASH [123, 128] with PROPACEOS EOS table and have been benchmarked with experimental Angular

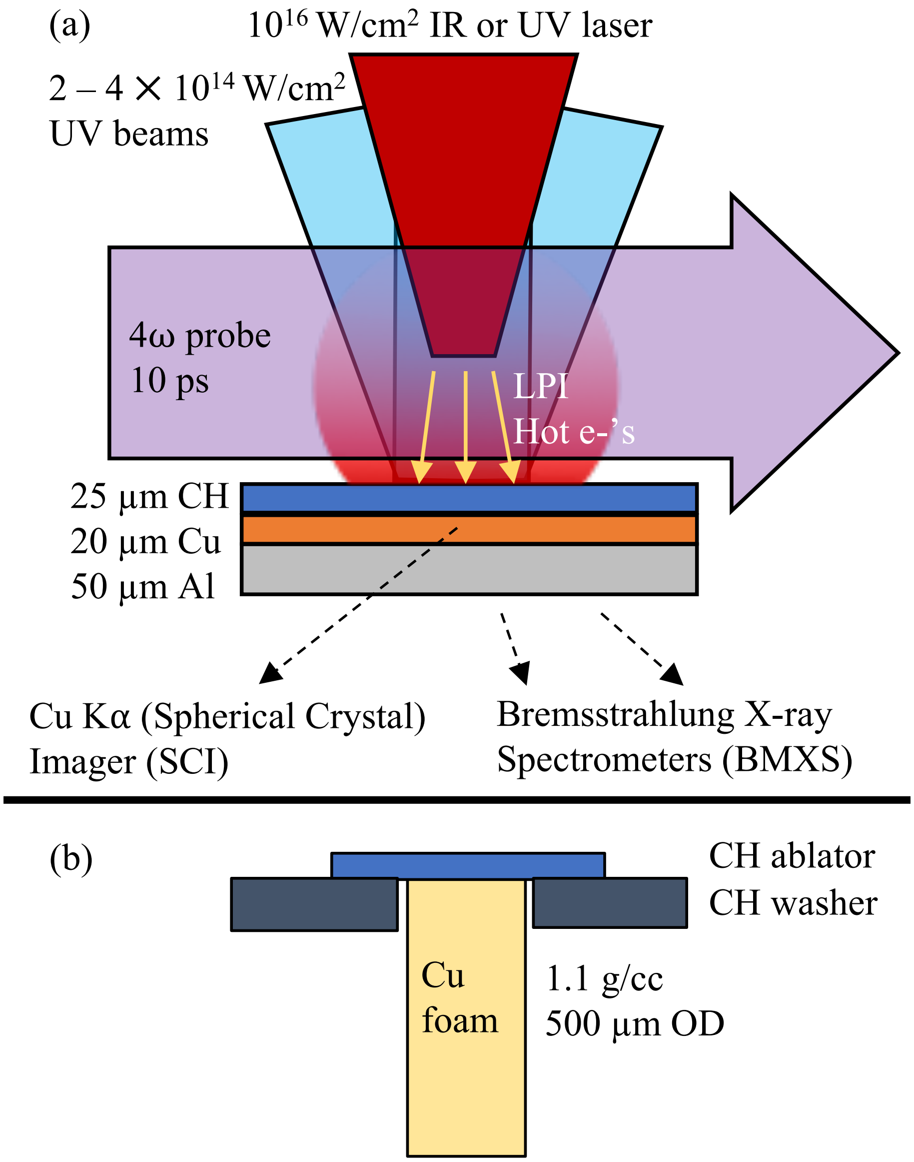

Figure 6.1: Experimental Setup and the 2 type of targets used to characterize hot electrons from 10^{16} W/cm^2 IR and UV lasers in hot and large plasmas. (a) is the setup with the 3-layer 5 mm diameter disk as our primary target; (b) is the secondary target, a Cu foam cylinder is attached on a 25 μm CH ablator to visualize the hot electron spatial energy deposition.

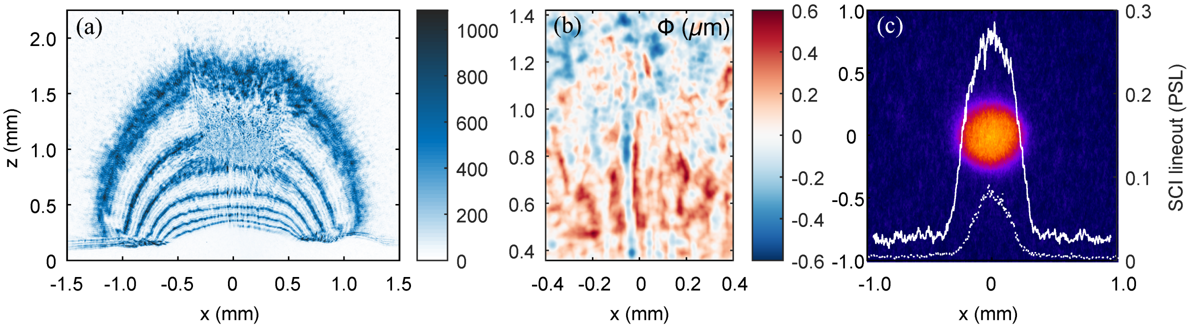

Figure 6.2: Probe and Cu Kα images from the shot with 100 ps IR laser. z is the distance from the target original surface. (a) 4ω Angular Filtration Refractometry (AFR) image, which was taken 60 ps after the IR laser power peak; (b) probe beam deflection potential as Eq. (6.1), inverted from the shadowgraphy image [120], zoomed into the region of interaction and filamentation; (c) the Cu Kα image and the lineouts cross the center; solid line is from the IR shot, the dotted line is the background shot with only UV plasma creation beams (6.4 kJ, 3×10^{14} W/cm^2).

Filter Refractometry (AFR) data [116, 126]. The 200 ps IR beam experiments used a 1.0 kJ and a 1.3 kJ 100 ps pulse that were overlapped in space but stacked sequentially in time. Limited by the facility, the shortest UV pulse is 1ns with 1.25 kJ energy. As seen in Fig. 6.1(a), a 5 mm diameter 3-layer disk target is used as the primary target in our experiments. The buried Cu serves as a tracer layer for hot electrons as they produce fluoresced Cu Ka line emission that we image with a spherical crystal imager (SCI) [109]. The distribution of the observed Kα emission gives a bound for the electron beam divergence. The Al layer that tamps the Cu layer can further stop the hot electrons and inhibit the electron refluxing. In order to image the penetration of the hot electrons and quantify their preheat in front of the shock, some of UV interaction shots use a target with 1.1 g/cm^3 Cu foam cylinder attached on the rear side of the ablator, shown in Fig. 6.1(b). In all shots, the Bremsstrahlung spectra in the range of 17 keV to 185 keV are diagnosed by the first 8 image plates in Bremsstrahlung MeV X-ray Spectrometers (BMXS) [69] from two different target lines of sight. The density profile of laser–plasma interaction is captured by AFR and shadowgraphy with the use of a 4ω probe laser. The orientation of this probe can be seen in the experimental configuration cartoon of Fig 6.1(a).

Table 6.1: Plasma and laser parameters in the experiments, the generated hot electron temperature, and the energy conversion efficiency from laser to hot electrons. T_e and L_n are from FLASH simulations at the time in the middle of the interaction lasers. I_L is the vacuum intensity at quarter critical surface. $I_\mathrm{L,AFR}$ is the sprayed beam intensity considering the AFR measured spot size on $n_\mathrm{c}/4$.

	200 ps IRs	100 ps IR	1 ns UV
T_e (keV)	1.5	1.4	1.5
L_n (μm)	360	450	300
I_L (W/cm^2)	2.0×10^{16}	2.0×10^{16}	1.0×10^{16}
$I_\mathrm{L,AFR}$ (W/cm^2)	2.3×10^{15}	5.6×10^{15}	1.0×10^{16}
$I_\mathrm{L,AFR}\lambda^2$ (W cm^{-2}μm^2)	2.5×10^{15}	6.2×10^{15}	1.1×10^{15}
T_hot (keV)	70 ± 8	90 ± 10	45 ± 5
$E_\mathrm{hot}/E_\mathrm{L}$	$3.5 \pm 0.7\%$	$2.4 \pm 0.5\%$	$2.0 \pm 0.4\%$
Average Divergence	$< 11°$	$< 11°$	$< 22°$

6.3 Hot electron temperature and energy

The bremsstrahlung spectra show that both IR and UV lasers produce hot electrons with moderate temperatures ($45 - 90$ keV) and high energy conversion efficiency $2.0 - 3.5\%$, as seen in Table 6.1. The hot electron temperature and the total energy were inferred by fitting the simulated bremsstrahlung x-ray spectra to the diagnosed spectra from two BMXSs. We used Monte Carlo code ITS 3.0 [70] to simulate both the target x-ray emission and the x-ray doses on image plates in BMXSs. In these simulations, the electron beams were assumed to be collimated and have a 1-D relativistic Maxwell–Jüttner distribution. The 200 ps IR pulse performed better than the 100 ps IR pulse in generating the hot electrons for electron shock ignition, since the lower T_hot and higher $E_\mathrm{hot}/E_\mathrm{L}$ are preferred [48]. The lowering of T_hot from 90 keV to 70 keV would reduce the hot electron stopping range in the DT fuel from 49 mg/cm^2 to 30 mg/cm^2 and consequently reduce the required beam energy. Compared to the IR lasers, the high intensity UV generated hot electrons with even lower temperature (45 ± 5 keV) but lower energy conversion efficiency ($2.0 \pm 0.4\%$). These lower T_h and $E_\mathrm{h}/E_\mathrm{L}$ are expected since the UV laser has a lower

$I_L\lambda^2 \sim 1.1 \times 10^{15}$ Wcm^{-2}μm^2, which is only 18% – 44% of the $I_L\lambda^2$ in IR, see Table 6.1. Although the UV energy coupling is not as high as IR, the lower T_{hot} in UV can short the required pulse length for the shock generation. The required laser powers and pulse durations for the shock formation will be discussed later in this chapter.

6.4 Hot electron beam divergence

The AFR and Cu Kα images show that all the hot electron beams from either IR or UV lasers are collimated. The AFR image from the 100 ps IR shot, as seen in Fig. 6.2(a), shows a plasma perturbation region at ~1 mm above the target surface, which agrees with the SRS's location. This strong SRS suggests that it can be the main mechanism for the hot electron generation. From Fig. 6.2(c), Cu Kα emission is concentrated in a spot with 470 ± 10 μm FWHM, which is 30% smaller than the diameter of the perturbation region. A similar sized perturbation region and Cu Kα spot were also observed in the 200 ps IR experiments. Similarly, the UV's Cu Kα spot size (fig. 6.3(b), FWHM = 100 ± 10 μm) is also approximately equal to the laser's focal spot size. If we consider the distance from the perturbation region to the target, 1 mm in IR shots and 300 μm in UV shots, only well collimated beams can produce these small Cu Kα spots. This beam collimation also agrees with the direction of the plasma waves in SRS.

This small beam divergence also suggests that most of the electrons generated by the UV and IR lasers can be collected by the compressed fuel in electron shock ignition. As seen in the SCI image from the IR shot, Fig. 6.2(c), 95% of the Cu Kα signal is concentrated in a 280 μm radius spot, smaller than the 350 μm radius of the compressed fuel during the spike pulse [36]. It suggests that the compressed capsule can collect >95% of the hot electrons. For the UV shot, 95% Cu Kα signal is concentrated in a 200 μm radius spot. The average divergence angle of the electron beam is 22° when we assume electron beam is from a point source at the UV $n_c/4$ ($z = 250$ μm). With this small divergence, minimum 84% of the hot electrons generated at UV $n_c/4$ surface ($r_{nc/4} = 900$ μm) can be collected by the compressed target.

6.5 Observed laser filamentation

Besides the observed SRS, the IR laser also sprayed into filaments during the interaction. The AFR image Fig. 6.2(a) shows that the width of the plasma perturbation region is 2.2 times as large as the vacuum IR spot size (300 μm) at $n_c/4$. This wider interaction region is likely due to the laser filamentation in the low density plasma. The laser power in one speckle (P_s) is 4 GW, 24 times as high as the filamentation critical power P_c [95, 149], which is 165 MW at $n_c/4$ where $T_e \sim 1.4$ keV. Similar to our experiment, a 4 times enlarged laser spot was found in previous shock ignition relevant experiment where $P_s/P_c \sim 23$ [79]. This beam spraying would reduce the average IR intensity at $n_c/4$ from 2.0×10^{16} W/cm^2 to 5.6×10^{15} W/cm^2 as shown in Table 6.1 and affect the LPIs. The reduced intensity is considered in our PIC simulations. In addition to this AFR image, the 4ω shadowgraphy captured the laser filamentation in the $n_e > n_c/4$ region. Fig. 6.2(b) shows the deflection potential map inverted from the shadowgraphy image. The deflection potential Φ can be expressed as

$$\Phi \approx \frac{e^2}{m_e \epsilon_0 \omega_p^2} \int n_e(x, y, z) \mathrm{d}z, \tag{6.1}$$

where ω_p is the probe beam angular frequency and z axis is along the direction of the probe beam. This shadowgraphy inverse process is based on Ref. [120, 122]. The deflection potential map shows several plasma channels along the laser direction. These channels are 50 μm wide on average with a typical density depth δn_e on the order of 10^{20} cm^{-3}. This density depth implies that the laser intensities in the channels are $2-6 \times 10^{15}$ W/cm^2

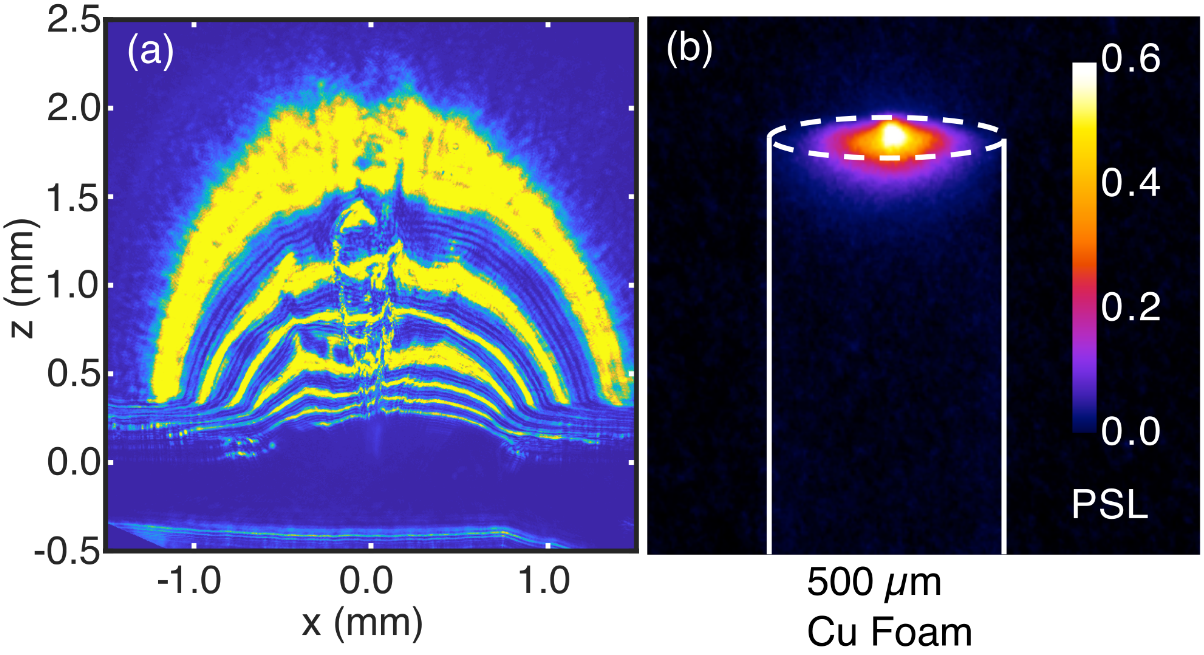

Figure 6.3: The results of the UV interaction experiments: (a) AFR image captured after the interaction of the high intensity UV laser; (b) Cu Kα image of the Cu foam target. White lines mark the target profile.

higher than that out of the channels [95], which are on the same order of the sprayed beam intensities ($I_{\mathrm{L,AFR}}$'s in Table 6.1).

In contrast to the laser spraying in IR shot, the AFR image of the UV interaction shot, as shown in Fig. 6.3(a), shows that the UV laser created a single straight channel in the plasma. This may be explained by the weaker ponderomotive force of the UV laser which can mitigate the self-trapping effect. In the UV experiment, the laser speckle power at $n_c/10$ is ~1 GW, and the $P_{\mathrm{s}}/P_{\mathrm{c}}$ is about 2, which is much lower than the ratio in the IR case. Inside the channel, the plasma was perturbed from $n_{\mathrm{c}}/100$ ($z = 1.4$ mm) to $n_{\mathrm{c}}/4$ ($z =$ 0.25 mm) region. This density perturbation suggests that, with large scale corona, LPIs can happen in much lower density region than that shown in reduced-scale experiments, in which only SRS from $n_{\mathrm{e}} > n_{\mathrm{c}}/10$ region was detected [46].

6.6 PIC simulations

We used 2D PIC code OSIRIS [150] to model the laser–plasma instabilities and hot electron generation in the experiments. Simulations were performed with both IR and UV beams in the time scale of 6-8 ps, and the initial physical parameters were obtained from FLASH hydro simulations. For the simulation with IR beam, the exponential density profile ranges from $0.1-0.3$ n_c with a scale length of ~ 380 μm. The electron and ion temperatures are 1.2 and 0.28 keV, respectively. For the simulation with the UV beam, the plasma density is between 0.14 and 0.28 n_c with an exponential profile and scale length of ~ 230 μm at $n_c/4$ surface. The electron and ion temperatures are 1.6 and 1 keV. The incident lasers are plane waves for both simulations with intensity $I = 1 \times 10^{16}$ W/cm^2 for IR and $I = 5 \times 10^{15}$ W/cm^2 for UV. In the simulations, we diagnose the space and time evolution of the LPI modes, and the hot electrons from both inside the simulation domain and crossing the boundaries.

In both simulations, TPD occurs only transiently near the $n_c/4$ surface and is rapidly suppressed by strong pump depletion due to SRS and SBS in the region with density below $0.2n_c$. In the UV simulation, TPD generates a negligible amount of hot electrons. In the IR simulation, the hot electrons generated by TPD and SRS have different divergence angles. Figure 6.4(a) shows typical angular distributions of the hot electrons (with energy above 50 keV) from only SRS and from both TPD and SRS. The hot electron angles are significantly different between $FWHM = 38°$ for only SRS and $FWHM = 70°$ when hot electrons generated by TPD were mixed with those from SRS. This shows a much larger divergence angle of hot electrons from TPD compared to those from SRS, as a result of their respective dispersion relations. The TPD modes grow mainly on the TPD hyperbola in the wave vector space [18] and can have high transverse wave vector with deviation angles of $\sim 45°$ to the laser wave vector. By comparison, the SRS modes with highest growth rates are directly backscattered SRS along the laser incidence direction.

Therefore, the hot electrons generated by these oblique TPD modes have a much larger angle than those accelerated by directional SRS modes.

The accumulated angular and energy distributions of the hot electrons are shown in Fig. 6.4(b). Both the UV and the IR simulations show similar angular spread with FWHM$\sim 60^\circ$ and with average angle $\sim 22^\circ$, which approximately agree with the experimental results. The similarity between the two simulations agrees with the experimental results that the hot electrons from both UV and IR experiments show similar collimated feature. The hot electron energy spectra are demonstrated in Fig. 6.4(c). The spectra from both IR and UV have two-temperature feature with low-energy temperature of ~ 35 keV and high-energy temperatures of ~ 85 keV for UV and 144 keV for IR. This qualitatively agrees with the higher average hot electron temperature for IR. From these results, we think that the hot electron generation mechanism in our experiment is mainly SRS.

6.7 Discussion and conclusion

With the measured T_{hot}'s and $E_{\mathrm{hot}}/E_{\mathrm{L}}$'s, either IR or UV can generate the hot electron beam intense enough to create a 300 Mbar ignition shock for electron shock ignition. The calculations in Ref. [48, 49] indicate that stopping a hot electron beam in the compressed DT fuel can generate a shock with pressure P_{h} in loading time t_{h} as

$$P_{\mathrm{h}} \sim 175\, I_0^{2/3} \rho_0^{1/3}\ \mathrm{Mbar}, \tag{6.2}$$

$$t_{\mathrm{h}} \sim 0.11\, R_0\, I_0^{-1/3}\, \rho_0^{-2/3}\ \mathrm{ns}, \tag{6.3}$$

where I_0 is the electron beam intensity in 10^{15} W/cm^2, ρ_0 is the averaged compressed shell density in g/cm^3, and R_0 is the electron stopping range in mg/cm^2. This analytical model suggests that generating a 300 Mbar shock in a 10 g/cm^3 DT fuel would require

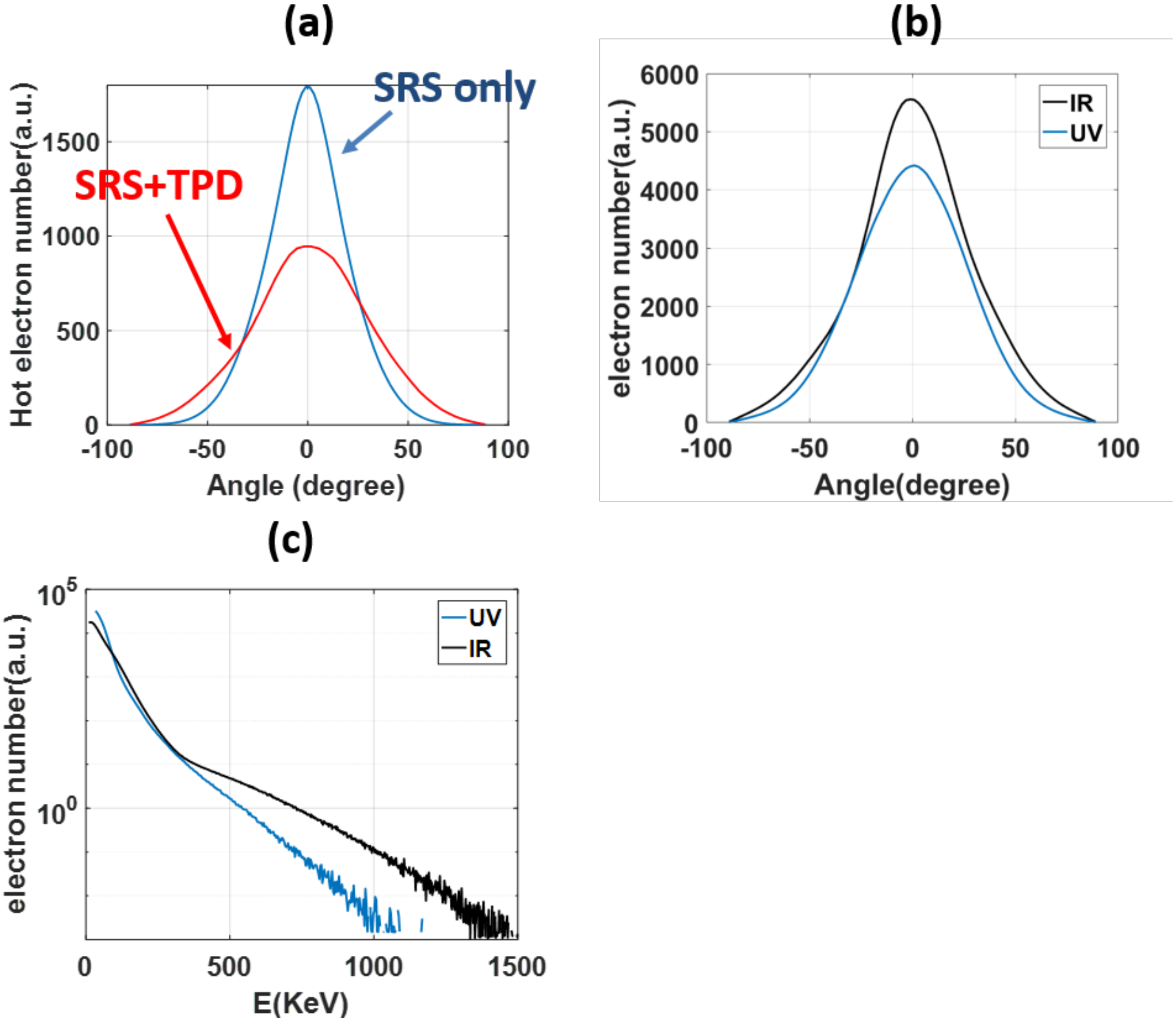

Figure 6.4: (a) The angular distribution of hot electrons from IR simulation inside the simulation box at 1ps (Blue) when SRS is the only LPI, and recorded at the simulation boundary during 0.05 ps near 3.65 ps (Red), when hot electrons from TPD ans SRS are mixed together. (b) The accumulated angular distributions and energy spectra of the hot electrons for UV (blue) and IR(black) simulations.

a 7×10^{14} W/cm^2 electron beam on the dense shell. This electron beam needs to have a 11 TW total power in the shock ignition design for HiPER [36], in which the shell was designed be compressed to $r_s = 350$ μm before launching the ignition shock. According to the measured E_h/E_L's, to generate this electron beam requires a minimum 540 TW UV pulse or a 310 TW IR pulse. We can also calculate the required laser pulse lengths with Eq. (6.3). For $T_h \sim 70$ keV IR hot electrons, the average stopping range R_0 is ~ 30 mg/cm^2 in DT fuel. The required electron beam pulse duration is 0.8 ns. For $T_h \sim 45$ keV UV-induced hot electron beams, $R_0 \sim 12$ mg/cm^2, the required pulse duration is 0.3 ns. Based on the required laser power discussed above, total 250 kJ of IR energy or 160 kJ of UV energy are required in the spike pulse.

For electron shock ignition with IR lasers, further experiments with nanosecond IR lasers are necessary, since our experiments have shown that the pulse duration can affect the hot electron properties. This effect is also observed in some PIC simulations showing that density perturbations can suppress LPIs [151]. As shown in the AFR and the shadowgraphy images, Fig. 6.2(a) and (b), the first 100 ps IR pulse has heavily disturbed the plasma. Consequently, the plasma conditions for the LPIs in the remaining pulse would be different to those in the first 100 ps. The comparison between the 100 ps and the 200 ps pulses has partially shown the effect, but a nanosecond pulse may further impact the hot electron generation, which is needed to be experimentally studied.

In conclusion, our experimental hot electron characterization suggests both IR and UV lasers can generate electron beams capable to launch a 300 Mbar shock for electron shock ignition. These hot electrons are generated by 10^{16} W/cm^2 lasers in large and hot plasmas under shock ignition conditions. The hot electrons from IR lasers have a higher temperature (~ 70 keV) and higher energy conversion efficiency (~ 3.5%) than hot electrons produced by UV lasers (45 keV, 2.0%). Both hot electron beams have small divergence, and the PIC simulations suggest they are SRS-generated. Theoretical analyses suggest that high shock pressure in electron shock ignition can be achieved by the hot electron beams generated from 540 TW UV or 310 TW IR lasers, which are around or below the limit power of NIF.

This chapter is currently being prepared for submission and publication: "Generation of Collimated Moderate Temperature Electron Beam and Laser–Plasma Interaction for Megajoule Shock Ignition", S. Zhang, C. M. Krauland, J. Li, J. Peebles, F. N. Beg, S. Muller, N. Alexander, C. Ren, W. Theobald, R. Betti, D. Haberberger, E. M. Campbell, R. Yan, E. Borwick, J. Trela, D. Batani, P. Nicolai, and M. S. Wei. The dissertation's author is the primary investigator and author of this paper.

Chapter 7

Summary and future work

7.1 Summary

As an alternative inertial confinement fusion scheme, shock ignition is designed to use a >300 Mbar convergent shock to ignite a pre-compressed fuel capsule. Generating this strong convergent shock requires the energy deposited by 10^{16} W/cm^2 lasers with a sub-nanosecond pulse. The energy conversion can be affected by the laser-plasma instabilities (LPIs). Thus, the validation of shock ignition requires experiments to characterize the energy deposition of the ~10^{16} W/cm^2 lasers in a large-scale and hot coronal plasma. This dissertation summarized the first series of experiments for characterizing the shock ignition-relevant LPIs. These experiments measured the LPI-induced pump-depletion and the hot electrons. These hot electrons may benefit the shock generation.

The experiments with UV lasers conducted on the OMEGA EP laser facility have for the first time demonstrated that such instabilities can ~100% deplete the first 0.5 ns of the high-intensity laser. Analyses of the observed laser-generated blast wave suggest that this pump-depletion starts at ~0.02 critical density and progresses to 0.1–0.2 critical density, which is also confirmed by the time-resolved stimulated Raman backscattering spectra. The pump-depletion dynamics can be explained by the breaking of ion-acoustic waves in stimulated Brillouin scattering. Such pump-depletion would inhibit the collisional laser energy absorption but may benefit the generation of hot electrons with moderate temperatures for electron shock ignition [50].

The experiments on the OMEGA EP laser facility have also characterized the temperature and total energy of hot electrons generated from a kilojoule-class 100-ps infrared (IR) or a 1-ns ultraviolet (UV) laser interacting with a large ($L_n \sim 330 - 450$ µm) and hot ($T_\mathrm{e} \sim 1 - 2$ keV) coronal plasma at the SI-relevant intensities ($\sim 10^{16}$ W/cm^2). The IR laser converts ~2.5% energy into hot electrons with $T_\mathrm{hot} \sim$ 60–90 keV, while the UV laser couples $0.8 \pm 0.7\%$ energy into $T_\mathrm{hot} = 27 \pm 9$ keV hot electrons. The IR-produced hot electrons yield 5 times higher Cu Kα emission than the UV case, confirming the higher electron conversion efficiency with the IR laser. The low energy conversion from the UV laser to hot electrons may be due to the refraction of the off-normal incident laser in the large coronal plasma. These findings are the first comparisons of hot electron generation between the IR and UV pulses at kilojoule scales in SI-relevant large-scale plasmas. The findings may expand the SI design space to include IR lasers as the possible spike lasers.

Simulations predict that laser–plasma-instability-induced hot electrons may be able to generate the strong shock required in the shock ignition concept [50]. This depends on the electron population and temperature produced during the laser pulse. The planar experiments described in this dissertation show that the interaction between the $\sim 10^{16}$ W/cm^2 IR or UV lasers and the large-scale plasmas generates collimated electron beams with moderate temperature ($45 - 90$ keV). Particle-in-Cell simulations suggest these collimated hot electrons are generated mainly by stimulated Raman scattering. This is consistent with the SRS-induced plasma perturbations observed in the experimental data. The filamentation of the plasma-creation UV lasers may also create azimuthal magnetic fields guiding the electrons. Based on these results, theoretical calculations suggest that the required 300 Mbar shock can be created by the hot electrons from 310 TW, 0.8 ns infrared lasers or 540 TW, 0.3 ns ultraviolet lasers. These laser parameters are around the limits of National Ignition Facility.

7.2 Future work

The generation of the 300-Mbar shock in full-scale conditions still needs to be validated. The experiment has been scheduled in September 2020 to measure the speed of the shock generated by overlapped UV lasers. The overlapped laser intensity is 1.5×10^{16} W/cm^2. The lasers are focused 200 μm above the target surface to have a larger spot size (~1 mm) for a larger plasma length scale while keeping the high intensity region near the quarter critical surface. The length scale of the plasma is 220 μm, and the plasma temperature is 3–4 keV. A larger plasma can be created if a conical target is used. Experiments on the NIF laser would also provide a direct measurement of the shock strength.

The >100 keV portion of the hot electrons also needs to be characterized since they may preheat the fuel. The experiments are planned to use a thicker CH ablator (140 μm) to stop the low-energy (<100 keV) hot electrons from reaching the Cu layer. By comparing the Cu Kα generated in this target to that from the 25 μm CH target, we would be able to quantify the >100 keV portion of the hot electrons.

In addition, the magnetic field generated around the electron beam may also affect the electron stopping, which is not considered in the analyses of the experiments. The current of the electron beam is on the order of 10 MA, which is far above the Alfven current limit of ~ 17 kA. The rise of the beam current would create an electric field along the beam driving the return current to neutralize the beam current. However, the electric field also creates the azimuthal magnetic field, which may grow to kT after a few hundreds of ps. The field magnitude is large enough to magnetize the hot electrons near the edge of the beam. Consequently, the field may pinch the electron beam or create filaments. This field-effect can be simulated with a hybrid or implicit PIC code.

The theoretical analysis of the ion-acoustic wave breaking model discussed in Ch. 4 also needs simulations or experiments for validation. The regular PIC simulations are not suitable to describe this nanosecond scale dynamic. However, a hybrid PIC code [136] with a fluid electron model and a pondermotive force model or a PIC code with reduced ion mass may be useful to simulate the SBS saturation properly. If these simulations can reproduce the observed dynamic pump-depletion, then it can be extended to simulate the pump-depletion in a higher-temperature plasma which is closer to a full-scale shock ignition condition.

Bibliography

[1] Vaclav Smil. *Energy and Civilization*. The MIT Press, 2017. ISBN: 9780262338301. DOI: 10.7551/mitpress/10752.001.0001. URL: https://mitpress.mit.edu/books/energy-and-civilization.

[2] Melinda A. Zeder. “The Origins of Agriculture in the Near East”. In: *Current Anthropology* 52.S4 (2011), S221–S235. DOI: 10.1086/659307. eprint: https://doi.org/10.1086/659307. URL: https://doi.org/10.1086/659307.

[3] Dieter Lüthi et al. “High-resolution carbon dioxide concentration record 650,000–800,000 years before present”. In: *Nature* 453.7193 (May 2008), pp. 379–382. ISSN: 0028-0836. DOI: 10.1038/nature06949. URL: http://www.nature.com/articles/nature06949.

[4] Kirk W Thoning, Pieter P Tans, and Walter D Komhyr. “Atmospheric carbon dioxide at Mauna Loa Observatory: 2. Analysis of the NOAA GMCC data, 1974–1985”. In: *Journal of Geophysical Research: Atmospheres* 94.D6 (1989), pp. 8549–8565.

[5] *Climate Change: How Do We Know?* https://climate.nasa.gov/evidence/. Accessed: 2020-04-08.

[6] J. Hatfield et al. *Ch. 6: Agriculture. Climate Change Impacts in the United States: The Third National Climate Assessment*. Tech. rep. Washington, DC: U.S. Global Change Research Program, 2014, pp. 150–174. DOI: 10.7930/J02Z13FR. URL: https://nca2014.globalchange.gov/downloads.

[7] *Power Blows Past $9,000 Cap in Texas as Heat Triggers Emergency*. https://www.bloomberg.com/news/articles/2019-08-13/texas-power-prices-briefly-surpass-9-000-amid-searing-heat. Accessed: 2020-04-08.

[8] Albert E Heustis. *PEACEFUL USES OF ATOMIC ENERGY: PROCEEDINGS OF THE SECOND UNITED NATIONS INTERNATIONAL CONFERENCE*. 1960.

[9] *NuDat 2, developed by National Nuclear Data Center in Brookhaven National Laboratory*. https://www.nndc.bnl.gov/nudat2/. Accessed: 2020-04-12.

[10] Christian Iliadis. *Nuclear physics of stars*. 2nd ed. John Wiley & Sons, 2015, pp. 353–369.

[11] Stefano Atzeni and Jürgen Meyer-ter-Vehn. *The Physics of Inertial Fusion: Beam Plasma Interaction, Hydrodynamics, Hot Dense Matter*. Oxford University Press, 2009. ISBN: 9780199568017. URL: https://global.oup.com/academic/product/the-physics-of-inertial-fusion-9780199568017?cc=us&lang=en&.

[12] J D Lawson. "Some Criteria for a Power Producing Thermonuclear Reactor". In: *Proceedings of the Physical Society. Section B* 70.1 (Jan. 1957), pp. 6–10. DOI: 10.1088/0370-1301/70/1/303. URL: https://doi.org/10.1088%5C%2F0370-1301%5C%2F70%5C%2F1%5C%2F303.

[13] L. Spitzer. *Physics of Fully Ionized Gases: Second Revised Edition*. Dover Publications, 2006, p. 149. ISBN: 9780486449821.

[14] R. Betti et al. "Shock Ignition of Thermonuclear Fuel with High Areal Density". In: *Phys. Rev. Lett.* 98 (15 Apr. 2007), p. 155001. DOI: 10.1103/PhysRevLett.98.155001. URL: https://link.aps.org/doi/10.1103/PhysRevLett.98.155001.

[15] R. S. Craxton et al. *Figure 2-1 in Direct-drive inertial confinement fusion: A review*. Reprinted with permission from AIP Publishing. 2015. DOI: 10.1063/1.4934714. eprint: https://doi.org/10.1063/1.4934714. URL: https://doi.org/10.1063/1.4934714.

[16] Mordecai D. Rosen. "The physics issues that determine inertial confinement fusion target gain and driver requirements: A tutorial". In: *Physics of Plasmas* 6.5 (1999), pp. 1690–1699. DOI: 10.1063/1.873427. eprint: https://doi.org/10.1063/1.873427. URL: https://doi.org/10.1063/1.873427.

[17] M.C Herrmann, M Tabak, and J.D Lindl. "A generalized scaling law for the ignition energy of inertial confinement fusion capsules". In: *Nuclear Fusion* 41.1 (Jan. 2001), pp. 99–111. DOI: 10.1088/0029-5515/41/1/308. URL: https://doi.org/10.1088%5C%2F0029-5515%5C%2F41%5C%2F1%5C%2F308.

[18] W.L. Kruer. *The Physics of Laser Plasma Interactions*. Frontiers in physics. Westview Press, 2003. ISBN: 9780813340838. URL: https://westviewpress.com/books/physics-of-laser-plasma-interactions/.

[19] John D. Lindl et al. "The physics basis for ignition using indirect-drive targets on the National Ignition Facility". In: *Physics of Plasmas* 11.2 (2004), pp. 339–491. DOI: 10.1063/1.1578638. eprint: https://doi.org/10.1063/1.1578638. URL: https://doi.org/10.1063/1.1578638.

[20] B A Hammel et al. "Simulations and experiments of the growth of the tent perturbation in NIF ignition implosions". In: *Journal of Physics: Conference Series* 717.1 (2016), p. 012021. URL: http://stacks.iop.org/1742-6596/717/i=1/a=012021.

[21] Stefano Atzeni. "Inertial fusion fast ignitor: Igniting pulse parameter window vs the penetration depth of the heating particles and the density of the precompressed fuel". In: *Physics of Plasmas* 6.8 (1999), pp. 3316–3326. DOI: 10.1063/1.873571. eprint: https://doi.org/10.1063/1.873571. URL: https://doi.org/10.1063/1.873571.

[22] R Betti et al. "Shock ignition of thermonuclear fuel with high areal densities". In: *Journal of Physics: Conference Series* 112.2 (2008), p. 022024. URL: http://stacks.iop.org/1742-6596/112/i=2/a=022024.

[23] S. Atzeni et al. "Shock ignition of thermonuclear fuel: principles and modelling". In: *Nuclear Fusion* 54.5 (2014), p. 054008. URL: http://stacks.iop.org/0029-5515/54/i=5/a=054008.

[24] L. J. Perkins et al. "Shock Ignition: A New Approach to High Gain Inertial Confinement Fusion on the National Ignition Facility". In: *Phys. Rev. Lett.* 103 (4 July 2009), p. 045004. DOI: 10.1103/PhysRevLett.103.045004. URL: https://link.aps.org/doi/10.1103/PhysRevLett.103.045004.

[25] K. S. Anderson et al. "A polar-drive shock-ignition design for the National Ignition Facility". In: *Physics of Plasmas* 20.5 (2013), p. 056312. DOI: 10.1063/1.4804635. URL: http://dx.doi.org/10.1063/1.4804635.

[26] B Canaud and M Temporal. "High-gain shock ignition of direct-drive ICF targets for the Laser Megajoule". In: *New Journal of Physics* 12.4 (2010), p. 043037. URL: http://stacks.iop.org/1367-2630/12/i=4/a=043037.

[27] X Ribeyre et al. "Shock ignition: an alternative scheme for HiPER". In: *Plasma Physics and Controlled Fusion* 51.1 (2008), p. 015013. URL: http://stacks.iop.org/0741-3335/51/i=1/a=015013.

[28] X Ribeyre et al. "Shock ignition: modelling and target design robustness". In: *Plasma Physics and Controlled Fusion* 51.12 (2009), p. 124030. URL: http://stacks.iop.org/0741-3335/51/i=12/a=124030.

[29] Stefano Atzeni. *Figure 10.18 in Laser-Plasma Interactions and Applications*. Ed. by Paul McKenna et al. Reprinted with permission from Springer International Publishing. 2013.

[30] M. Lafon, X. Ribeyre, and G. Schurtz. "Gain curves and hydrodynamic modeling for shock ignition". In: *Physics of Plasmas* 17.5 (2010), p. 052704. DOI: 10.1063/1.

3407623. eprint: https://doi.org/10.1063/1.3407623. URL: https://doi.org/10.1063/1.3407623.

[31] C.E. Max, J.D. Lindl, and W.C. Mead. “Effect of symmetry requirements on the wavelength scaling of directly driven laser fusion implosions”. In: *Nuclear Fusion* 23.2 (Feb. 1983), pp. 131–145. DOI: 10.1088/0029-5515/23/2/001. URL: https://doi.org/10.1088%5C%2F0029-5515%5C%2F23%5C%2F2%5C%2F001.

[32] W Theobald et al. “Initial experiments on the shock-ignition inertial confinement fusion concepta)”. In: *Physics of Plasmas (1994-present)* 15.5 (2008), p. 056306.

[33] O. Klimo et al. “Laser plasma interaction studies in the context of shock ignition–Transition from collisional to collisionless absorption”. In: *Physics of Plasmas* 18.8 (Aug. 2011), p. 082709. ISSN: 1070-664X. DOI: 10.1063/1.3625264. URL: http://aip.scitation.org/doi/10.1063/1.3625264.

[34] O. Klimo and V T Tikhonchuk. “Laserplasma interaction studies in the context of shock ignition: the regime dominated by parametric instabilities”. In: *Plasma Physics and Controlled Fusion* 55.9 (Sept. 2013), p. 095002. ISSN: 0741-3335. DOI: 10.1088/0741-3335/55/9/095002. URL: http://stacks.iop.org/0741-3335/55/i=9/a=095002?key=crossref.3589d6a562fb6ff9d7e525c31803a0e7%20http://stacks.iop.org/0741-3335/55/i=9/a=095002.

[35] L. Hao et al. “Simulation of stimulated Brillouin scattering and stimulated Raman scattering in shock ignition”. In: *Physics of Plasmas* 23.4 (2016), p. 042702. DOI: 10.1063/1.4945647. URL: http://dx.doi.org/10.1063/1.4945647.

[36] D. Batani et al. “Physics issues for shock ignition”. In: *Nuclear Fusion* 54.5 (2014), p. 054009. URL: http://stacks.iop.org/0029-5515/54/i=5/a=054009.

[37] D. W. Forslund, J. M. Kindel, and E. L. Lindman. “Theory of stimulated scattering processes in laserirradiated plasmas”. In: *The Physics of Fluids* 18.8 (1975), pp. 1002–1016. DOI: 10.1063/1.861248. eprint: https://aip.scitation.org/doi/pdf/10.1063/1.861248. URL: https://aip.scitation.org/doi/abs/10.1063/1.861248.

[38] C. S. Liu, Marshall N. Rosenbluth, and Roscoe B. White. “Raman and Brillouin scattering of electromagnetic waves in inhomogeneous plasmas”. In: *The Physics of Fluids* 17.6 (1974), pp. 1211–1219. DOI: 10.1063/1.1694867. URL: http://aip.scitation.org/doi/abs/10.1063/1.1694867.

[39] A. Simon et al. “On the inhomogeneous two-plasmon instability”. In: *The Physics of Fluids* 26.10 (1983), pp. 3107–3118. DOI: 10.1063/1.864037. URL: http://aip.scitation.org/doi/abs/10.1063/1.864037.

[40] S. D. Baton et al. “Shock generation comparison with planar and hemispherical targets in shock ignition relevant experiment”. In: *Physics of Plasmas* 24.9 (Sept. 2017), p. 092708. ISSN: 1070-664X. DOI: 10.1063/1.4989525. URL: http://aip.scitation.org/doi/10.1063/1.4989525.

[41] M Hohenberger et al. “Shock-ignition relevant experiments with planar targets on OMEGA”. In: *Physics of Plasmas (1994-present)* 21.2 (2014), p. 022702.

[42] D. Batani et al. “Generation of high pressure shocks relevant to the shock-ignition intensity regime”. In: *Physics of Plasmas* 21.3 (2014), p. 032710. DOI: 10.1063/1.4869715. eprint: https://doi.org/10.1063/1.4869715. URL: https://doi.org/10.1063/1.4869715.

[43] S.Yu. Gus’kov et al. “Laser-driven ablation through fast electrons in PALS experiment”. In: *Journal of Physics: Conference Series* 688 (Mar. 2016), p. 012023. DOI: 10.1088/1742-6596/688/1/012023. URL: https://doi.org/10.1088%5C%2F1742-6596%5C%2F688%5C%2F1%5C%2F012023.

[44] T. Pisarczyk et al. “Pre-plasma effect on laser beam energy transfer to a dense target under conditions relevant to shock ignition”. In: *Laser and Particle Beams* 33.2 (June 2015), pp. 221–236. ISSN: 0263-0346. DOI: 10.1017/S0263034615000233. URL: https://www.cambridge.org/core/product/identifier/S0263034615000233/type/journal%7B%5C_%7Darticle.

[45] R. Nora et al. “Gigabar Spherical Shock Generation on the OMEGA Laser”. In: *Phys. Rev. Lett.* 114 (4 Jan. 2015), p. 045001. DOI: 10.1103/PhysRevLett.114.045001. URL: https://link.aps.org/doi/10.1103/PhysRevLett.114.045001.

[46] W. Theobald et al. “Spherical strong-shock generation for shock-ignition inertial fusion”. In: *Physics of Plasmas* 22.5 (2015), p. 056310. DOI: 10.1063/1.4920956. URL: http://aip.scitation.org/doi/abs/10.1063/1.4920956.

[47] S. Gus’kov et al. “Ablation Pressure Driven by an Energetic Electron Beam in a Dense Plasma”. In: *Phys. Rev. Lett.* 109 (25 Dec. 2012), p. 255004. DOI: 10.1103/PhysRevLett.109.255004. URL: https://link.aps.org/doi/10.1103/PhysRevLett.109.255004.

[48] E. Llor Aisa et al. “Dense plasma heating and shock wave generation by a beam of fast electrons”. In: *Physics of Plasmas* 22.10 (2015), p. 102704. DOI: 10.1063/1.4933119. URL: https://doi.org/10.1063/1.4933119.

[49] E. Llor Aisa et al. “The preplasma effect on the properties of the shock wave driven by a fast electron beam”. In: *Physics of Plasmas* 23.8 (2016), p. 082702. DOI: 10.1063/1.4960209. URL: https://doi.org/10.1063/1.4960209.

[50] W. L. Shang et al. “Electron Shock Ignition of Inertial Fusion Targets”. In: *Phys. Rev. Lett.* 119 (19 Nov. 2017), p. 195001. DOI: 10.1103/PhysRevLett.119.195001. URL: https://link.aps.org/doi/10.1103/PhysRevLett.119.195001.

[51] R. Yan et al. “Generating energetic electrons through staged acceleration in the two-plasmon-decay instability in inertial confinement fusion”. In: *Phys. Rev. Lett.* 108 (17 Apr. 2012), p. 175002. DOI: 10.1103/PhysRevLett.108.175002. URL: https://link.aps.org/doi/10.1103/PhysRevLett.108.175002.

[52] R. Yan, J. Li, and C. Ren. “Intermittent laser-plasma interactions and hot electron generation in shock ignition”. In: *Physics of Plasmas* 21.6 (2014), p. 062705. DOI: 10.1063/1.4882682. URL: http://dx.doi.org/10.1063/1.4882682.

[53] M. Hohenberger et al. “Polar-direct-drive experiments on the National Ignition Facility”. In: *Physics of Plasmas* 22.5 (2015), p. 056308. DOI: 10.1063/1.4920958. eprint: https://aip.scitation.org/doi/pdf/10.1063/1.4920958. URL: https://aip.scitation.org/doi/abs/10.1063/1.4920958.

[54] M. J. Rosenberg et al. “Origins and Scaling of Hot-Electron Preheat in Ignition-Scale Direct-Drive Inertial Confinement Fusion Experiments”. In: *Phys. Rev. Lett.* 120 (5 Jan. 2018), p. 055001. DOI: 10.1103/PhysRevLett.120.055001. URL: https://link.aps.org/doi/10.1103/PhysRevLett.120.055001.

[55] M. J. Rosenberg et al. “Stimulated Raman scattering mechanisms and scaling behavior in planar direct-drive experiments at the National Ignition Facility”. In: *Physics of Plasmas* 27.4 (2020), p. 042705. DOI: 10.1063/1.5139226. eprint: https://doi.org/10.1063/1.5139226. URL: https://doi.org/10.1063/1.5139226.

[56] W Theobald et al. “Spherical shock-ignition experiments with the 40+ 20-beam configuration on OMEGA”. In: *Physics of Plasmas (1994-present)* 19.10 (2012), p. 102706.

[57] P Koester et al. “Recent results from experimental studies on laserplasma coupling in a shock ignition relevant regime”. In: *Plasma Physics and Controlled Fusion* 55.12 (Nov. 2013), p. 124045. DOI: 10.1088/0741-3335/55/12/124045. URL: https://doi.org/10.1088%5C%2F0741-3335%5C%2F55%5C%2F12%5C%2F124045.

[58] O Renner et al. “Suprathermal electron production in laser-irradiated Cu targets characterized by combined methods of x-ray imaging and spectroscopy”. In: *Plasma Physics and Controlled Fusion* 58.7 (2016), p. 075007. URL: http://stacks.iop.org/0741-3335/58/i=7/a=075007.

[59] D. Batani et al. “Progress in understanding the role of hot electrons for the shock ignition approach to inertial confinement fusion”. In: *Nuclear Fusion* 59.3 (Dec.

2018), p. 032012. DOI: 10.1088/1741-4326/aaf0ed. URL: https://doi.org/10.1088%5C%2F1741-4326%5C%2Faaf0ed.

[60] S. Weber and C. Riconda. “Temperature dependence of parametric instabilities in the context of the shock-ignition approach to inertial confinement fusion”. In: *High Power Laser Science and Engineering* 3 (2015). DOI: 10.1017/hpl.2014.50. URL: https://doi.org/10.1017/hpl.2014.50.

[61] C. Riconda et al. “Kinetic simulations of stimulated Raman backscattering and related processes for the shock-ignition approach to inertial confinement fusion”. In: *Physics of Plasmas* 18.9 (2011), p. 092701. DOI: 10.1063/1.3630937. URL: http://dx.doi.org/10.1063/1.3630937.

[62] O. Klimo et al. “Two-dimensional simulations of laserplasma interaction and hot electron generation in the context of shock-ignition research”. In: *Plasma Physics and Controlled Fusion* 56.5 (May 2014), p. 055010. ISSN: 0741-3335. DOI: 10.1088/0741-3335/56/5/055010. URL: http://stacks.iop.org/0741-3335/56/i=5/a=055010?key=crossref.aa51f60b6b1ab2e137f3972039a116da.

[63] S. Depierreux et al. “Effect of the Laser Wavelength on the Saturated Level of Stimulated Brillouin Scattering”. In: *Phys. Rev. Lett.* 103 (11 Sept. 2009), p. 115001. DOI: 10.1103/PhysRevLett.103.115001. URL: https://link.aps.org/doi/10.1103/PhysRevLett.103.115001.

[64] S. Depierreux et al. “Experimental investigation of the stimulated Brillouin scattering growth and saturation at 526 and 351 nm for direct drive and shock ignition”. In: *Physics of Plasmas* 19.1 (Jan. 2012), p. 012705. ISSN: 1070-664X. DOI: 10.1063/1.3677256. URL: http://aip.scitation.org/doi/10.1063/1.3677256.

[65] S. D. Baton et al. “Experiment in Planar Geometry for Shock Ignition Studies”. In: *Phys. Rev. Lett.* 108 (19 May 2012), p. 195002. DOI: 10.1103/PhysRevLett.108.195002. URL: https://link.aps.org/doi/10.1103/PhysRevLett.108.195002.

[66] C. Goyon et al. “Experimental Approach to Interaction Physics Challenges of the Shock Ignition Scheme Using Short Pulse Lasers”. In: *Phys. Rev. Lett.* 111 (23 Dec. 2013), p. 235006. DOI: 10.1103/PhysRevLett.111.235006. URL: https://link.aps.org/doi/10.1103/PhysRevLett.111.235006.

[67] G. Cristoforetti et al. “Measurements of parametric instabilities at laser intensities relevant to strong shock generation”. In: *Physics of Plasmas* 25.1 (Jan. 2018), p. 012702. ISSN: 1070-664X. DOI: 10.1063/1.5006021. URL: http://dx.doi.org/10.1063/1.5006021%20http://aip.scitation.org/doi/10.1063/1.5006021.

[68] L.J. Waxer et al. “High-Energy Petawatt Capability for the Omega Laser”. In: *Opt. Photon. News* 16.7 (July 2005), pp. 30–36. DOI: 10.1364/OPN.16.7.000030. URL: http://www.osa-opn.org/abstract.cfm?URI=opn-16-7-30.

[69] C. D. Chen et al. “A Bremsstrahlung spectrometer using k-edge and differential filters with image plate dosimeters”. In: *Review of Scientific Instruments* 79.10 (2008), 10E305. DOI: 10.1063/1.2964231. URL: http://dx.doi.org/10.1063/1.2964231.

[70] J. A. Halbleib et al. “ITS: the integrated TIGER series of electron/photon transport codes-Version 3.0”. In: *IEEE Transactions on Nuclear Science* 39.4 (Aug. 1992), pp. 1025–1030. ISSN: 0018-9499. DOI: 10.1109/23.159753.

[71] D. W. Phillion et al. “Evidence for profile steepening in laserirradiated plasmas”. In: *The Physics of Fluids* 20.11 (1977), pp. 1892–1899. DOI: 10.1063/1.861808. eprint: https://aip.scitation.org/doi/pdf/10.1063/1.861808. URL: https://aip.scitation.org/doi/abs/10.1063/1.861808.

[72] R. H. Lehmberg and J. A. Stamper. “Depolarization in laser probing of inhomogeneous magnetized plasmas”. In: *The Physics of Fluids* 21.5 (1978), pp. 814–816. DOI: 10.1063/1.862299. eprint: https://aip.scitation.org/doi/pdf/10.1063/1.862299. URL: https://aip.scitation.org/doi/abs/10.1063/1.862299.

[73] O. Willi, P. Rumsby, and S. Sartang. “Optical probe observations of nonuniformities in laser-produced plasmas”. In: *IEEE Journal of Quantum Electronics* 17.9 (1981), pp. 1909–1917.

[74] G S Sarkisov. “Simulation of laser beam propagation through an axisymmetric dense plasma”. In: *Quantum Electronics* 26.9 (Sept. 1996), pp. 799–805. DOI: 10.1070/qe1996v026n09abeh000785. URL: https://doi.org/10.1070%5C%2Fqe1996v026n09abeh000785.

[75] John Dawson and Carl Oberman. “HighFrequency Conductivity and the Emission and Absorption Coefficients of a Fully Ionized Plasma”. In: *The Physics of Fluids* 5.5 (1962), pp. 517–524. DOI: 10.1063/1.1706652. eprint: https://aip.scitation.org/doi/pdf/10.1063/1.1706652. URL: https://aip.scitation.org/doi/abs/10.1063/1.1706652.

[76] John M. Dawson. “On the Production of Plasma by Giant Pulse Lasers”. In: *The Physics of Fluids* 7.7 (1964), pp. 981–987. DOI: 10.1063/1.1711346. eprint: https://aip.scitation.org/doi/pdf/10.1063/1.1711346. URL: https://aip.scitation.org/doi/abs/10.1063/1.1711346.

[77] Tudor Wyatt Johnston and John M. Dawson. “Correct values for highfrequency power absorption by inverse bremsstrahlung in plasmas”. In: *The Physics of Fluids* 16.5 (1973), pp. 722–722. DOI: 10.1063/1.1694419. eprint: https://aip.scitation.org/

doi/pdf/10.1063/1.1694419. URL: https://aip.scitation.org/doi/abs/10.1063/1.1694419.

[78] I. P. Shkarofsky. "VALUES OF THE TRANSPORT COEFFICIENTS IN A PLASMA FOR ANY DEGREE OF IONIZATION BASED ON A MAXWELLIAN DISTRIBUTION". In: *Canadian Journal of Physics* 39.11 (1961), pp. 1619–1703. DOI: 10.1139/p61-192. eprint: https://doi.org/10.1139/p61-192. URL: https://doi.org/10.1139/p61-192.

[79] S Depierreux et al. "Interaction physics for the shock ignition scheme of inertial confinement fusion targets". In: *Plasma Physics and Controlled Fusion* 53.12 (2011), p. 124034. URL: http://stacks.iop.org/0741-3335/53/i=12/a=124034.

[80] J. F. Drake and Y. C. Lee. "Temporally Growing Raman Backscattering Instabilities in an Inhomogeneous Plasma". In: *Phys. Rev. Lett.* 31 (19 Nov. 1973), pp. 1197–1200. DOI: 10.1103/PhysRevLett.31.1197. URL: https://link.aps.org/doi/10.1103/PhysRevLett.31.1197.

[81] Marshall N. Rosenbluth. "Parametric Instabilities in Inhomogeneous Media". In: *Phys. Rev. Lett.* 29 (9 Aug. 1972), pp. 565–567. DOI: 10.1103/PhysRevLett.29.565. URL: https://link.aps.org/doi/10.1103/PhysRevLett.29.565.

[82] A. M. (Aleksandr Markovich) Rubenchik and S. Witkowski. *Physics of laser plasma*. North-Holland, 1991, p. 654. ISBN: 0444874267. URL: https://inis.iaea.org/search/search.aspx?orig%7B%5C_%7Dq=RN:24048688.

[83] Kent Estabrook, W. L. Kruer, and B. F. Lasinski. "Heating by Raman Backscatter and Forward Scatter". In: *Phys. Rev. Lett.* 45 (17 Oct. 1980), pp. 1399–1403. DOI: 10.1103/PhysRevLett.45.1399. URL: https://link.aps.org/doi/10.1103/PhysRevLett.45.1399.

[84] B. Yaakobi et al. "Measurements of the divergence of fast electrons in laser-irradiated spherical targets". In: *Physics of Plasmas* 20.9 (2013), p. 092706. DOI: 10.1063/1.4824008. eprint: https://doi.org/10.1063/1.4824008. URL: https://doi.org/10.1063/1.4824008.

[85] E. A. Williams et al. "The frequency and damping of ion acoustic waves in hydrocarbon (CH) and two-ion-species plasmas". In: *Physics of Plasmas* 2.1 (1995), pp. 129–138. DOI: 10.1063/1.871101. eprint: https://doi.org/10.1063/1.871101. URL: https://doi.org/10.1063/1.871101.

[86] Burton D Fried and Samuel D Conte. *The plasma dispersion function: the Hilbert transform of the Gaussian*. Academic Press, 1961.

[87] Burton D. Fried, Roscoe B. White, and Thomas K. Samec. “Ion Acoustic Waves in a Multi-Ion Plasma”. In: *The Physics of Fluids* 14.11 (1971), pp. 2388–2392. DOI: 10.1063/1.1693346. eprint: https://aip.scitation.org/doi/pdf/10.1063/1.1693346. URL: https://aip.scitation.org/doi/abs/10.1063/1.1693346.

[88] D. W. Phillion, W. L. Kruer, and V. C. Rupert. “Brillouin Scatter in Laser-Produced Plasmas”. In: *Phys. Rev. Lett.* 39 (24 Dec. 1977), pp. 1529–1533. DOI: 10.1103/PhysRevLett.39.1529. URL: https://link.aps.org/doi/10.1103/PhysRevLett.39.1529.

[89] Kazuo Tanaka and Leonard M. Goldman. “Observations of Brillouin Sidescatter in Laser-Produced Plasmas”. In: *Phys. Rev. Lett.* 45 (19 Nov. 1980), pp. 1558–1561. DOI: 10.1103/PhysRevLett.45.1558. URL: https://link.aps.org/doi/10.1103/PhysRevLett.45.1558.

[90] G. Cristoforetti et al. “Time evolution of stimulated Raman scattering and two-plasmon decay at laser intensities relevant for shock ignition in a hot plasma”. In: *High Power Laser Science and Engineering* 7 (2019), e51. DOI: 10.1017/hpl.2019.37.

[91] Uri Samir, K. H. Wright Jr., and N. H. Stone. “The expansion of a plasma into a vacuum: Basic phenomena and processes and applications to space plasma physics”. In: *Reviews of Geophysics* 21.7 (1983), pp. 1631–1646. DOI: 10.1029/RG021i007p01631. eprint: https://agupubs.onlinelibrary.wiley.com/doi/pdf/10.1029/RG021i007p01631. URL: https://agupubs.onlinelibrary.wiley.com/doi/abs/10.1029/RG021i007p01631.

[92] B. H. Ripin et al. “Enhanced Backscatter with a Structured Laser Pulse”. In: *Phys. Rev. Lett.* 39 (10 Sept. 1977), pp. 611–615. DOI: 10.1103/PhysRevLett.39.611. URL: https://link.aps.org/doi/10.1103/PhysRevLett.39.611.

[93] B. H. Ripin and E.A. McLean. “Brillouin backscatter dependence upon pulse amplitudes, timing, target material, and geometry”. In: *Applied Physics Letters* 34.11 (1979), pp. 809–811. DOI: 10.1063/1.90653. eprint: https://doi.org/10.1063/1.90653. URL: https://doi.org/10.1063/1.90653.

[94] D. H. Froula, L. Divol, and S. H. Glenzer. “Measurements of Nonlinear Growth of Ion-Acoustic Waves in Two-Ion-Species Plasmas with Thomson Scattering”. In: *Phys. Rev. Lett.* 88 (10 Feb. 2002), p. 105003. DOI: 10.1103/PhysRevLett.88.105003. URL: https://link.aps.org/doi/10.1103/PhysRevLett.88.105003.

[95] P. Kaw, G. Schmidt, and T. Wilcox. “Filamentation and trapping of electromagnetic radiation in plasmas”. In: *The Physics of Fluids* 16.9 (1973), pp. 1522–1525. DOI: 10.1063/1.1694552. eprint: https://aip.scitation.org/doi/pdf/10.1063/1.1694552. URL: https://aip.scitation.org/doi/abs/10.1063/1.1694552.

[96] F. W. Perkins and E. J. Valeo. "Thermal Self-Focusing of Electromagnetic Waves in Plasmas". In: *Phys. Rev. Lett.* 32 (22 June 1974), pp. 1234–1237. DOI: 10.1103/PhysRevLett.32.1234. URL: https://link.aps.org/doi/10.1103/PhysRevLett.32.1234.

[97] Claire Ellen Max, Jonathan Arons, and A. Bruce Langdon. "Self-Modulation and Self-Focusing of Electromagnetic Waves in Plasmas". In: *Phys. Rev. Lett.* 33 (4 July 1974), pp. 209–212. DOI: 10.1103/PhysRevLett.33.209. URL: https://link.aps.org/doi/10.1103/PhysRevLett.33.209.

[98] Claire E. Max, C. F. McKee, and W. C. Mead. "A model for laser driven ablative implosions". In: *The Physics of Fluids* 23.8 (1980), pp. 1620–1645. DOI: 10.1063/1.863183. eprint: https://aip.scitation.org/doi/pdf/10.1063/1.863183. URL: https://aip.scitation.org/doi/abs/10.1063/1.863183.

[99] Claire Ellen Max, Christopher F. McKee, and W. C. Mead. "Scaling of Ablative Laser-Fusion Implosions". In: *Phys. Rev. Lett.* 45 (1 July 1980), pp. 28–31. DOI: 10.1103/PhysRevLett.45.28. URL: https://link.aps.org/doi/10.1103/PhysRevLett.45.28.

[100] I.N Ross et al. "The prospects for ultrashort pulse duration and ultrahigh intensity using optical parametric chirped pulse amplifiers". In: *Optics Communications* 144.1 (1997), pp. 125–133. ISSN: 0030-4018. DOI: https://doi.org/10.1016/S0030-4018(97)00399-4. URL: http://www.sciencedirect.com/science/article/pii/S0030401897003994.

[101] Donna Strickland and Gerard Mourou. "Compression of amplified chirped optical pulses". In: *Optics Communications* 55.6 (1985), pp. 447–449. ISSN: 0030-4018. DOI: https://doi.org/10.1016/0030-4018(85)90151-8. URL: http://www.sciencedirect.com/science/article/pii/0030401885901518.

[102] M. Hohenberger et al. "Optical smoothing of laser imprinting in planar-target experiments on OMEGA EP using multi-FM 1-D smoothing by spectral dispersion". In: *Physics of Plasmas* 23.9 (2016), p. 092702. DOI: 10.1063/1.4962185. eprint: https://doi.org/10.1063/1.4962185. URL: https://doi.org/10.1063/1.4962185.

[103] Terrance J Kessler et al. "Phase conversion of lasers with low-loss distributed phase plates". In: *Proc. SPIE* 1870 (1993), pp. 95–104. URL: http://proceedings.spiedigitallibrary.org/pdfaccess.ashx?url=/data/conferences/spiep/57034/95_1.pdf.

[104] Cliff D Chen. "Spectrum and conversion efficiency measurements of suprathermal electrons from relativistic laser plasma interactions". PhD thesis. Massachusetts Institute of Technology, 2009. URL: http://hdl.handle.net/1721.1/53213.

[105] B. Hidding et al. "Novel method for characterizing relativistic electron beams in a harsh laser-plasma environment". In: *Review of Scientific Instruments* 78.8 (2007),

p. 083301. DOI: 10.1063/1.2775668. eprint: https://doi.org/10.1063/1.2775668. URL: https://doi.org/10.1063/1.2775668.

[106] B. R. Maddox et al. “High-energy x-ray backlighter spectrum measurements using calibrated image plates”. In: *Review of Scientific Instruments* 82.2 (2011), p. 023111. DOI: 10.1063/1.3531979. eprint: https://doi.org/10.1063/1.3531979. URL: https://doi.org/10.1063/1.3531979.

[107] G. Boutoux et al. “Validation of modelled imaging plates sensitivity to 1-100 keV x-rays and spatial resolution characterisation for diagnostics for the PETawatt Aquitaine Laser”. In: *Review of Scientific Instruments* 87.4 (2016), p. 043108. DOI: 10.1063/1.4944863. eprint: https://doi.org/10.1063/1.4944863. URL: https://doi.org/10.1063/1.4944863.

[108] G. Boutoux et al. “Study of imaging plate detector sensitivity to 5-18 MeV electrons”. In: *Review of Scientific Instruments* 86.11 (2015), p. 113304. DOI: 10.1063/1.4936141. eprint: https://doi.org/10.1063/1.4936141. URL: https://doi.org/10.1063/1.4936141.

[109] C. Stoeckl et al. “A spherical crystal imager for OMEGA EP”. In: *Review of Scientific Instruments* 83.3 (2012), p. 033107. DOI: 10.1063/1.3693348. URL: http://dx.doi.org/10.1063/1.3693348.

[110] L. C. Jarrott et al. “Calibration and characterization of a highly efficient spectrometer in von Hamos geometry for 7-10 keV x-rays”. In: *Review of Scientific Instruments* 88.4 (2017), p. 043110. DOI: 10.1063/1.4981793. URL: http://dx.doi.org/10.1063/1.4981793.

[111] C Hombourger. “An empirical expression for K-shell ionization cross section by electron impact”. In: *Journal of Physics B: Atomic, Molecular and Optical Physics* 31.16 (Aug. 1998), pp. 3693–3702. DOI: 10.1088/0953-4075/31/16/020. URL: https://doi.org/10.1088%5C%2F0953-4075%5C%2F31%5C%2F16%5C%2F020.

[112] M.J. Berger et al. *ESTAR, PSTAR, and ASTAR: Computer Programs for Calculating Stopping-Power and Range Tables for Electrons, Protons, and Helium Ions*. Accessed: 2020-05-20. NIST Physics Laboratory Gaithersburg, MD, 2005. URL: http://physics.nist.gov/Star.

[113] Leonard Charles Jarrott. “Fast electron transport and spatial energy deposition in Cu-doped fast ignition plasmas”. PhD thesis. UC San Diego, 2015.

[114] J. R. Davies, A. R. Bell, and M. Tatarakis. “Magnetic focusing and trapping of high-intensity laser-generated fast electrons at the rear of solid targets”. In: *Phys. Rev. E* 59 (5 May 1999), pp. 6032–6036. DOI: 10.1103/PhysRevE.59.6032. URL: https://link.aps.org/doi/10.1103/PhysRevE.59.6032.

[115] D. H. Froula et al. “Optical diagnostic suite (schlieren, interferometry, and grid image refractometry) on OMEGA EP using a 10-ps, 263-nm probe beam”. In: *Review of Scientific Instruments* 83.10 (2012), 10E523. DOI: 10.1063/1.4733739. URL: http://dx.doi.org/10.1063/1.4733739.

[116] D. Haberberger et al. “Measurements of electron density profiles using an angular filter refractometer”. In: *Physics of Plasmas* 21.5 (2014), p. 056304. DOI: 10.1063/1.4873899. URL: http://dx.doi.org/10.1063/1.4873899.

[117] A. Davies et al. “Polarimetry diagnostic on OMEGA EP using a 10-ps, 263-nm probe beam”. In: *Review of Scientific Instruments* 85.11 (2014), 11E611. DOI: 10.1063/1.4889908. eprint: https://doi.org/10.1063/1.4889908. URL: https://doi.org/10.1063/1.4889908.

[118] Amrutha Gopal, Stefano Minardi, and Michael Tatarakis. “Quantitative two-dimensional shadowgraphic method for high-sensitivity density measurement of under-critical laser plasmas”. In: *Opt. Lett.* 32.10 (May 2007), pp. 1238–1240. DOI: 10.1364/OL.32.001238. URL: http://ol.osa.org/abstract.cfm?URI=ol-32-10-1238.

[119] Wolfgang Merzkirch. *Flow Visualization*. 2nd ed. 1987, p. 128.

[120] Muhammad Firmansyah Kasim et al. “Quantitative shadowgraphy and proton radiography for large intensity modulations”. In: *Phys. Rev. E* 95 (2 Feb. 2017), p. 023306. DOI: 10.1103/PhysRevE.95.023306. URL: https://link.aps.org/doi/10.1103/PhysRevE.95.023306.

[121] Muhammad Firmansyah Kasim. *Invert shadowgraphy and proton radiography*. https://github.com/mfkasim91/invert-shadowgraphy. 2018.

[122] Mohamed M. Sulman, J.F. Williams, and Robert D. Russell. “An efficient approach for the numerical solution of the Monge–Ampere equation”. In: *Applied Numerical Mathematics* 61.3 (2011), pp. 298–307. ISSN: 0168-9274. DOI: https://doi.org/10.1016/j.apnum.2010.10.006. URL: http://www.sciencedirect.com/science/article/pii/S0168927410001819.

[123] B. Fryxell et al. “FLASH: An Adaptive Mesh Hydrodynamics Code for Modeling Astrophysical Thermonuclear Flashes”. In: *The Astrophysical Journal Supplement Series* 131.1 (2000), p. 273. URL: http://stacks.iop.org/0067-0049/131/i=1/a=273.

[124] *PrOpacEOS Overview*. http://www.prism-cs.com/Software/Propaceos/overview.html. Accessed: 2020-05-29.

[125] D. S. Montgomery et al. “Measurements of Radial Heat Wave Propagation in Laser-Produced Exploding-Foil Plasmas”. In: *Phys. Rev. Lett.* 73 (15 Oct. 1994), pp. 2055–

2058. DOI: 10.1103/PhysRevLett.73.2055. URL: https://link.aps.org/doi/10.1103/PhysRevLett.73.2055.

[126] S. Zhang et al. "Experimental study of hot electron generation in shock ignition relevant high-intensity regime with large scale hot plasmas". In: *Physics of Plasmas* 27.2 (2020), p. 023111. DOI: 10.1063/1.5119250. eprint: https://doi.org/10.1063/1.5119250. URL: https://doi.org/10.1063/1.5119250.

[127] S. Zhang et al. "Generation of Collimated Moderate Temperature Electron Beam and Laser Plasma Interaction for Megajoule Shock Ignition". to be submitted.

[128] Anshu Dubey et al. "Extensible component-based architecture for FLASH, a massively parallel, multiphysics simulation code". In: *Parallel Computing* 35.1011 (2009), pp. 512–522. ISSN: 0167-8191. DOI: http://dx.doi.org/10.1016/j.parco.2009.08.001. URL: http://www.sciencedirect.com/science/article/pii/S0167819109000945.

[129] L. Ceurvorst et al. "Channel optimization of high-intensity laser beams in millimeter-scale plasmas". In: *Phys. Rev. E* 97 (4 Apr. 2018), p. 043208. DOI: 10.1103/PhysRevE.97.043208. URL: https://link.aps.org/doi/10.1103/PhysRevE.97.043208.

[130] L. I. Sedov. *Similarity and Dimensional Methods in Mechanics*. 10th. Boca Raton: CRC Press, May 1993. ISBN: 9780203739730. DOI: 10.1201/9780203739730. URL: https://doi.org/10.1201/9780203739730%20https://www.taylorfrancis.com/books/9781351416573.

[131] J. Li et al. "Pump depletion and hot-electron generation in long-density-scale-length plasma with shock-ignition high-intensity laser". In: *Phys. Rev. E* 101 (3 Mar. 2020), p. 033206. DOI: 10.1103/PhysRevE.101.033206. URL: https://link.aps.org/doi/10.1103/PhysRevE.101.033206.

[132] C. N. Judice, J. F. Decker, and R. A. Stern. "Breaking and Turbulent Transition in Ion Acoustic Waves". In: *Phys. Rev. Lett.* 30 (7 Feb. 1973), pp. 267–270. DOI: 10.1103/PhysRevLett.30.267. URL: https://link.aps.org/doi/10.1103/PhysRevLett.30.267.

[133] Bruce I. Cohen et al. "Resonantly excited nonlinear ion waves". In: *Physics of Plasmas* 4.4 (1997), pp. 956–977. DOI: 10.1063/1.872187. eprint: https://doi.org/10.1063/1.872187. URL: https://doi.org/10.1063/1.872187.

[134] S. Weber, C. Riconda, and V. T. Tikhonchuk. "Low-Level Saturation of Brillouin Backscattering due to Cavity Formation in High-Intensity Laser-Plasma Interaction". In: *Phys. Rev. Lett.* 94 (5 Feb. 2005), p. 055005. DOI: 10.1103/PhysRevLett.94.055005. URL: https://link.aps.org/doi/10.1103/PhysRevLett.94.055005.

[135] S. Weber, C. Riconda, and V. T. Tikhonchuk. “Strong kinetic effects in cavity-induced low-level saturation of stimulated Brillouin backscattering for high-intensity laser-plasma interaction”. In: *Physics of Plasmas* 12.4 (2005), p. 043101. DOI: 10.1063/1.1862246. eprint: https://doi.org/10.1063/1.1862246. URL: https://doi.org/10.1063/1.1862246.

[136] L. Divol et al. “Nonlinear saturation of stimulated Brillouin scattering for long time scales”. In: *Physics of Plasmas* 10.9 (2003), pp. 3728–3732. DOI: 10.1063/1.1601223. eprint: https://doi.org/10.1063/1.1601223. URL: https://doi.org/10.1063/1.1601223.

[137] W. L. Kruer, E. J. Valeo, and K. G. Estabrook. “Limitation of Brillouin Scattering in Plasmas”. In: *Phys. Rev. Lett.* 35 (16 Oct. 1975), pp. 1076–1079. DOI: 10.1103/PhysRevLett.35.1076. URL: https://link.aps.org/doi/10.1103/PhysRevLett.35.1076.

[138] J. Li, R. Yan, and C. Ren. “Density modulation-induced absolute laser-plasma-instabilities: Simulations and theory”. In: *Physics of Plasmas* 24.5 (2017), p. 052705. DOI: 10.1063/1.4983143. eprint: https://doi.org/10.1063/1.4983143. URL: https://doi.org/10.1063/1.4983143.

[139] B. E. Kruschwitz et al. “Accurate target-plane focal-spot characterization in high-energy laser systems using phase retrieval”. In: *Opt. Express* 20.19 (Sept. 2012), pp. 20874–20883. DOI: 10.1364/OE.20.020874. URL: http://www.opticsexpress.org/abstract.cfm?URI=oe-20-19-20874.

[140] L von Hamos. “Roetgen Spectra Image by Means of the Crystal Effect”. In: *Ann. Phys* 17.6 (1933), pp. 716–724.

[141] F. J. Marshall et al. “Imaging of laser-plasma x-ray emission with charge-injection devices”. In: *Review of Scientific Instruments* 72.1 (2001), pp. 713–716. DOI: 10.1063/1.1318257. eprint: https://doi.org/10.1063/1.1318257. URL: https://doi.org/10.1063/1.1318257.

[142] J.J. Macfarlane. “{IONMIX} - a code for computing the equation of state and radiative properties of {LTE} and non-LTE plasmas”. In: *Computer Physics Communications* 56.2 (1989), pp. 259–278. ISSN: 0010-4655. DOI: http://dx.doi.org/10.1016/0010-4655(89)90023-4. URL: http://www.sciencedirect.com/science/article/pii/0010465589900234.

[143] D. E. Hinkel, E. A. Williams, and C. H. Still. “Laser Beam Deflection Induced by Transverse Plasma Flow”. In: *Phys. Rev. Lett.* 77 (7 Aug. 1996), pp. 1298–1301. DOI: 10.1103/PhysRevLett.77.1298. URL: https://link.aps.org/doi/10.1103/PhysRevLett.77.1298.

[144] J. D. Moody et al. “First Optical Observation of Intensity Dependent Laser Beam Deflection in a Flowing Plasma”. In: *Phys. Rev. Lett.* 77 (7 Aug. 1996), pp. 1294–1297. DOI: 10.1103/PhysRevLett.77.1294. URL: https://link.aps.org/doi/10.1103/PhysRevLett.77.1294.

[145] P. E. Young et al. “Observations of Laser-Beam Bending due to Transverse Plasma Flow”. In: *Phys. Rev. Lett.* 81 (7 Aug. 1998), pp. 1425–1428. DOI: 10.1103/PhysRevLett.81.1425. URL: https://link.aps.org/doi/10.1103/PhysRevLett.81.1425.

[146] J. Trela et al. “The control of hot-electron preheat in shock-ignition implosions”. In: *Physics of Plasmas* 25.5 (2018), p. 052707. DOI: 10.1063/1.5020981. eprint: https://doi.org/10.1063/1.5020981. URL: https://doi.org/10.1063/1.5020981.

[147] L. Antonelli et al. “Laser-driven strong shocks with infrared lasers at intensity of 1016 W/cm2”. In: *Physics of Plasmas* 26.11 (2019), p. 112708. DOI: 10.1063/1.5119697. eprint: https://doi.org/10.1063/1.5119697. URL: https://doi.org/10.1063/1.5119697.

[148] S. D. Baton et al. “Experiment in Planar Geometry for Shock Ignition Studies”. In: *Phys. Rev. Lett.* 108 (19 May 2012), p. 195002. DOI: 10.1103/PhysRevLett.108.195002. URL: https://link.aps.org/doi/10.1103/PhysRevLett.108.195002.

[149] Juan Francisco Lam, Bernard Lippmann, and Frederick Tappert. “Selftrapped laser beams in plasma”. In: *The Physics of Fluids* 20.7 (1977), pp. 1176–1179. DOI: 10.1063/1.861679. eprint: https://aip.scitation.org/doi/pdf/10.1063/1.861679. URL: https://aip.scitation.org/doi/abs/10.1063/1.861679.

[150] R. A. Fonseca et al. “Computational Science — ICCS 2002: International Conference Amsterdam, The Netherlands, April 21–24, 2002 Proceedings, Part III”. In: ed. by Peter M. A. Sloot et al. Berlin, Heidelberg: Springer Berlin Heidelberg, 2002. Chap. OSIRIS: A Three-Dimensional, Fully Relativistic Particle in Cell Code for Modeling Plasma Based Accelerators, pp. 342–351. ISBN: 978-3-540-47789-1. DOI: 10.1007/3-540-47789-6_36. URL: http://dx.doi.org/10.1007/3-540-47789-6_36.

[151] S. Weber et al. “Fast saturation of the two-plasmon-decay instability for shock-ignition conditions”. In: *Phys. Rev. E* 85 (1 Jan. 2012), p. 016403. DOI: 10.1103/PhysRevE.85.016403. URL: https://link.aps.org/doi/10.1103/PhysRevE.85.016403.